DOTTORATO DI RICERCA IN
FISICA

XXIII CICLO

Sede Amministrativa
Università degli Studi di MODENA e REGGIO EMILIA

TESI PER IL CONSEGUIMENTO DEL TITOLO DI
DOTTORE DI RICERCA

Quantum effects in molecular spin clusters

Candidata: Giulia Lorusso

Relatore: Prof. Marco Affronte

Contents

I Introduction **1**

1 Introduction **3**

1.1 Molecular spin clusters 3

1.1.1 Triangular spin clusters 4

1.1.2 Heterometallic AF spin rings 5

1.1.3 Spin Hamiltonian description 8

1.1.4 Linking the rings 10

1.2 Entanglement between molecular spins 12

1.3 Quantum communication through molecular AF spin ring 15

1.4 Theoretical Background on solid state physical properties 17

1.4.1 Specific heat 17

1.4.2 AC-DC Magnetometry 21

2 Experimental methods and theory of measurements **25**

2.1 Low temperature set-up 25

2.2 Specific heat and calorimetry 27

2.2.1 Theory of Measurement 27

2.2.2 Experimental setup 29

2.3 QD AC-DC Magnetometer 31

2.4 Hall micro-probe magnetometry 33

2.4.1 Working principle: the Hall effect 33

2.4.2 Hall devices 34

2.5 Development of the new setup 45

II Results **55**

3 Closed spin rings: Cr_xCu_2 family. **57**
3.1 Structures and synthesis details 59
3.2 Magnetic characterization 60
3.2.1 Theoretical Models 64
Discussion 70

4 Open spin rings: Cr_6InNi and Cr_7InNi **73**
4.1 Synthesis and structural characterization 74
4.2 Thermodynamic properties 75
Conclusions 82

5 Chromium-based triangles **83**
5.1 Cr_3 83
5.1.1 Magnetic characterization 84
5.2 Cr_2Cu 88
5.2.1 Structure 89
5.2.2 Thermodynamic characterization 89
Conclusions 94

6 Magnetic coupling in supramolecular Cr_7Ni spin systems **95**
6.1 *Purple*-Cr_7Ni ring 96
6.2 Supramolecular systems $(Cr_7Ni)_n$ with $n > 2$ 100
6.3 *Purple*-(Cr_7M)/*Green*-(Cr_7M') dimers 106
6.4 Changing the linker in *purple*-$(Cr_7Ni)_2$ dimers 111
6.4.1 Experimental characterization 112
Conclusions 116

7 Spin entanglement between two Cr_7Ni molecular clusters **119**
7.1 Magnetic characterization 120
7.2 Measurement of the entanglement 127
Conclusions 131

III General Conclusions **133**

8 Conclusions **135**

Appendixes **137**

A Probing edge magnetization: X-ray Magnetic Circular Dichroism **139**

A.1 Cr_6InNi and Cr_7InNi 139

A.2 Cr_2Cu 143

B Propagation of spin information: Density Functional Theory calculations **147**

C Entanglement quantification: Concurrence calculation **151**

Bibliography **152**

Curriculum vitae **169**

Part I

Introduction

Chapter 1

Introduction

1.1 Molecular spin clusters

Molecular spin clusters are ideal test bed for the study of nanoscale magnetic phenomena. These systems are molecules of few nanometers, constituted by a magnetic nucleus surrounded by organic chemical groups. The magnetic core is typically constituted by transition metals, rare-earth ions or even organic radicals, while the organic bridges comprise light elements like carbon, oxygen, hydrogen and nitrogen. The deep level of control achieved by chemical synthesis allows to produce collections of identical molecules embedded in crystalline structures and aligned along specific crystallographic directions. Although the final product of synthesis appears as macroscopic samples, i.e. bulk crystals or powders, generally, the inter-molecular magnetic interactions are negligible with respect to those within the molecule and we can assume these materials as statistical ensembles of quantum systems. Therefore, solid state experimental techniques, like the measurements of thermodynamic properties, reflect mainly ensemble properties of the single molecule. The experimental conditions needed to reveal the quantum behavior are easily achievable in laboratory: molecular spectra are well resolved at liquid helium temperatures, while level crossings can be observed at few teslas fields. All these reasons contributed to the success of molecular magnets in the last 20 years.

Structural and physical features of molecular magnets can be tailored at synthetic level and a huge variety of molecules can be produced. A first differentia-

tion that can be done among these systems is the dimensionality of the structure: zero dimensional (0D), for isolated structure; one-dimensional (1D), for chains or segments of spin; two-dimensional (2D), in case of matrix systems; and finally three-dimensional (3D) structures. The molecules can be distinguished also for the type of material: there are inorganic magnetic molecules, like polyoxometalates (POM) [1–3]; metal-organic molecules; and finally only organic systems in which the magnetic moment is carried by radicals [4, 5]. Finally and most important the classification of molecular spin clusters can be based on their different magnetic properties: single-molecule magnets (SMM), photomagnetic and spin-cross-over derivatives, ferromagnetic or antiferromagnetic chains and antiferromagnetic rings.

SMM is a wide class of molecules with high spin. Among them, Mn_{12}-acetate has $S = 10$ and high anisotropy barrier [6–8], it is one of the first ones that has been extensively studied and probably also the most popular. Together with Fe_8, for Mn_{12}-ac key experimental results were obtained like: tunneling of magnetization [9–13], the observation of quantum phase interference (Berry phase) [14] and coherent quantum oscillations of spin between two energy minima [15].

In this thesis the attention is focused on another interesting subclass of magnetic molecules, that of antiferromagnetic (AF) spin rings. These, differently to the SMM, are low spin systems and with lower dipolar interaction, that are advantages, as discussed later, for applications in quantum information processing. The first AF rings synthesized were homometallic and based on trivalent metals. As examples, there are rings based on Fe^{+3} ($s = 5/2$), like Fe_6 [16,17], F_{10} [17,18], Fe_{12} [19] and Fe_{18} [20]; those on Cr^{+3} ($s = 3/2$), like Cr_8 [21–23] and Cr_{10} [24]; and finally based on V^{+3}, like V_8 and V_{10} [25].

1.1.1 Triangular spin clusters

Triangular spin molecular systems (trimers) with dominant AF coupling are particularly appealing since they show a rich Physics in spite of their simplicity. For instance, they represent the simplest models to study spin frustration [26–36]. Indeed, for a triangle with three equal spins S, the dominant AF coupling gives rise to doubly degenerate doublets whose degeneracy can be split by differences in intra-molecular exchange coupling constants J [37–42]. More generally, the

theoretical problem of three interacting spins S_i can be solved in different ways, allowing the direct comparison of exact theoretical predictions with the experimental results. Thus, it is not surprising that in the last twenty years or so, a plethora of molecular spin trimers have been synthesized and their chemical, structural and magnetic properties have been widely investigated [43].

Recently AF spin triangles have attracted a renewed interest of physicists as model systems in the context of Quantum Information Processing (QIP). AF spin triangles have been indeed proposed as effective two-level systems for implementation of quantum gates [44]. The main advantage of spin triangles resides in their low energy spectrum that allows a tunable effective inter-qubit coupling even in presence of permanent microscopic interactions [45]. Another interesting issue is the manipulation of spin states by electric fields. In this respect spin triangles have shown special interplay between spin exchange, spin-orbit interaction, and the chirality that make them particularly suitable for coupling with electric field [46]. Synthesis and characterization of new molecular trimers thus provides real cases to be discussed and eventually exploited in these new contexts.

1.1.2 Heterometallic AF spin rings

Even-membered AF rings have a fully compensated total spin. A recent approach is the introduction of an extra spin, in order to break the compensation and control the total spin of the AF wheels. This strategy was used for the Cr-based cyclic systems to synthesize heterometallic molecular wheels in which one Cr ion is substituted with a divalent transition metal M [47]. [1] If M =Ni^{+2} with $s = 1$ the spin balance gives an effective total $S = 1/2$ to the molecule; two examples are Cr_9Ni [48], obtained from Cr_{10}, and Cr_7Ni, obtained from Cr_8.

Cr_7Ni as qubit

The structure of Cr_7Ni is depicted in Fig. 1.1; the 7 Cr^{+3} ($s = 3/2$) ions and the extra Ni^{+2} ($s = 1$) are arranged in a symmetric octagonal planar structure, and with the spins antiferromagnetically coupled. This molecule, synthesized in 2003

[1] Note here that the simple case of adding an equal spin to the wheel, obtaining thus an odd number of equal spins, leads to frustration with a degenerate ground state.

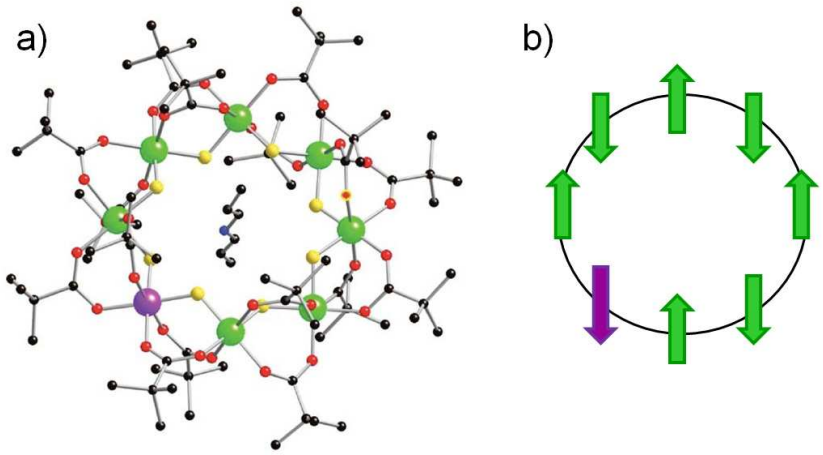

Figure 1.1: a) Crystallographic structure of Cr_7Ni obtained from X-ray diffraction; b) sketch of the spin arrangement in the molecule.

by Dr. G. Timco and the group of Prof. R. E. P. Winpenny at Department of Chemistry, University of Manchester [47], has been deeply investigated by specific heat and torque [49] (reported in Fig. 1.2), nuclear magnetic resonance [21], neutron scattering [50] and micro-SQUID magnetization at very low temperature [51]. The experimental results were fitted by using a spin-Hamiltonian model [52] and $S = 1/2$ ground state well separated from the first excited state ($S = 3/2$) was found (see Fig. 1.3). Afterwards, Cr_7Ni has been proposed as a molecular qubit, suitable candidate for QIP [49, 53]. This proposal has been corroborated by the very promising theoretical [54] and experimental [55] studies of coherence. The time of coherence measured for the molecule is indeed about 3 μs at 2 K, several order of magnitude longer than the time needed for spin manipulation. Finally, successful grafting of isolated molecules on surfaces was recently achieved, with only minor changes in the magnetic features of the bulk-material [56–59]. The next step, in order to exploit Cr_7Ni as qubit for QIP, is to acquire the capability to establish and control magnetic interaction between two or more Cr_7Ni rings (qubits) without altering the properties of the single cluster.

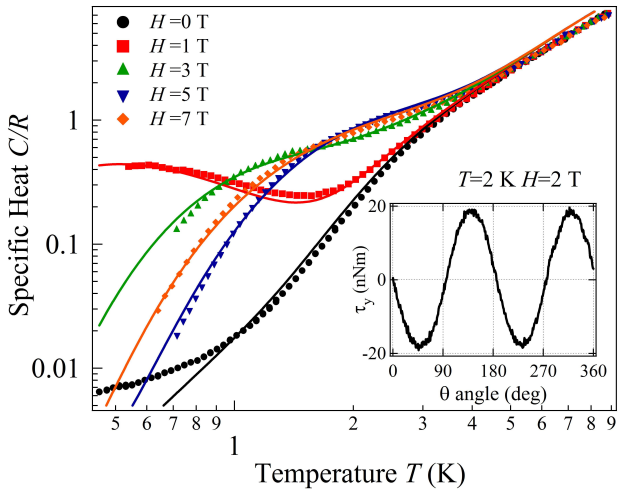

Figure 1.2: Specific heat of Cr_7Ni. (Inset) Torque magnetometry. Figure taken from Ref. [49].

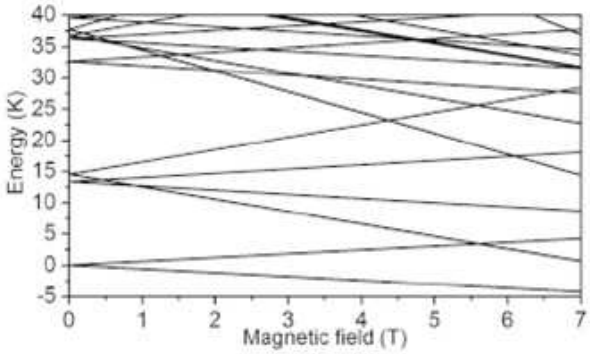

Figure 1.3: Low-lying energy level pattern of Cr_7Ni. Figure taken from Ref. [49].

1.1.3 Spin Hamiltonian description

Despite the complexity of the structure constituted by hundreds of atoms, in molecular spin clusters the magnetic features depend only from the small number of magnetic ions and they can be described by a microscopic spin Hamiltonian model. In these systems the predominant interaction is the exchange coupling, arising from electrostatic interaction between nearest neighbor metal centers. This is described by the isotropic Heisenberg exchange Hamiltonian [60]:

$$\mathcal{H}_{ex} = \sum_{i}^{n-1} J_i \mathbf{s}_i \cdot \mathbf{s}_{i+1}, \tag{1.1}$$

where $J_i > 0$ is the AF exchange constant. The diagonalization of the Heisenberg Hamiltonian [61–63] shows that the energy multiplets are typically structured in three bands: the lowest one, named $L-$band, is a rotational band that follows the Landè rule:

$$E(S) = \frac{2J}{n} S(S+1). \tag{1.2}$$

These excited states are characterized by the rotation of the oppositely oriented total spins of each sublattice. The second group, named $E-$band, is generated by higher energy excitations, which appear with one sublattice spin decreased by one in analogy with spin waves. The third and last band is a quasi-continuum of states [23, 61, 62].

In crystals of AF spin rings, the long-range interactions are negligible for the most cases, because no super-exchange paths between the molecules are available, and because inter-rings dipolar interactions are minimized by the small total spin S. Magnetic anisotropy arises from crystal field and dipolar interactions; this is smaller than isotropic interaction of Eq. 1.1, but finite. The Hamiltonian corresponding to the crystal field is:

$$\mathcal{H}_{cf} = \sum_{i}^{n} \mathbf{s}_i \cdot \mathbf{D}_i \cdot \mathbf{s}_i = \sum_{i=1}^{n} d_i \left[s_{z,i}^2 - s_i(s_i+1)/3 \right] + \sum_{i}^{n} e_i \left[s_{x,i}^2 - s_{y,i}^2 \right], \tag{1.3}$$

where $\mathbf{D}_i$ is the crystal field anisotropy that can be expressed as the sum of the *axial* and *rhombic* contributions (terms on the right side of the equation) and $\mathbf{z}$ is the axis orthogonal to the ring plane. Due to the cyclic symmetry of spin rings, the axial anisotropy constant (d_i) is always greater than the rhombic one

(e_i), and these systems can be considered in good approximation uniaxial [23]. The Hamiltonian corresponding to dipolar interaction reads:

$$\mathcal{H}_{dip} = \sum_{i>j=1}^{n} \mathbf{s}_i \cdot \mathbf{D}_{i,j} \cdot \mathbf{s}_i = \sum_{i>j=1}^{n} \frac{\mu_0 \mu_B^2}{4\pi \mathbf{r}_{i,j}^3} \left(3(g_i \mathbf{s}_i \cdot \mathbf{r}_{i,j})(g_j \mathbf{s}_j \cdot \mathbf{r}_{i,j}) - (g_i \mathbf{s}_i \cdot g_j \mathbf{s}_j)\right), \tag{1.4}$$

where $\mathbf{r}_{i,j}$ is the distance between the spins, g_i is the gyromagnetic factor and μ_B the Bohr magneton. If an external magnetic field $\mathbf{H}$ is present, also the *Zeeman* interaction should be taken into account:

$$\mathcal{H}_{Zeeman} = \mu_B \sum_{i=1}^{n} g_i \mathbf{H} \cdot \mathbf{s}_i. \tag{1.5}$$

The general full Hamiltonian for AF molecular spin clusters therefore is the sum of all the above contribution:

$$\mathcal{H} = \mathcal{H}_{ex} + \mathcal{H}_{cf} + \mathcal{H}_{dip} + \mathcal{H}_{Zeeman} \tag{1.6}$$

The anisotropic part of $\mathcal{H}$ does not commute with the squared total spin operator $\mathbf{S}^2$ thus it mixes subspaces corresponding to different values of the total spin ($S-mixing$). However, the energy spectrum at $H = 0$ is well approximated by a $S-$defined multiplets because the entity of the anisotropic interactions is small.

The pattern of energy levels can be calculated by the diagonalization of the Hamiltonian Eq. 1.6. This is a demanding computational task, since the dimension of the matrix to diagonalize increases hugely with the spin number of magnetic nuclei in the molecule, explicitly: $(2s+1)^n$ for n nuclei with spin s. An efficient solution scheme based on the irreducible tensor operator formalism was developed in Ref. [64], its peculiarity is to maintain the simple total-spin description even in presence of mixing between different multiplets.

Another important aspect is that as soon as the magnetic molecule increases in nuclearity, many independent parameters of the spin-Hamiltonian need to be determined and the possibility of gaining additional information from different techniques became crucial. The use of a variable magnetic field, especially if large field and low temperature are available, often provides the lacking information. This is the case when the paramagnetic centers of the molecule are antiferromagnetically coupled. The state with the largest spin is not necessarily the ground

one, but its energy decreases most rapidly by the *Zeeman* interaction with the field. A crossing of energy levels can be induced by the field and reveals itself as a sudden increase in the magnetization.

1.1.4 Linking the rings

A further challenge is to magnetically couple two (or few) complex molecular units without perturbing the properties of the single ones. Supramolecular dimers of SMMs were already reported by the Christou group in the early 1990s [65], the magnetic coupling of the linked Mn_4 cages through C–H$\cdots$Cl hydrogen bonds were found much later in 2002 [66]. Although magnetic interaction is achieved, change of the linker was not straightforward. Dimers of Mn_4^{III} can be obtained by using diketonates, as shown by Aromì and coworkers [67] but in this case the features of the single units were perturbed. The controlled integration of aromatic linkers with molecular magnetic building blocks would allow to realize supramolecular systems with tailored (and tunable) intermolecular interactions. One critical point in their use at synthetic level, is the risk of obtaining polymeric networks with long-range magnetic order, as demonstrated in the work from Yamashita and co-workers [68], where Mn_4 single molecule magnets are linked through dicyanamide $N(CN)_2$ into a 3-dimensional polymer. Thank to the small dipolar interaction, the Cr_7Ni ring family offers an unique opportunity in this respect.

The first attempt to link together Cr_7Ni rings was realized in 2005 [69]; the link was organo-metallic and it was attached to the Cr_7Ni wheels via hydrogen-bonds between F-bridges within the cage and terminal H–N groups within the link (see Fig. 1.4(a)). Unfortunately, this type of connection between the rings is not efficient for the inter-ring magnetic coupling [48], indeed it was shown that no significant exchange of spin can be achieved through this link. Progresses were achieved linking the rings via the external carboxylates at the Ni edge, where appreciable spin density is found. The dimers represented in Figs. 1.4(b) and (c) are examples of such structures where the magnetic coupling between the rings is permanently established, respectively, by one or two copper ions in the link, as reported in Ref. [70].

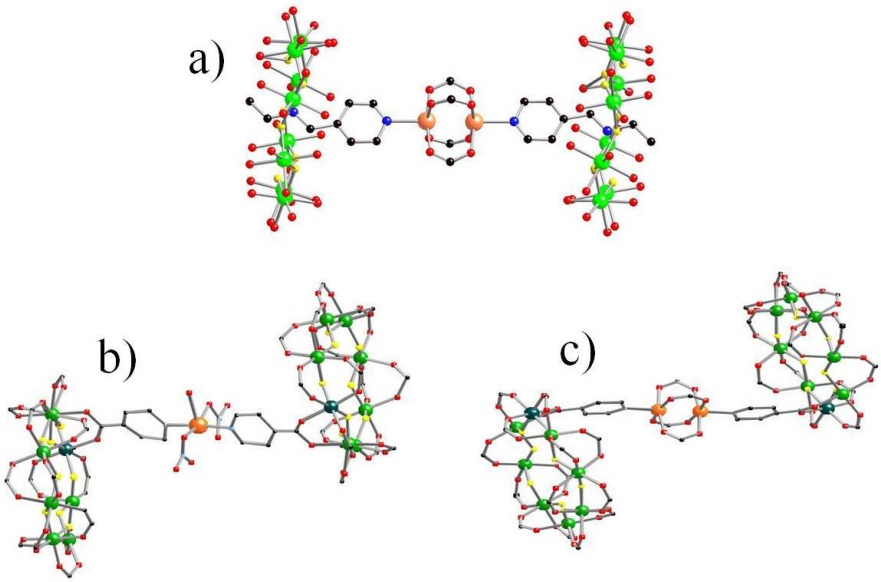

Figure 1.4: Crystallographic structures of the first Cr_7Ni dimers synthesized. In a) the organo-metallic link is connected to the centers of the wheels via hydrogen-bonds (taken from [69]); in b) and c) the link is still organo-metallic but connected via the carboxylate bridge to the Ni edge (taken from [70]). Moreover, in b) and c) the magnetic coupling can be permanently switched on and off via a single Cu ion ($s = 1/2$) and a dimer of Cu ions ($S = 0$), respectively.

1.2 Entanglement between molecular spins

Entanglement is one of the most peculiar property of quantum mechanics. Given a composite system, entanglement is established when the states of the parts are so highly correlated each other that it is impossible to describe one quantum component without the knowledge of the rest of the system[2]. Consequently, as sketched in Fig. 1.5, having two entangled qubits, if we carry out an experiment and we measure one of them, we have information about the state of the other qubit. This property is a great resource for fields like quantum cryptography, teleportation, information and computation [73].

The renewed interest for the exploitation of entanglement in quantum information science has stimulated intensive research activity. Besides, the controlled generation of entanglement among nanoscaled objects allows us to explore the boundary between quantum and classical behavior. For photons [74] or cold atoms, as well as for a few solid state systems [75], entanglement is largely investigated, both theoretically and experimentally trying to unveil both its qualitative and quantitative aspects [71, 72].

For what concerns the entanglement in magnetic systems there is a large theoretical literature [76–83] but still very few experiments [84,85] and the latter are referred to collections of spin systems. So the problem of measuring entanglement in finite spin systems is still very open. Molecular spin clusters represent a very interesting testing ground in this context. In fact, they represent complex but finite systems whose structural and physical features can be tailored at the synthetic level and whose properties can be predicted by microscopic, albeit demanding, models. Recent achievements in supramolecular chemistry, experiments and modeling appear extremely encouraging in this field [70, 86, 87].

The route to measure entanglement between spins in supramolecular structures, such as dimers or oligomers, needs at least two prerequisites: (1) the recognition of molecular building blocks with well-defined features and (2) the establishment of initial intermolecular magnetic coupling without perturbing the single units. Two observations are important. The first is that different kinds of magnetic coupling between the units are compatible with the controlled generation of

[2]The entanglement is exhaustively reviewed in the two recent noteworthy works by Horodecki et al. [71] and Amico et al. [72], see there for further details.

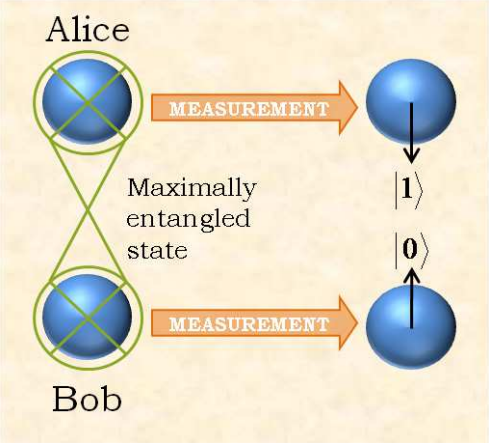

Figure 1.5: Sketch of entanglement in the bipartite system constituted by the two maximally entangled qubits 'Alice' and 'Bob'. A measurement of the second qubit always gives results depending on the state of the first.

entangled states. Dipolar interaction is long range and might be desirable if one searches entanglement of a large collection of objects [84], but it is detrimental to control entanglement between a few molecular units, since it tends to couple molecules belonging to different oligomers. Therefore, local types of magnetic interaction, such as exchange, that is predominant in the case of Cr_7Ni dimers, are preferable. Then, we have to notice that the existence of a magnetic coupling between molecular spin clusters does not guarantee per se that these are in an entangled state, but its form plays a crucial role in the controlled generation of entanglement. Therefore, the high degree of flexibility with which such coupling can be engineered through supramolecular chemistry represents a fundamental resource.

Experimental detection and quantification of entanglement is a demanding task [88]. Formally a state is entangled if its wavefunction cannot be factorized. This definition is not helpful, because, in general, tell whether a state of n parties is separable or not is an open problem. In theory, to reconstruct experimentally the overall density matrix it is necessary to measure the correlations between the observables of all the parties. This approach can be used if a small number of particles are involved, as in the case of photons [74]. Conversely, for magnetic bulk systems, i.e. ensemble of order of Avogadro's number of spins, one may not

refer to individual properties of every constituent of a solid sample or correlation between them. Fortunately, an alternative and much simpler experimental approach exists to certify if a certain state is entangled directly. This tools are the so-called *entanglement witnesses*. An entanglement witness W is a Hermitian operator which is able to detect entanglement in a state. The basic idea is that the expectation value of the witness W for the state ρ under consideration exceeds certain bounds only when ρ is entangled [71, 72]. Recently, the magnetic susceptibility was proposed as entanglement witness by Wiesniak et al. [89]. Microscopically, magnetic susceptibility is, in fact, a sum over all microscopic spin correlation functions $< s_z^i \cdot s_z^j >$ for the sites i and j [89]:

$$\begin{aligned} \chi_z &= \frac{1}{k_B T}\Delta^2(M_z) = \frac{1}{k_B T}(< M_z^2 > - < M_z >^2) \\ &= \frac{1}{k_B T}\left(\sum_{i,j=1}^{N} < s_z^i s_z^j > - < \sum_{i=1}^{N} s_z^i >\right). \end{aligned} \tag{1.7}$$

The above expression is valid in the condition $[\mathcal{H}, \mathcal{H}_1] = 0$, where $\mathcal{H}$ is the Hamiltonian of the system, and $\mathcal{H}_1$ the part of the Hamiltonian that describes the interaction with magnetic field. Thus Eq. 1.7 is always valid for isotropic systems, but we can anticipate that also in case of systems with small anisotropy it is demonstrated to be valid (see Chap. 7). Starting from Eq. 1.7, it can then be demonstrated (for further details see Ref. [89]) that the system is entangled if:

$$\bar{\chi} \equiv \frac{1}{3}\left(\frac{\chi_x}{g_x^2} + \frac{\chi_y}{g_y^2} + \frac{\chi_z}{g_z^2}\right) \lesssim \frac{N_A \mu_B^2 S}{k_B T} \tag{1.8}$$

where χ_x, χ_y and χ_z are the susceptibilities measured along three orthogonal directions, g_x, g_y and g_z are the corresponding gyromagnetic factors, N_A is Avogadro's number, k_B the Boltzmann constant, μ_B the Bohr magneton and finally S is the spin of the systems taken into account. As visible from Eq. 1.8, the entanglement witness depends on the temperature T, meaning that the same system can be entangled for certain temperature ranges and not entangled in others. This is a direct consequence that the entanglement is a property of the state of the system. Moreover, this enlightens the distinction between entanglement and simple interaction that, being related to the Hamiltonian of the system, is instead independent from the temperature.

The limits of entanglement witness approach are essentially two: it gives only a sufficient condition for entanglement and it is poor in quantitative information. For the cases in which it is possible to know the eigenvalues of the Hamiltonian a quantification of the entanglement can be done theoretically by the calculation of the concurrence ($\mathcal{C}$) [71, 72, 88]. By definition [72] that concurrence is a monotonous function of the entanglement of formation and it can assume values comprised between zero and one, which represent the extreme situations of a not entangled or maximally entangled state, respectively. A generalized analytic expression for the concurrence is hard to give, it should be calculated case by case (see Chap. 7 for the case of two $S = 1/2$ spins).

1.3 Quantum communication through molecular AF spin ring

Quantum communication through a spin chain has recently received theoretical interest: in an ideal quantum computer based on spin qubits, spin chains have been proposed as channels for short distance transmission of (quantum state) information [90,91]. In particular, Bose et al. [92] propose Heisenberg ferromagnetic rings with twisted boundary conditions as busses for connecting a large number of parties (spin 1/2) and address the fidelity of the quantum communication between any pairs of such parties. From the experimental side, several works show the possibility to fabricate spin chains with tailored magnetic interactions. One of the first attempts to create artificial spin segments by aligning atoms on a surface was reported by Gambardella et al. [93, 94]. Good examples of atomic structures were recently engineered by the IBM group [95]: few magnetic Mn atoms were aligned on a CuN surface, thus forming antiferromagnetic spin segments. Molecular chemistry has proven to be a powerful approach synthesizing a wide range of structures that can be produced in scalable units [96]. The finite size of a spin chain leads to a discrete spectrum of excitations. Recently, spin waves has been studied in detail in the case of molecular spin clusters [23, 61–63] considering also the effect of cyclic symmetry breakings [96] in the spectrum of the principal three bands described in section 1.1.3. Thus, AF molecular spin rings can represent examples of real systems where quantum communication can be applied.

The implementation of quantum state transfer with magnetic molecular clusters requires the actuation of a specific protocol, that can essentially be schematized in four steps [97]:

1. initialization of the system in a well defined quantum state;

2. at time $t = 0$ the first spin of the chain, s_1, is switched by a rotation in the Bloch sphere to the state $|\Psi(0) >_1$;

3. the spin chain is left to evolve freely for a given time T

4. at time $t = T$, s_n is found in the final state $|\Psi(T) >_n$.

If the communication channel is ideal the final state $|\Psi(T) >_n$ transmitted to the *nth* spin should coincide with $|\Psi(0) >_1$. For real chain, the efficiency of transmission of quantum state is limited and quantified by the $fidelity$, defined as the overlap between $|\Psi(T) >_n$ and $|\Psi(0) >_1$.

The physical realization of the steps enumerated above implies some prerequisites both in the experimental capabilities and in the properties of the molecules. For example, given a molecular spin ring or chain, the initial pure state requirement is fulfilled if the molecule is in its well defined ground state. Thus it is needed a molecule with ground state well separated (by Δ) with respect to the first excited one and the possibility to work at a temperature lower than Δ. To actuate the second step, it is necessary to be able to modify the state of the first spin without perturbing the rest of the chain. This can be achieved if the manipulation of s_1 is on a timescale short as compared to the coupling between the first spin and the rest of the chain. Referring to real systems, suitable candidates can then be heterometallic AF spin rings or chains where the extra spins at the edges should have exchange constants J smaller respect those between the elements within the channel. The last step requires the capability of locally reading out the state of the *nth* spin. Some strategy of local probing were recently developed exploiting chemical selectivity of experimental techniques such

as NMR [21,22] and X-ray spectroscopy [98,99]. This again makes heterometallic molecules suitable systems. However, these methods are probes of static properties; while, in order to probe the coherent dynamics, time resolution is also required. Besides and most important, prerequisite to all the listed operations is that the decoherence time of the molecule should be longer than the operation time.

1.4 Theoretical Background on solid state physical properties

In order to study the issues mentioned in the previous sections, the magnetic features of molecular spin clusters were investigated by means of specific heat and magnetization measurements. Hereafter the theoretical background of these experimental techniques is reported.

1.4.1 Specific heat

The specific heat C of a given material represents the heat per unit mass (or mole) necessary to increase by a degree the temperature of the material: it is defined as the derivative of the internal energy U with respect to the temperature T:

$$C = \frac{\partial U}{\partial T}. \tag{1.9}$$

From its definition it is clear that the specific heat can provide a great deal of information over all the possible excitations: electronic, vibrational, magnetic, nuclear, etc. [100–102] In the case of molecular magnets it is the result of several contributions, but the predominant are given by the lattice vibrations C_{latt} and the magnetic part C_{mag} [103–107].

Lattice Contribution

Molecular clusters typically contain a few hundreds of atoms that are in a perfectly embedded crystalline arrangement. From the classical theory, in a perfect crystal containing N atoms per unit cell, the internal energy of the lattice is

equivalent to the energy of a system of $3N$ independent harmonic oscillators. The classical expression for the specific heat, due to Dulong and Petit and valid only at high temperature, is $C = 3NR$, where $R = 8.314$ JK^{-1}mol^{-1} is the gas constant. This implies that for the hundreds of ions per cell molecule-based materials the lattice contribution at high temperatures saturate to the huge $3NR$ value. Even at cryogenic temperatures C_{latt} is still substantial and, since it grows very fast with the temperature, at ~ 10 K the lattice contribution becomes already preponderant obscuring most of the features of the magnetic one, thereby limiting the accuracy to which it can be determined.

To have a realistic expression for the temperature dependence of the specific heat we need to refer to the quantum mechanics and to the concept of quantized vibration modes (phonons), obtaining:

$$C_{latt} = \frac{\partial}{\partial T} \sum_{\mathbf{k},s} \frac{\hbar\omega_s(\mathbf{k})}{e^{\beta\hbar\omega_s(\mathbf{k})} - 1} \tag{1.10}$$

where $\hbar\omega_s(\mathbf{k})$ is the energy related to the s-th normal mode with wavevector $\mathbf{k}$. The details of the spectrum of the phonons can be quite complex due to the huge number of independent vibration modes. More manageable approximations are the models due to Einstein and Debye. The Debye model replaces all the branches of the vibrational spectrum with three acoustic branches, giving the so called Debye contribution (C_D). The Einstein model instead accounts for $(3N-3)$ optical branches that are responsible for the corresponding Einstein contribution (C_E). Thus, the lattice specific heat turns to be: $C_{latt} = C_D + C_E$. Within molecular magnets, the intra-cluster interactions between the ions are quite strong, while the coupling between different clusters are much weaker (the molecular crystals are formed through van der Waals bondings). Correspondingly, high- and low-energy branches are both present in the phonon spectra of the isolated molecules, giving rise to Einstein modes that can be broadened in energy by intermolecular interactions. The expressions for the Einstein and Debye contributions are respectively:

$$\frac{C_E}{R} = 3r \left(\frac{T_E}{T}\right)^2 \frac{\exp\left(\frac{T_E}{T}\right)}{\left[\exp\left(\frac{T_E}{T}\right) - 1\right]^2} \tag{1.11}$$

where T_E is the Einstein temperature such that $\varepsilon_E = k_B T_E$ is the energy of the

optical phonon mode, and

$$\frac{C_D}{R} = 9\left(\frac{T}{\Theta_D}\right)^3 \int_0^{\Theta_D/T} \frac{x^4 e^x}{(e^x-1)^2} dx, \tag{1.12}$$

where $x = \hbar\omega/k_B T$ and $\hbar\omega_D = \hbar c k_D = 2\pi k_B \Theta_D$, is the Debye energy for which the characteristic linear dispersion $\omega_D = c k_D$ of the acoustic branch is assumed, with c the velocity of sound. For the temperature region $T \lesssim \Theta_D/50$, i.e. at considerably lower temperatures than predicted by Debye approximation, Eq. 1.12 can be reduced to:

$$\frac{C_D}{R} = 234\left(\frac{T}{\Theta_D}\right)^3. \tag{1.13}$$

In practice in molecular materials there are significant deviation from the conventional Debye $C \sim T^3$ law. In the temperature range of $0.1 - 20$ K the typical behavior of the lattice contribution is $C_{latt} \propto T^\alpha$ with $\alpha \sim 2.6 - 3$ and Θ_D values range between 15 and 50 K. These Θ_D values are much lower than what is usually found for insulating solids or intermetallic compounds ($\Theta_D = 150 \div 600$ K in these cases).

The temperature range of interest in the study of molecular magnets is $T \lesssim$ 10 K. In this case, the lattice contribution is mainly due to the acoustic branches, so to C_D, but low energy optical vibration modes may contribute as well. To estimate C_D it is possible to use a phenomenological expression [106]:

$$\frac{C_D}{R} = \frac{234 r T^3}{\left(\Theta_D + \delta T^2\right)^3} \tag{1.14}$$

where the parameter r is fixed by the system taken into account and equal to the number of atoms per molecule; while Θ_D and δ are determined by least square fitting. This last expression will be used extensively for the analysis of the lattice contribution of heat capacity in the result chapters.

Magnetic Contribution

The magnetic contribution arises from the eigenstates E_i of the magnetic part of the Hamiltonian:

$$C_{mag} = \frac{\partial}{\partial T}\langle \mathcal{H}_{mag} \rangle. \tag{1.15}$$

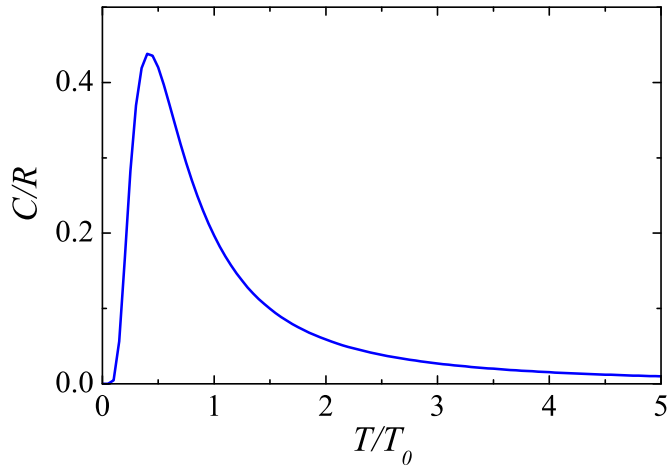

Figure 1.6: Two-levels Schottky anomaly calculated in the case $g_0 = g_1 = 1$ for a fixed magnetic field. The peak is maximum in correspondence of $T \sim T_0/2$

Assuming a canonical Boltzmann distribution describing the population of the electronic levels, in the simplified case of a two-level system, we obtain for the specific heat the well known Schottky anomaly expression [104]:

$$\frac{C_S}{R} = \frac{g_0}{g_1}\left(\frac{T_0}{T}\right)^2 \frac{\exp\left(\frac{T_0}{T}\right)}{\left[1+\frac{g_0}{g_1}\exp\left(\frac{T_0}{T}\right)\right]^2} \tag{1.16}$$

where g_0 and g_1 are the degeneracies of the ground and the first excited state, respectively, and $k_B T_0$ is the energy gap between these states. If $g_0 = g_1 = 1$ the Schottky anomaly has a characteristic maximum at $T \sim T_0/2$, so the energy gap $k_B T_0$ can be immediately visualized by looking at the temperature at which the anomaly exhibits its maximum, as visible in Fig. 1.6.

In the case of magnetic systems with many levels E_i the expression 1.16 can be generalized as:

$$\frac{C_{mag}}{R} = \beta^2 \frac{\sum_i E_i^2 \exp\left(-\beta E_i\right) \sum_i \exp\left(-\beta E_i\right) - \left[\sum_i E_i \exp\left(-\beta E_i\right)\right]^2}{\left[\sum_i \exp\left(-\beta E_i\right)\right]} \tag{1.17}$$

where $\beta = 1/k_B T$. This expression is commonly used to describe the magnetic contribution in molecular magnets. For instance, if the distribution of the lowest lying eigenstates is known by diagonalization of the Hamiltonian, C_{mag} can be

easily calculated. Alternatively, one may introduce one or a few parameters describing the magnetic system and fit the specific heat data to fix them.

For molecular spin clusters, Schottky anomalies can be due to energy gaps between different multiplets (generally tens of Kelvin) or between the levels belonging to same multiplets (typically up to few K). The zero field splitting (ZFS) within the multiplets of the ground state, as example, is manifested by a Schottky anomaly in zero field curve and, from its fitting, information on the anisotropy of the molecule can be obtained. Another example is the case of interacting $S = 1/2$ molecules (reported in Chapters 6 and 7), here the presence of a Schottky anomaly at zero field is an evidence of inter-clusters coupling and can give an estimation of its intensity.

1.4.2 AC-DC Magnetometry

The magnetization of a material is defined as the magnetic momentum per unit of volume. Using statistical mechanics, it is possible to demonstrate that, for a multilevel system at the thermal equilibrium, the magnetization is given by [60]:

$$M = k_B T \frac{\partial ln Z}{\partial H} \tag{1.18}$$

with Z the partition function. For a paramagnetic system with total spin momentum S the partition function is:

$$Z = \sum_{ms=-S}^{S} \exp(m_S g \mu_B H / k_B T),$$

where $\mu_B = 0.671$ JT^{-1} is the Bohr magneton, $k_B = 1.381 \times 10^{-23}$ JK^{-1} the Boltzmann constant and g is the g-factor. In this case, can be demonstrated that the magnetization follows the Brillouin function:

$$\frac{M}{N_A \mu_B} = gS \left[\frac{2S+1}{2S} \coth\left(\frac{2S+1}{2S} x \right) - \frac{1}{2S} \coth\left(\frac{1}{2S} x \right) \right] \tag{1.19}$$

where

$$x = \frac{g \mu_B S H}{k_B T} \tag{1.20}$$

The magnetic susceptibility is the response of a material to an applied magnetic field and is defined as:

$$\chi = \frac{\partial M}{\partial H} = k_B T \frac{1}{Z} \frac{\partial Z}{\partial H} \tag{1.21}$$

In presence of a gradient of magnetic field, diamagnetic substances are subjected to a force directed opposite to the gradient, while paramagnetic materials are subjected to a force directed like the gradient. Consequently, from the above expression, the susceptibility for diamagnetic materials is negative, while for paramagnetic systems is positive. Furthermore, the paramagnetic susceptibility is generally independent of temperature and field, while in the case of paramagnetic systems using the Brillouin expression 1.19, Eq. 1.21 simplifies to the Curie law:

$$\chi = \frac{N g^2 \mu_B^2}{3 k_B T} S(S+1) = \frac{C}{T} \tag{1.22}$$

The χ is field independent as long as one works at small fields and not too low temperature, where the condition $g\mu_B H \ll k_B T$ is satisfied. It's very common to report the product χT to have directly the value of S and g for paramagnetic materials or conversely to highlight deviations from the paramagnetic constant value C. In the case of **antiferromagnetic spin clusters** the dominant contribution of the Hamiltonian, as seen in the previous chapter, is the Heisenberg term $\mathcal{H}_{ex} = \sum_i J_i \mathbf{S}_i \cdot \mathbf{S}_{i+1}$ and, for T above few degrees K, χT can be quantified with:

$$\chi T = \frac{N_A g^2 \mu_B^2}{3 k_B} \frac{\sum_i S_i(S_i+1)(2S_i+1) e^{\epsilon(S_i)/k_B T}}{Z} \tag{1.23}$$

where the sum is over all the spin-multiplets eigenstates $\epsilon(S_i)$ of the Heisenberg exchange interaction $\mathcal{H}_{ex}$. A well known example is the Bleany-Bowers equation [108] for two isotropically coupled $s = 1/2$ spins, like a dimer of Cu^{2+} for instance, in this case the eigenstates correspond to total spin states $S = 0$ and $S = 1$ [26] separated by J, thus the magnetic susceptibility reads:

$$\chi T = \frac{2 N_A g^2 \mu_B^2}{k_B (3 + e^{-J/k_B T})}. \tag{1.24}$$

In this case the only adjustable parameters are J and g.

An important parameter to calculate the magnetization $M(H)$ is the magnetic anisotropy that can be associate to the axial zero-field splitting parameter D and have to be included considering the orientation respect to the magnetic field. A rather precise estimation of D can be obtained also working on powder samples by analyzing the field dependence of the magnetization at low temperature.

The measurement of the susceptibility can be performed by using the dc or ac methods. For the measurement of static magnetic properties they give the same outcome, namely Eq. 1.21. For time-dependent phenomena, the ac-susceptibility has the useful feature to allow the measurement of both the real, or *in-phase*, component χ', and the imaginary, or *out-of-phase*, component χ'' of the complex susceptibility,

$$\chi = \chi' + i\chi''. \tag{1.25}$$

The magnetization resulting from an applied dc-field H_0 plus an oscillating field $H_{ac} = he^{i\omega t}$ with frequency ω, is given by:

$$M = M_0 + \chi h e^{i(\omega t+\phi)} \tag{1.26}$$

where the equilibrium magnetization is indicated by $M_0 = \chi H_0$ and ϕ is the dephasing between the excitation and the response of the system. Within the linear response approximation [109], the approach of the magnetization $M(t)$ to M_0 after a field change is characterized by exponential variation with time:

$$M = M_0(1 - e^{-t/\tau}) \tag{1.27}$$

where τ is the spin-lattice relaxation time.

In the Néel-Brown model, the relaxation time for superparamagnetic particles with uniaxial anisotropy barrier $E_a = KV$, being K the anisotropy constant (of magnetocrystalline or shape origin) and V the volume of the particle, follows the Arrhenius law:

$$\tau = \tau_0 \exp\left(\frac{E_a}{k_B T}\right) \tag{1.28}$$

that is typical of thermal activated processes. For a superparamagnetic system the factor τ_0 typically ranges between 10^{-8} and 10^{-10} s. When the inter-particle interactions are non-negligible, the Arrhenius law is no longer valid. A phenomenological expression, the so called Vogel-Fulcher law, reads:

$$\tau = \tau_0 \exp\left(\frac{E_a}{k_B(T - T_0)}\right) \tag{1.29}$$

where T_0 is a measure of the interaction strength among the nanoparticles.

Chapter 2

Experimental methods and theory of measurements

This Chapter is devoted to the experimental tools I have used during my PhD work to carry out the measurements shown in the next part. The chapter is organized as follows. In section 2.1 the low temperature set-up is presented, while sections 2.2, 2.3 and 2.4 concern specific heat, ac-dc magnetometry and the Hall probe magnetometry, respectively. For each technique, theory of measurements and experimental details are reported. Finally, section 2.5 is devoted to the development of a new set-up for Hall probe measurements under radio frequency (RF) and laser excitation.

2.1 Low temperature set-up

In order to investigate the quantum behavior of molecular spin clusters, all the measurements are performed at low temperature. The commercial cryogenics system I have principally used is the Quantum Design *Physical Properties Measurements System* (QD-PPMS). Another setup, made by Oxford Instruments (OI), that I have developed for measurements under radio frequency electromagnetic excitation, is described in section 2.5.

The QD-PPMS, sketched in Fig. 2.1, is an automated workstation that allows to perform a variety of experiments requiring fine setting of the thermal control in the temperature range $1.9 - 400$ K. Using the ^{3}He refrigerator the temperature

Figure 2.1: Sketch of the Quantum Design PPMS cryogenic dewar with the 7T superconductive magnet (right) and its controller (left).

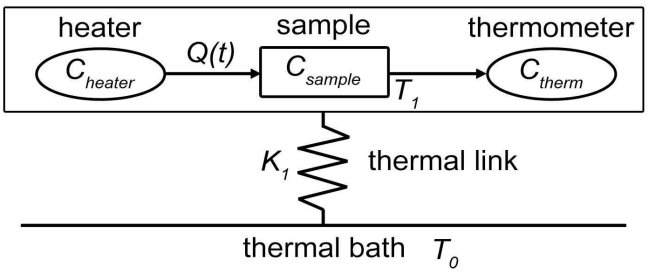

Figure 2.2: Sketch of the calorimeter constituted by a platform with a heater and a thermometer. The sample is supposed to be in excellent thermal contact with the calorimeter; the whole system is thermalized with the thermal bath via the thermal conductance K_1.

available goes down to 0.3 K. A superconducting coil allows to apply a magnetic field up to ± 7 T. All the specific heat, ac susceptibility and magnetization data presented in the result part were obtained performing the experiments with QD-PPMS system.

2.2 Specific heat and calorimetry

2.2.1 Theory of Measurement

To measure the specific heat it is necessary to read the response of the system in terms of temperature changes after a controlled quantity of heat has been supplied. The instrument apt to realize this kind of experiment is the calorimeter, that essentially is constituted by a platform with an heater to provide the heat $Q(t)$ and a thermometer to read the temperature $T(t)$. In principle, the simplest way to perform a specific heat measurement was by decoupling the sample from the surrounding. This type of experiment is however seriously affected by the non-perfect adiabatic condition. The wires of the thermometer and of the heater, as well as the sample holder, are responsible for the thermal leak. To obviate this problem another method was proposed and developed by Bachmann in 1972 [110], the *relaxation method*, where the thermal link of the sample with the thermal bath is taken into account, as schematized in Fig. 2.2. A heat pulse is sent to the sample and this results in a sudden temperature increase of the sample. Due to thermal link with the thermostat the temperature goes back to the equilibrium value. The relevant quantity is the total heat capacity measured $C_{tot} = C + C_{add}$, being C the heat capacity of the sample and C_{add}, *add* stands for *addenda*, the heat capacity of the calorimeter. The latter gives a small but finite contribution to C_{tot} and its value is given by the sum of the heat capacity of the single components of the calorimeter, $C_{add} = C_{holder} + C_{heater} + C_{therm}$, that in first approximation can be assumed in excellent thermal contact. If the heat pulse gives a temperature increase which is small compared to the sample temperature, the time dependence energy balance of the system can thus be written:

$$\frac{\partial Q(t)}{\partial t} = K_1(T)(T_1 - T_0) + C_{tot}(T)\frac{\partial T_1(t)}{\partial(t)} \tag{2.1}$$

where the term on the left is the rate of heat dissipated by the heater, the first term on the right is the heat flowing through the thermal conductance K_1 from the system to the thermal bath and the second term on the right is the heat used for the temperature variation of the system (sample + addenda). T_0 is the fixed temperature of the thermal bath while $T_1(t)$ is the actual temperature of the system (sample + addenda) that is time-dependent. Since $K_1(T)$ and $C_{tot}(T)$

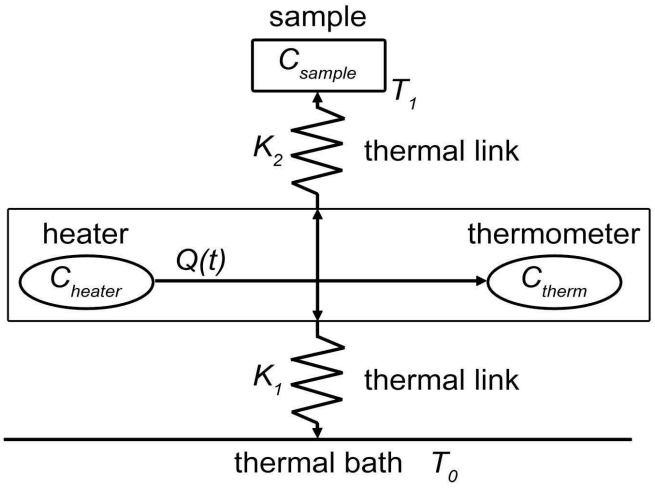

Figure 2.3: Sketch of the calorimeter in more realistic situation where the sample is thermally linked to the calorimeter via a second thermal conductance K_2

are functions of T, the differential equation 2.1 is in general non-linear. It can be nevertheless linearized assuming that $Q(t)$ is small and it gives limited variations of T_1. In this case $K_1(T)$ and $C_{tot}(T)$ can be expanded in power series of T and limited to the lowest order.

Different solutions of Eq. 2.1 are possible with a convenient choice of the thermal conductivity K_1 and of the time dependence of the heat $Q(t)$ [107]. A particular solution is obtained when:

$$\frac{\partial Q}{\partial t} = P\Theta(t - t_0) \tag{2.2}$$

(step like heat signal starting at $t = t_0$) and K_1 is finite. The solution results therefore:

$$T_1 - T_0 = \frac{P}{K_1(T)} e^{-\frac{t-t_0}{\tau_1}} \tag{2.3}$$

where $\tau_1 = C_{tot}/K_1$ is the relaxation time. τ_1 can be obtained fitting the exponential relaxation of $T_1(t)$ afterwards the pulse $Q(t)$, while K_1 can be measured directly, thus allowing to calculate C_{tot}.

Organic materials have often a bad thermal conductivity, so the approximation of Eq. 2.1 is no longer valid. Fig. 2.3 displays a more realistic model of the calorimeter stage, where a finite K_2 is considered, that accounts both the physical

link between sample and holder block, and the rate of internal equilibrium of the sample; establishing an internal relaxation time $\tau_2 = C/K_2$. The Eq. 2.1 should be extended as [111]:

$$\frac{\partial Q}{\partial t} = C_p \frac{\partial T}{\partial t} + K_2(T_p - T_1) + K_1(T_p - T_0) \tag{2.4}$$

$$0 = C_s \frac{\partial T_1}{\partial t} + K_2(T_1 - T_p) \tag{2.5}$$

where C_p and T_p are the heat capacity and temperature of the platform. C_s and T_1 are the heat capacity and temperature of the sample. To get the solution of Eq. 2.5, one may use curve fitting method (CFM). The procedure is rather complicate, and one can find more detail in reference [112]. In the limit $\tau_1 > \tau_2$, the temperature rise (or decay) following a heat pulse is essentially given by the sum of two exponentials, when the constant heating power is on or off:

$$T = A_1 \exp(-t/\tau_1) + A_2 \exp(-t/\tau_2) + C \tag{2.6}$$

The total specific heat can be analytically derived from the fit of the temperature relaxation with good precision, typically 1 or few per cent [112, 113]:

$$C_{tot} = \frac{P}{A_1 + A_2}(A_1\tau_1 + A_2\tau_2) \tag{2.7}$$

where P is the constant heating power. The above Eq. 2.7 expresses the two-tau relaxation method used by QD-PPMS for automatized heat capacity measurements.

2.2.2 Experimental setup

The calorimeter used in QD PPMS is shown in Fig. 2.4: the platform hosts the resistor-heater, that provides the heat pulse, and the thermometer, which measures the temperature displacement. In order to reduce the thermal conductivity toward the thermal bath (the cryostat), the platform is suspended and held by four thin wires and the sample chamber is evacuated to high vacuum (10^{-5} mBar). The sensitivity of the calorimeter is of about 1 nJ K^{-1} at $T = 2$ K.

The value of K_2 can be maximized by choosing flat samples with large base. Measurements were performed on powders and single crystals. The former were

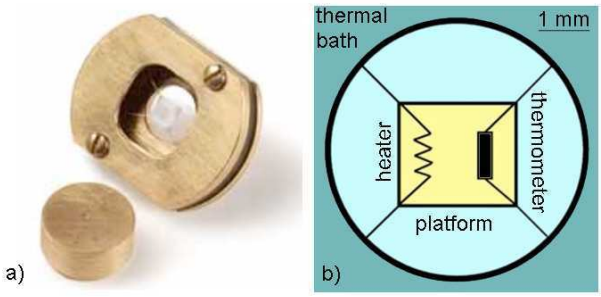

Figure 2.4: (a) The QD-PPMS calorimeter. (b) The calorimeter holder hosts thermometer and heater. The link to the thermal bath is realized by four wires. The measurement is performed under high vacuum (10^{-5} Torr) to limit the conductivity toward the thermal bath.

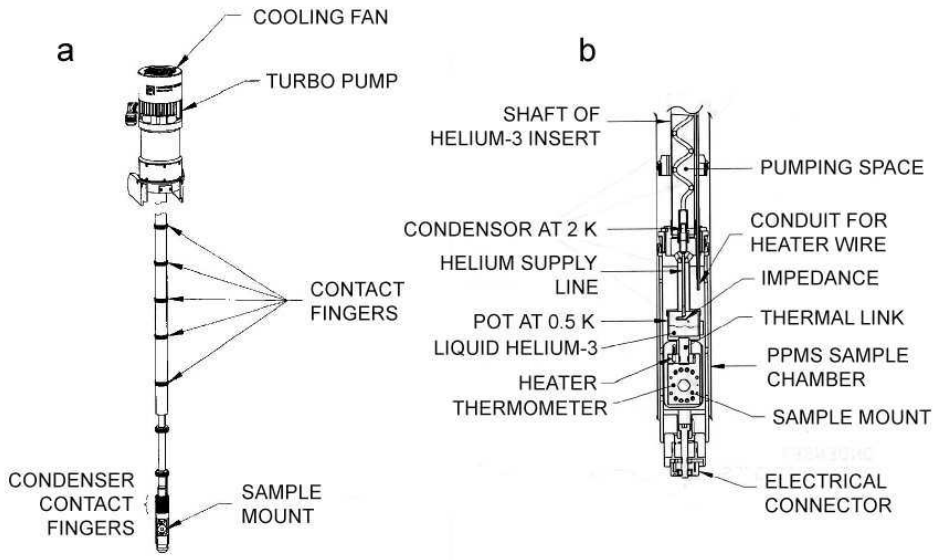

Figure 2.5: (a) The Quantum Design ^{3}He insert for the QD-PPMS cryostat. (b) Enlargement of the bottom side.

pressed ($\sim$ 100 Bar/Φ = 5 mm) to create thin pellets. The sample was glued to the calorimeter with Apiezon N grease.

The QD-PPMS achieves temperature down 0.3 K utilizing an additional ^{3}He refrigerator, sketched in Fig. 2.5. The closed-circulation system condenses ^{3}He in a reservoir linked to the specimen. Down to 0.5 K the reservoir is continuously refilled, whereas the ^{3}He gas must be completely condensed to achieve 0.3 K, so the base-line temperature is kept no longer than one hour before re-cycling.

Units. Data acquired by the PPMS calorimeter are given in units of μJ K^{-1}. To obtain the molar heat capacity and then normalize the data to the molar gas constant R this simple equation can be used:

$$C/R = C(\mu\text{J K}^{-1}) \times \frac{\text{molar mass(g mol}^{-1})}{\text{sample mass(g)}} \times \frac{10^{-6}}{R(\text{J mol}^{-1}\text{ K}^{-1})} \tag{2.8}$$

where R=8.314 J K^{-1} mol^{-1}.

2.3 QD AC-DC Magnetometer

The magnetization and susceptibility measurements presented in this thesis work were performed by means of QD-PPMS magnetometer (ACMS), that allows both ac and dc measurements in the temperature range $1.9 - 400$ K. As depicted in Fig. 2.6, the magnetometer consists in a set of coils inserted in the main dc superconducting magnet ($0 - 7$ T).

dc-measurements are performed by means of the extraction method [111]. The magnetic field is applied by the dc-superconducting magnet and the sample is moved by a servo motor through the two detection coils, thus inducing a voltage signal proportional to the magnetic moment.

ac-susceptibility is measured providing an oscillating excitation field with frequency in the range 1 Hz-10 kHz and typical amplitude 10 Oe. The excitation field is provided by the ac-drive coil, the change in magnetic flux is detected positioning the sample into each of the two secondary coils. To reduce the interaction with the environmental materials outside the measurements region (chamber walls, magnet core etc.), a compensation coil is used to confine the excitation field within the sample space. The compensation coil is counter wounded outside the

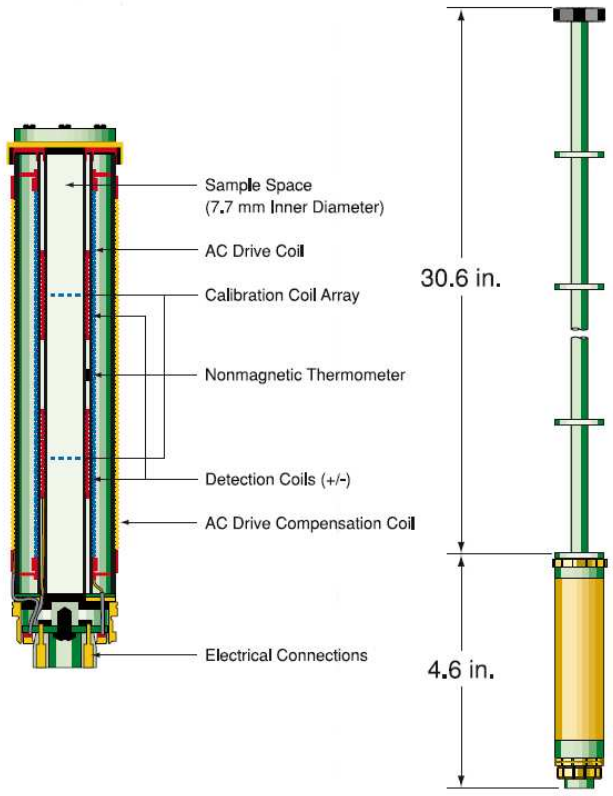

Figure 2.6: (a) The QD-PPMS *ac-dc* magnetometer. (b) Section of the bottom part.

drive coil and supplied with the same ac-current. It thus generates a magnetic field opposite to the excitation one, which has the effect to downgrade the rank of the field from dipolar to quadrupolar. Quantum Design ACMS set also employs special calibration coils to precisely remove phase shifts coming from the detection apparatus and effectively separate sample signal from instrumentation effects. The minimum detectable magnetic moment is of about 10^{-7} emu.

Units. Data measured by the QD-PPMS acquisition software are given in units of emu, whereas the molar susceptibility χ and magnetization M are usually expressed as emu mol^{-1} and μ_B/f.u. respectively. The necessary transformations are:

$$\chi(\text{emu mol}^{-1}) = \chi(\text{emu}) \times \frac{\text{molar mass(g mol}^{-1})}{\text{sample mass(g)} \cdot \text{excitation field(Oe)}} \tag{2.9}$$

$$\text{M(DC)}(\mu_B/\text{f.u.}) = M(\text{emu}) \times \frac{\text{molar mass(g mol}^{-1})}{\text{sample mass(g)} \cdot \mu_\text{B} \cdot \text{N}_\text{A}} \tag{2.10}$$

where in c.g.s. units μ_B and N_A are defined as 9.274×10^{-21} erg G^{-1} and 6.022×10^{23} mol^{-1}, respectively. The unit erg G^{-1} is equivalent to emu.

2.4 Hall micro-probe magnetometry

2.4.1 Working principle: the Hall effect

If a current is flowing through a conductor thin strip and a magnetic field is applied perpendicular to the current direction, the trajectory of the carriers is deflected by the Lorentz force. The result is the Hall effect [100, 114], i.e. the appearance of a difference in the electric potential (known as Hall voltage V_H) at the extremes of the conductor transverse to the current. In a simple Drude model, in stationary conditions the electrostatic field along $\hat{y}$ is such that $eE_y = ev_xB_z$, with the current flowing along x with drift velocity v_x (see Fig. 2.7). The Hall voltage is thus given by

$$V_H = wE_y = v_xB_z = \frac{j_xB_z}{ne} \tag{2.11}$$

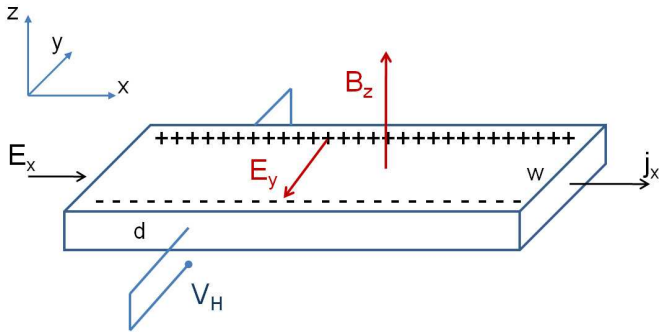

Figure 2.7: Sketch of the Hall effect in a conductive slab, the current is flowing through the material strip in the x-direction and a magnetic field **B** is applied along $\hat{z}$. The carries of charge q and drift velocity v are deflected by the Lorentz force toward the negative y-direction, generating the electrostatic potential E_y that prevents further accumulation and a potential V_H is found in the direction perpendicular to the current flux.

where w is the width of the conductor, j_x the current density along x and n the charge carriers density. Since $j = I/wd$ (d is the thickness), as final relation we obtained:

$$V_H = R_H I B_z \tag{2.12}$$

having defined the Hall coefficient R_H as:

$$R_H = \frac{E_y}{j_x B} = \frac{1}{ned} \tag{2.13}$$

The Hall voltage V_H turns out to be proportional to the magnetic field and the current, and inversely proportional to the carrier density n of the conductor. Thus, the Hall effect can be used to determine n and the sign of charge carriers in a material, that is related to the shape of the Fermi surface in the framework of electronic band theory.

2.4.2 Hall devices

If R_H is known by calibration, the Hall effect can also be used to measure the magnetic flux density of the field. The simplest geometry to exploit the Hall effect is a cross with the current channel perpendicular to the voltage channel, this configuration is also known as the *Hall cross*. If a magnetic object is placed

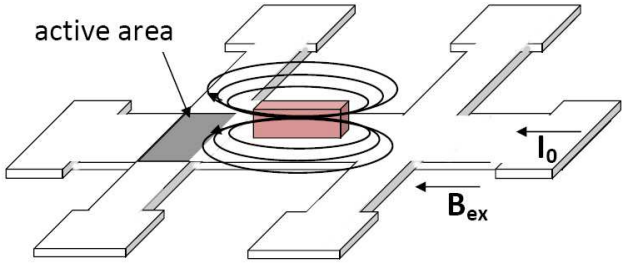

Figure 2.8: Sketch of the Hall probe devices and a typical sample mounting. The sample is magnetized by the external field $\mathbf{B_{ex}}$ and the flux of its stray field, proportional to the magnetization, is measured by the Hall sensor.

near the active area of the probe, i.e. near the center of the cross where the two channel intersect, then the Hall signal isproportional to the sum of the external field $\mathbf{B}_{ex}$ and the magnetic stray field coming from the sample and entering in the active area. Considering the geometry of Fig. 2.8, it can be seen that this field is related to the magnetization of the sample through geometrical factor. This constitutes the basis of the Hall probe magnetometry.

It has been calculated [115] that the Hall response is determined simply by the average of the magnetic field in the intersection between current and voltage leads, even in the presence of an extremely inhomogeneous field. Thus, Hall sensors are actually fluxmeters, as the case of SQUIDs magnetometers.

Sensitivity

The magnetic field sensitivity of a Hall sensor (usually indicated with B_{min}) expresses the minimum magnetic field, averaged in the whole active area, that can be detected. It is defined as the ratio between the Hall signal $V_H = IR_HB$ and the electrical noise present in the measurement.

$$B_{min} = \frac{\sqrt{V_{Johnson}^2 + IR_{noise}^2}}{IR_H} \tag{2.14}$$

where the two major contributions to the voltage noise are considered:

- $V_{Johnson} = \sqrt{4k_BTR_sf}$, where k_BT, R_s and f are thermal energy, series resistance of the device and the measurement bandwidth, respectively, is

the so called intrinsic or thermal noise and arises from the resistance of the voltage leads.

- IR_{noise}, is a resistive noise that manifests itself as telegraph noise in the time trace of the Hall signal and has a $1/f - like$ component in the frequency domains and it is probably due to fluctuations of the total resistance of the device [116].

As it can be seen in Equation 2.14, the Johnson noise can be suppressed increasing the value of the driving current I, but, above a certain value, the resistivity noise becomes the dominant one. In addition, also self heating effects (I^2R) impose constraints on the value of I. It turns out that there is an optimal value for the driving current (I_0, material dependent) that minimize the noise. Under this condition, B_{min} can be related to the physical parameters of the sensor, solving the equations that govern the behavior of the Hall effect [114, 117]. In particular [118]

$$B_{min} \propto \frac{1}{\sqrt{n\mu}w\sqrt{d}} \tag{2.15}$$

being n and μ the density and mobility of charge carriers and w and d the width and thickness of the probe. Generally speaking, the field sensitivity increases with the mobility of the conductors, while it worsens scaling down the size of the probe. This can be simply understood since smaller probes and material with low carriers mobility usually have shown high resistance values, thus increasing the sources of electrical noise.

Commercial high field resolution Hall probes are made of high mobility semiconductors. GaAs/AlGaAs has been widely employed for low temperature Hall magnetometry [119–121] for its extremely high signal to noise ratio. This originated by the desirable combination of small density n and high mobility μ of charge carriers. Until the lateral size of the probe is still in the micron range (in certain cases even hundreds of nm) magnetic signal of the order of 10^{-6} T can be easily detected, as reported in [116].

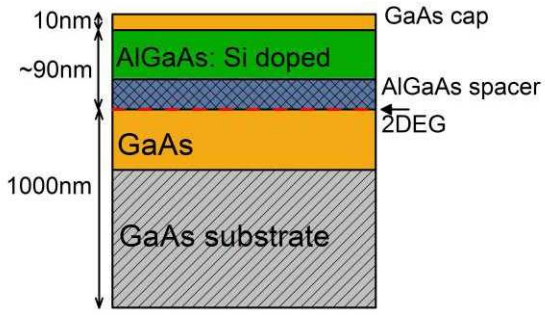

Figure 2.9: 2DEG structure of the wafers grown by MBE in the TASC laboratory, in Trieste. Starting from a commercial semi-insulating GaAs substrate, also a thick film of several microns is epitaxially grown to achieve good structure quality.

Fabrication details

During my thesis work, I produced and used GaAs/AlGaAs heterostructure Hall devices. The material, with a 2DEG below the surface, was grown by means of molecular beam epitaxy (MBE) by Dr. G. Biasiol at TASC in Trieste. I then fabricated the devices by optical lithography at NEST laboratory in Pisa, thank to a collaboration with Prof. L. Sorba and under the supervision of Dr. D. Ercolani and Dr. P. Pingue.

Figure 2.9 illustrates the profile of the wafers. At the interface between GaAs and AlGaAs charge carriers are confined in a sheet of narrow thickness, showing two-dimensional properties. Above this 2DEG there is an undoped $Al_{0.3}Ga_{0.7}As$ spacer layer, followed by silicon-doped $Al_{0.3}Ga_{0.7}As$, that acts as electron donor for the electron gas. The spacer is needed to reduce impurity scattering and hence it greatly improves the mobility. At top a GaAs cap is grown to prevent Al oxidation.

The fabrication procedure of devices is made by two principal steps. The first one is the photo-lithography and wet etching with H_3PO_4:H_2O_2:H_2O solution (in 3:1:50 ratio) to define the Hall bar shape (*mesa*) in the heterostructures. A second step of lithography is then employed to put ohmic contacts to allow electrical connections to the 2DEG. Contact pads are made by evaporation of Ni (10 nm), GeAu (100 nm) and Au (100 nm) followed by thermal annealing at high

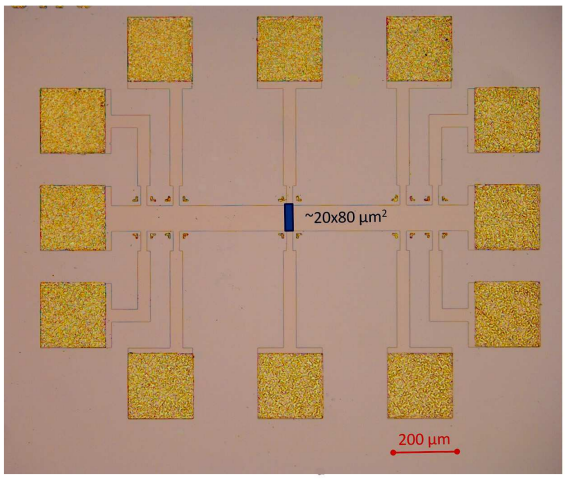

Figure 2.10: Optical microscope picture of an Hall device fabricated as explained in the text. The geometry of the probe allows to measure V_H up to five zones at the same time or samples with maximum length of about 900 μm .

temperature in a controlled nitrogen-washed atmosphere. During annealing Ge atoms diffuse deep in the wafer creating an ohmic electrical path to the electron gas. Figure 2.10 shows an optical microscope image of one final device realized, all the magnetometry measurements reported in the following are performed by using Hall probe of this type. In each device there is one principal (thicker) channel for the current and, perpendicular to this, other 5 channels for the voltage measurement situated at different distance, allowing experiments with sample till $\sim$900 μm length. The active zones (delimited by the intersection of the I with V channels) have an area of about 20x80 μm^2. Golden contacts have an area of about 200x200 μm^2. The 2DEG is situated at a depth of about 100 nm from the surface. Charge n=2.2x10^{11} (dark) and n=5.3x10^{11} (light); mobility μ=2.7x10^5 (dark) and μ=8.4x10^5 (light).

Sample mounting and experimental details

In order to optimize all probe magnetometry technique, some tricky aspects have to be taken into account, one of this is the sample mounting. Accurately positioning the sample in respect to the sensor is crucial indeed, to achieve good signal

coupling and hence perform sensitive measurements. The stray field originated by the sample's magnetization is maximum near the edge, and decrease rapidly with the distance ($1/r^3$ in the point dipole approximation). Thus the sample must be placed as close as possible to the probe's active area. A typical configuration is seen in Figure 2.8. Standard cryogenic grease (apiezon N) can be employed to glue the sample on the probe. Then the sample is moved to the desired position, for example using a thin and soft wire that works like a micro-tip.

Particular care has to be taken to avoid damages to the 2DEG, since it is quite near the surface: a simple scratch may be enough to irreversibly deteriorate the probe behavior.

Usually, a chip of sizes ≈2x2 mm^2 contains a small number (2-3) of almost identical Hall probes. The whole chip is glued to the PPMS resistance sample holder with silver paint, that assures good thermal contact. Shortcuts between different probes do not occur, since the substrate is made by several hundreds of microns of insulating GaAs. A Kulicke and Soffa Model 4123 Wedge Bonder [122] is used to connect contact pads of the 2DEG probe to the ones in the sample holder. Finally the sample holder is plug to the insert and placed in the PPMS cryostat to perform measurements.

Hall probes can be mounted on different inserts in the PPMS liquid helium cryostat: the standard Resistivity sample holder, the Horizontal Rotator probe or the ^{3}He system, this last with the advantage to achieve temperature down to 0.3 K. The measurements I present in the following are performed using an home-made insert, realized by Dr. Andrea Candini during is Ph.D. [123,124], compatible with the QD PPMS system. The improvement respect to the standard QD inserts is the presence of two coaxial cables for high frequency radiation and an optical fiber for laser. These allow to carry out Hall-probe magnetization experiments under external excitation of radio frequency electromagnetic radiation or coherent visible light.

The insert was designed to have the external field in the same plane of the sensor, thus in the geometrical configuration showed in Fig. 2.8. In this way the background signal is minimized (a small perpendicular component of the external field is always present due to not perfect alignment); in addition, this configuration avoid the occurrence of quantum effects at low temperature ($T <$

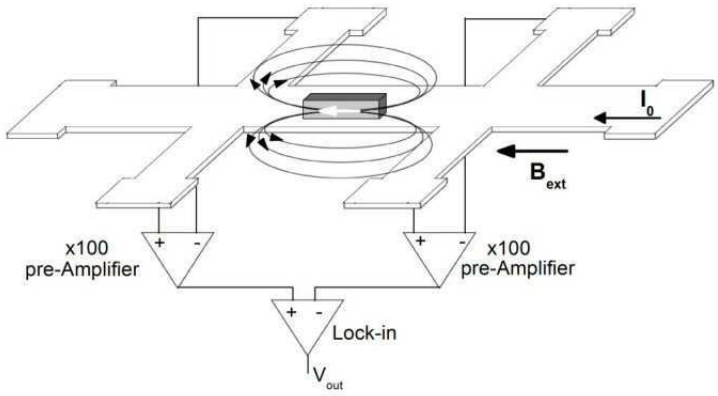

Figure 2.11: Sketch of the sample mounting and contacts configuration. Two active zones are measured at the same time: one with the sample and an empty one as reference to subtract the background. The difference of voltage $(V_+ - V_-)$ for each channel is obtained by a home-made differential amplifier. Then the resulting signals are subtracted by the lock-in.

10 K) since the effective field sensed by the Hall probe is relatively small.

The Hall voltage is proportional to the magnetic flux density perpendicular to the probe's active area. Thus the measured signal is the sum of the stray field proportional to the sample's magnetization and the z-component of the external field. To subtract this background contribution, also an empty reference probe can be connected and signals of both sensors are measured simultaneously, as depicted in Fig. 2.11. Since they belong to the same chip the two probes have very similar parameters and after subtraction only the signal from the sample is essentially left. Actually a small linear contribution may be still present, due to inhomogeneity of the charge density in the whole wafer. This is however a small error, typically of the order of 10^{-5} Ω/G.

Finally, two important observations about biasing and cooling. Typically, the optimal value for biasing our probe was around $10\mu A$ for ^{3}He temperatures, while it can be slightly higher (around $20\mu A$) for liquid helium temperatures up to $\approx$ 100 K. Currents of the order of tens of μA are expected for probes with sizes well above the micron scale.

Electron gas is a very sensitive element, and particular precaution have to be taken to optimize the performances of Hall measurements. Thermal shocks

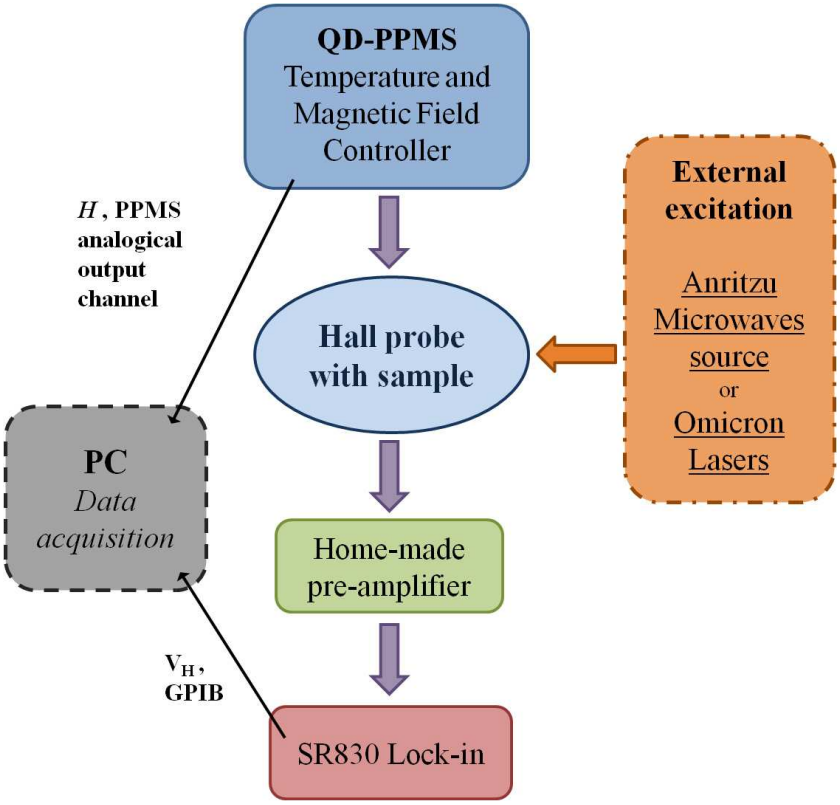

Figure 2.12: Schematic diagram of the experimental setup for Hall probe measurements under microwaves or laser excitation.

can seriously damage the probe; to avoid this problem, Hall devices have to be cooled and warmed very slowly, i.e. at a rate not higher than $2 - 3$ K/min and with a low value of the bias current (i.e. $I_0 < 1\mu$A). Exposing the sensor to visible/infrared light at low temperature can help to recover best performances, by releasing carriers trapped in defects and impurities. However, very unlikely a Hall probe can maintain good characteristics after few (4-5) thermal cycles and/or (2-3) sample mountings and it should be changed.

Measurements under radio frequency absorption

Magnetization measurements under resonant absorption are a great resource to study quantum effect in molecular clusters, like, for instance, the tunnelling of magnetization [8] and, more generally, it allows to have information concerning

the dynamics of the studied system using a stationary technique [125–127]. Moreover, with the present setup it remains open the possibility of further improvements of the system also for magnetization dynamics measurement like electron paramagnetic resonance [128–130].

The experimental configuration used for Hall probe magnetometry under external electromagnetic excitation is schematized in the diagram of Fig. 2.12. The sample is mounted, as described in the previous section, on the insert and located inside the QD-PPMS dewar, that controls both the temperature and the magnetic field. The probe is biased with an ac-signal coming from a voltage source with a high resistance in series, to assure good stability. Frequency of the signal is around 1 kHz and the amplitude is set to obtain $I_0 \sim 10\mu$A.

On the insert head, a home-made differential pre-amplifier is placed to amplify the Hall signal with a gain equal to 100, and performing subtraction between the two voltage leads. The system is built to measure up to four channels simultaneously. Two channels are connected as shown in Fig. 2.11; in this way, by subtraction of the two signals, contribution coming from the sample is enhanced, while background is minimized. These signals are then sent to a phase-locked system (Stanford Research Systems SR830 Lock In Amplifier), triggered with the voltage source, that also performs the final subtraction.

The external electromagnetic excitation is provided by Anritzu MG3692B signal generator, with frequency up to 20 GHz and power up to 20 dBm. The signal is transmitted through a coaxial cable that terminates straight directly to the sample position. This cable is a very thin (0.5 mm shield diameter) LakeShore CC-SR-10; furthermore, both the inner and outer conductors are made of stainless steel. This makes it ideal for low-temperature applications, however electrical losses are considerable, especially at frequency above few GHz.

Thank to the the presence of an optical fiber on the insert, also laser light can be transmitted to the sample and with the same setup for RF (see Fig. 2.12) is possible to perform Hall probe magnetometry under laser excitation. We have at our disposal two Omicron solid state laser in the visible light, respectively of 635 and 375 nm wave length.

Data acquisition is made by a labview program, that collects the V_H signal emerging from the Lock-in (interfaced via a GPIB with the computer) and the

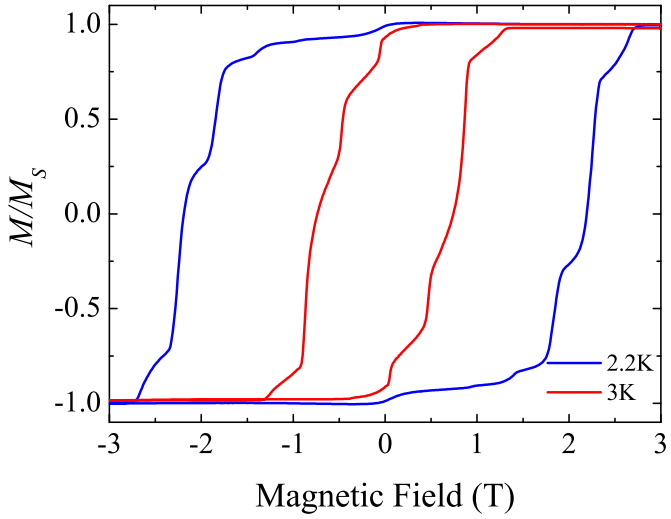

Figure 2.13: Magnetization hysteresis loop of Mn_{12} crystals measured at with Hall probe devices at $T = 2.2$ (blue) and 3 K (red). The curves are normalized to the value of saturation M_S.

magnetic field produced by the QD-PPMS, communicating via an analogical output channel.

Test measurements

To test the system I choose the well known single molecule magnet $Mn_{12}-$acetate [6, 7, 9]. This molecule is very suitable to check micro-Hall devices [131], indeed having high spin $S = 10$, we expect a strong magnetic signal. A ~ 100 μm-sized single crystal of Mn_{12} (synthesized by the group of Prof. A. Caneschi, Firenze) was glued on the top of a probe, orienting its long side (that corresponded to the easy axis of magnetization of the Mn_{12}-ac molecule) along the direction of the magnetic field and aligning its short side to the edge of the active area.

Figure 2.13 shows the magnetization hysteresis loop measured with Hall probe, without irradiating, at the temperatures of 2.2 and 3 K. The data are obtained subtracting a linear residual contribution of the devices with slope 0.14 mV/T, while the data are of the order of few mV, and normalizing to the saturation value M_S. The signal is very clean and the typical steps related to the quantum tunneling of magnetization [8, 11, 12] are clearly visible. The width of the hys-

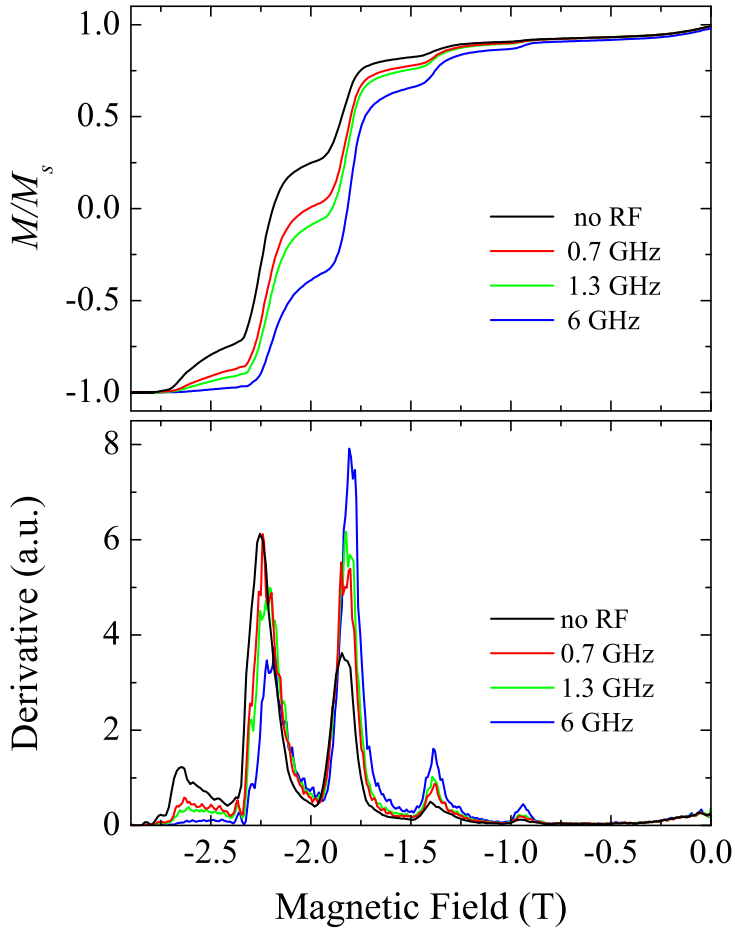

Figure 2.14: (Upper panel) Magnetization for Mn_{12} crystals at $T = 2.2$ K before irradiating (black) and while irradiating with continuum pulse of 0.7 (red), 1.3 (green) and 6 GHz (blue). (Lower panel) Derivative respect to the field of curves reported in the upper panel to enlighten the shift of the transition fields. For clarity only the data referring to decreasing field are reported.

teresis loops and the saturation magnetic field are in agreement with the values expected from literature.

In the upper panel of Fig. 2.14 the magnetization curves at $T = 2$ K for $Mn_{12}-ac$ while exciting the crystal with different frequencies, respectively of 0.7, 1.3 and 6 GHz are reported and compared with the curve without irradiation (black). As effect of irradiation, a shift is visible in the tunneling fields corresponding to the steps. This shift is enlightened by the derivative respect to the field, reported in the lower panel of Fig. 2.14. These results are similar to those reported in Ref. [132].

Concluding, the setup is working and can measure with good sensitivity magnetization of single crystals also under resonant absorption of radio frequency. To investigate a large class of molecular systems we need to extend the temperature range below 2.2 K, that is the limit of this setup. Indeed for an important part of molecular cluster at 2.2 K also the excited states are already populated and quantum phenomena like spin transition result hidden. In the next section I present a new setup that can achieve lower temperatures.

2.5 Development of the new setup

During the last year I have invested a part of the my Ph.D. activity in the installation of the new experimental equipment from Oxford Instrument (OI). Differently from QD, described in section 2.1, the OI system is not completely automated and the experiments should be realized and mounted by the users. The presence of the coaxial cables allows to excite the sample by means of radio frequency radiation (20 GHz$\sim$1K, typical gap between energy level in molecular spin rings). The presence of the triaxial magnet allows to change the orientation of the field respectively to the sample without moving this last one.

I was directly involved in the arrangement, in the assemblage and in the tests of the new instruments and in the realization of the setup for Hall probes magnetometry experiments. Specifically, I have designed and realized the sample holder and the electrical connections. Moreover, I have taken care of choice of the type of coaxial cables to run experiments with microwaves resonant absorption.

Referring to Fig. 2.15, the OI system is essentially constituted by a liquid

Figure 2.15: Oxford Instrument cryogenic setup: a) dewar with the triaxial magnet (9,1,1) T inside; b) ^{3}He cryostat Heliox-VL; c) magnets and ^{3}He needle-valve controllers.

helium dewar with a triaxial $(9, 1, 1)$ T magnet, a ^{3}He cryostat Heliox-VL with mounted microwave frequency coaxial cables, and the electronic controllers [133].

Heliox-VL

Heliox-VL is ^{3}He refrigerator insert that works mounted in a bath of liquid helium (^{4}He) in a suitable cryostat. Figure 2.16 illustrates the structure and the principal parts of Heliox-VL. At the top two experimental ports give line-of-sight access through the insert from room temperature to the sample space. Just below, it is situated a tank of about 2.5 liters with the charge of ^{3}He gas at a pressure of $\approx$ 2 bar. At the end of the sliding seal starts the Inner Vacuum Chamber (IVC), sealed by a greased cone seal, where the elements crucial for the cooling of the system are placed: the sorption pump, the 1 K plate and the ^{3}He pot (see Fig. 2.17(a)). The sample within the experiment is mounted on the base of the ^{3}He pot (see Fig. 2.17(b)).

The ^{3}He gas is free to circulate in the closed ^{3}He line that crosses the whole

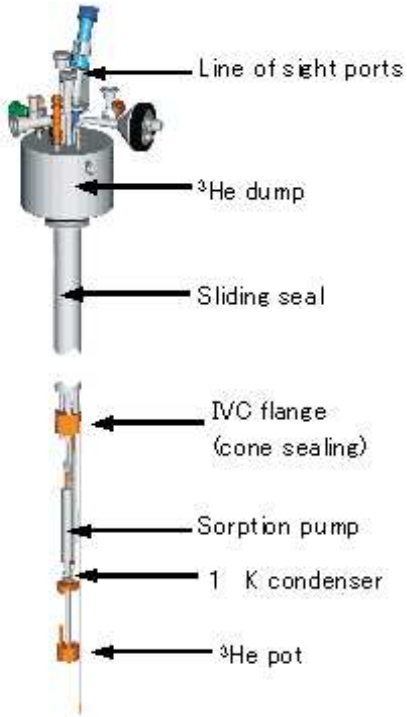

Figure 2.16: Sketch of the ^{3}He refrigerator Heliox-VL from Oxford Instruments. The principal parts are labelled.

insert, from the tank to the pot. In a separate line the liquid helium caught from the dewar can circulate. This line starts from the head probe, where a pump is mounted, crosses the sliding seal and IVC, where twists the 1 K plate and the sorption pump and terminates with a capillary external to the IVC. A *needle valve* (NV) regulates the opening of the capillary and thus the circulating quantity of liquid helium.

When the sample has been mounted and the IVC is fitted, the sample chamber is evacuated to a rough vacuum below 0.5 mbar (a rotary pump is sufficient) and a small amount of exchange gas, about 10 cm^3, is added to help the thermalization. This gas will be automatically absorbed by the Carbon sorption pump when the temperature goes below 30 K. At the same time, the ^{4}He line should be flushed (with NV completely open) and pumped (with NV closed) with helium gas few times. Finally, flushing with NV slightly open (about 20%) the insert is ready to be immersed in the liquid helium to initially cool the system.

Heliox-VL allows a temperature range from the base temperature ($\sim$ 250 mK) to room temperature, using two separate modes of operation. Briefly, for temperatures above 1 K, the ^{3}He pot is warmed directly by means of a heater and monitoring the temperature by a Cernox sensor. Conversely, below the 1 K plate temperature the refrigerator runs as a sorption pumped ^{3}He insert. Initially the ^{3}He sorb is maintained warm (approximately at 30 K) and ^{3}He gas is free to condense in the 1 K plate region and runs down to cool the ^{3}He pot and sample. The condensation takes about 20 minutes. After that, the heater on the sorb is switched off and the sorb, while cooling, starts pumping the ^{3}He gas. Reducing the vapor pressure above the liquid ^{3}He the temperature drops down to the base temperature.

The temperatures of 1 K and ^{3}He are controlled by an Oxford Instruments Intelligent Temperature Controller ITC503 (Fig. 2.15(c)). Further experimental details are available in Ref. [133].

The magnet

The magnet is placed at the base of the liquid helium dewar (Fig. 2.15(a)) and consists of three coaxial solenoids wound using multi-filamentary superconducting wire and disposed in way to have three magnetic fields along the orthogonal

directions **x**, **y** and **z**. These are controlled by three separate Intelligent Superconducting Magnet Power Supply (IPS-120-10), represented in Fig. 2.15(c). Switching on separately the superconducting magnets, the maximum magnetic field is 9 T along **z** and 1 T along **x** and **y**. Conversely, if the partial fields are switched at the same time, the total field can stay inside a cone generated by a vector with 9 T amplitude precessing around the **z** axis with an angle of 2°; or in a sphere with center in the origin and 1 T radius. After the first cooling, the maximum sweep rate for each solenoid is 1 T/min.

Mounting the experiment

For the Hall probe magnetometry, I have realized a removable sample holder in copper that is screwed to the copper rod supplied by OI and mounted at the base of ^{3}He pot (see Fig. 2.17(b)). The material of copper was chosen for its good thermal conductivity, indeed, to cool efficiently, it is crucial to have the sample well thermally anchored to ^{3}He pot.

The sample holder's geometry was designed to allow the use of the commercial QD ^{3}He puck for resistivity. This indeed has 8 golden pressure connectors spaced equally to the 8 QD puck pins, soldered via the two component Stycast 2850 FT by Emerson & Cuming with high thermal conductivity. In this way the Hall probes and the sample can be firstly mounted and bonded on the QD puck, as usual, and successively the QD puck can be fitted on the sample holder connected to the insert. Exploiting the 8 connections is possible to bond at the same time two simple Hall cross or up to three active zones for the same Hall probe.

On the back of the sample holder an hollow houses a 4-wires Ge thermometer to control the sample temperature. To have a good thermal contact the thermometer is fixed using apiezon N grease. In Fig. 2.18 the calibration of the thermometer obtained using the ^{3}He QD resistivity option is reported. In the upper panel is shown the resistivity of the thermometer versus temperature with zero field; while in the lower panel the magnetoresistence of the thermometer with the field for few temperatures is plotted.

Electrical connections are assured by 4 wires for the thermometer plus other 8 twisted cryogenic wires (Lake Shore WQT-36-25) for the Hall probe (soldered to the 8 golden connectors of the sample holder). These wires are soldered to a

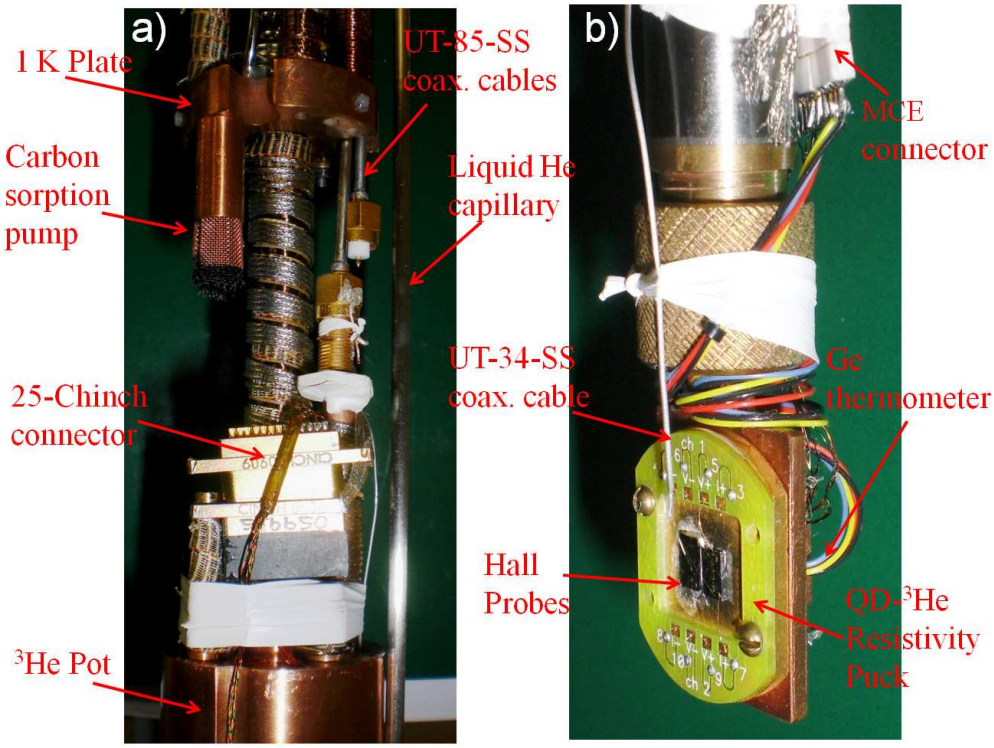

Figure 2.17: Picture of the open IVC a) between the 1 K plate and the ^{3}He Pot and b) at the sample holder extremity with the Hall probes and samples mounted. The principal elements are indicated.

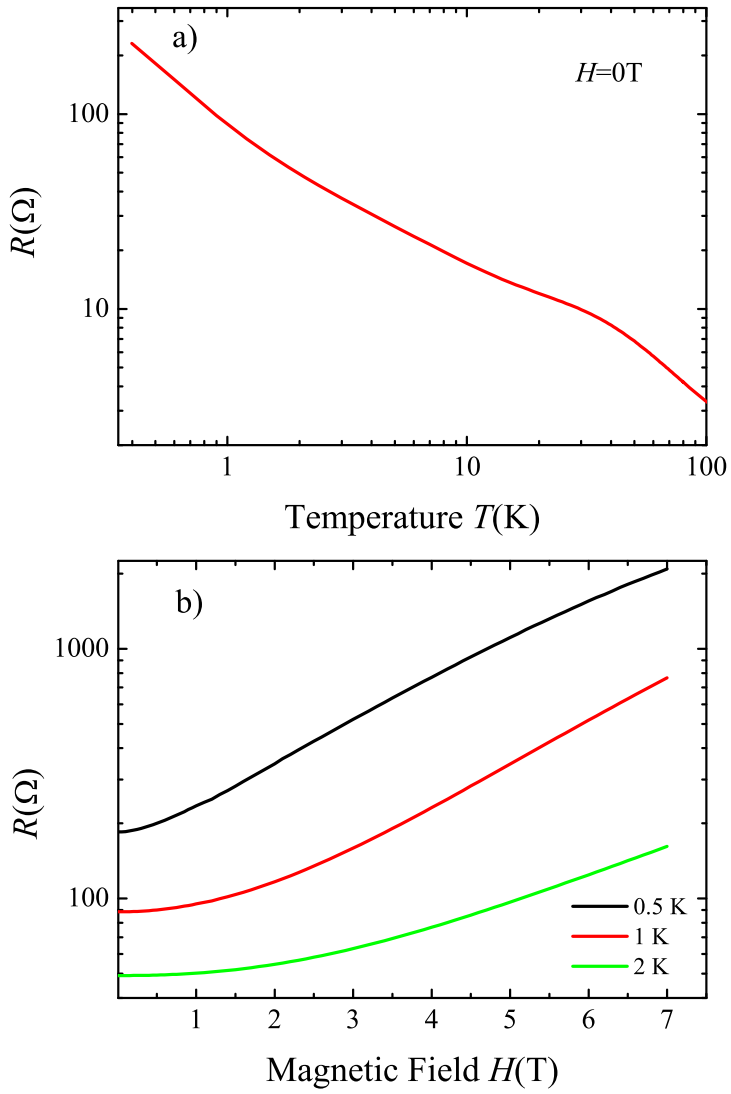

Figure 2.18: Resistivity of the 4-wires Ge thermometer a) against temperature with zero external field; b) versus field at 0.5 (black), 1 (red) and 2 K (green).

12 pins Microdot MCE golden connector thus constituting a first removable part (see Fig. 2.17(b)). From the MCE connector another stretch of 12 twisted wires passes through the cavity of the copper rod and finish to a 25-chinch connector provided by OI and situated on the top of the ^{3}He pot, this is the second and last removable part. Finally, from the chinch the wires arrived to a 24-way Fischer connector on the head of the insert.

In one line of sight port are mounted two Micro-Coax UT-85B-SS coaxial cables (at 20 GHz 6.94 dB/m insertion loss and 21.3 W power) that arrive just above the ^{3}He pot, terminating with SMA connectors adapted at 50 Ω. To these, other thinner coaxial cables Micro-Coax UT-34-SS-SS, with a lower heat power (at 20 GHz 7.52 dB/m insertion loss and 1.1 W power), can be screwed via the SMA connectors and transmit the electromagnetic excitation to the sample position. Moreover 4 standard flexible cables for high frequency are available.

The scheme of experimental setup is similar to those represented in Fig. 2.12 but with the OI system in the place of QD-PPMS. Data acquisition is made by the default labview program supplied by Oxford Instruments, and adapted for our setup.

Figure 2.19 presents preliminary results of Hall magnetometry performed with the new setup. The measurements were performed on Cr_8Cd single crystal at temperature $T \sim 0.5$ K and with the field along **z**. The signal is very clean and the steps expect from literature [134] are clearly visible. This demonstrates the operativity of Hall probe magnetometry with our new setup.

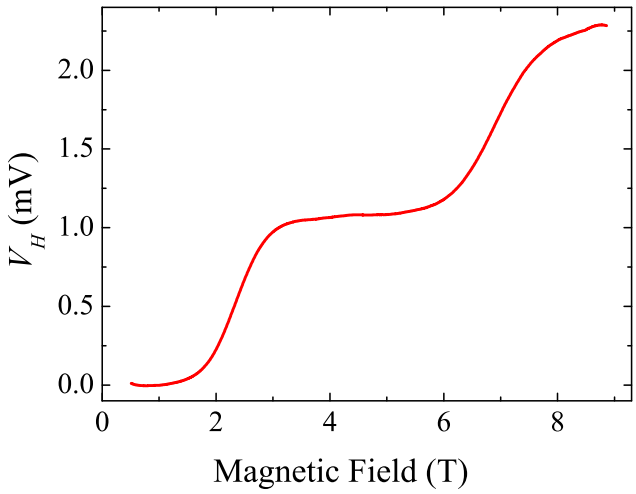

Figure 2.19: Preliminary results of Hall magnetometry with Oxford Instrument setup on Cr_8Cd single crystal at $T = 0.5$ K.

Part II

Results

Chapter 3

Closed spin rings: Cr_xCu_2 family.

Here a family of novel ring shaped molecular magnets Cr_xCu_2 is considered. These molecules are real systems of finite spin chains with two 'extra-spins'; they are indeed constituted by two identical antiferromagnetic chromium chains, of variable length, connected by two copper ions. The magnetic properties of these molecules are extensively investigated by susceptibility, magnetization and heat capacity experiments to characterize the systems and to find the effects of topology on the spin ground state. For the most 'manageable' molecules an effective model is proposed in order to quantify the microscopic parameters and to obtain the low-lying energy level pattern. Finally, an alternative model by spin-Hamiltonian diagonalization approach is reported for the smallest system.

The chapter is organized as follows. Firstly, in section 3.1 the structures and the chemical synthesis details for the various derivatives, produced by Dr. G. Timco within the group of Prof. R. E. P. Winpenny, are presented. In the successive 3.2 section I report the magnetic characterization by thermodynamic properties experiments performed at the *Low Temperature Lab* in Modena together with Dr. Alberto Ghirri. Lastly, in the subsection 3.2.1, the theoretical effective model and the spin-Hamiltonian one, made by Dr. Alberto Bianchi in Parma, are reported.

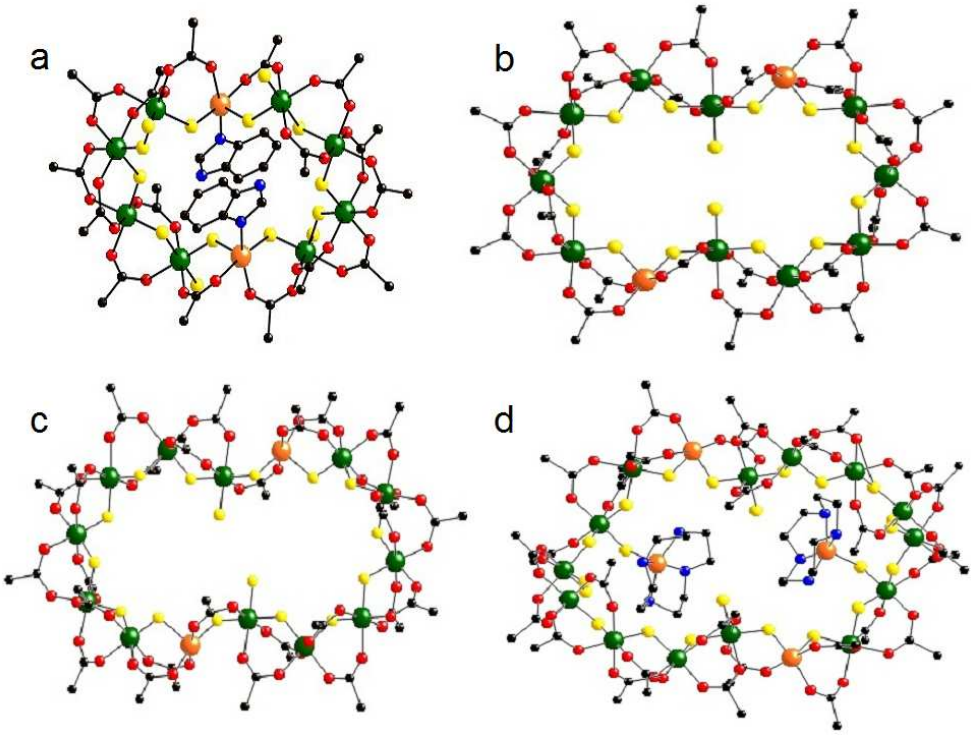

Figure 3.1: Crystallographic structure of (a) Cr_8Cu_2, (b) $Cr_{10}Cu_2$, (c) $Cr_{12}Cu_2$ and (d) $Cr_{14}Cu_4$ collected by X-ray diffraction. Colors: Cr: green, Cu: orange, F: yellow, O: red, C: black, N: blue. Hydrogen atoms and terminal Carbons in the pivalates groups are omitted for clarity.

3.1 Structures and synthesis details

The family investigated, namely Cr_xCu_2, is formed by four molecular rings each constituted by two twin chromium Cr^{3+} ($s = 3/2$) chains -of variable length- linked by two copper Cu^{2+} ($s = 1/2$) ions. Their chemical formulas are:

$$[HBz]_2[Cr_8Cu_2F_{14}(O_2CCMe_3)_{16}(Bz)_2],\ (Cr_8Cu_2 \text{ in short}),$$

$$[(C_8H_{17})_2NH_2]_2[Cr_{10}Cu_2F_{14}(O_2CCMe_3)_{22}],\ (Cr_{10}Cu_2 \text{ in short}),$$

$$[(Me_2CH)_2NH(C_2H_5)]_2[Cr_{12}Cu_2F_{16}(O_2CCMe_3)_{26}],\ (Cr_{12}Cu_2 \text{ in short}),$$

and

$$[CuC_8H_{20}N_4]_2[Cr_{14}Cu_2F_{22}(O_2CCMe_3)_{28}],\ (Cr_{14}Cu_2Cu_2 \text{ in short}),$$

The derivatives were prepared by Dr. G. Timco within the group of Prof. R. E. P. Winpenny, at *School of Chemistry* in Manchester. The chemical synthesis of Cr_8Cu_2 is described in Ref. [135] (compound 5).

$Cr_{10}Cu_2$ was obtained similarly to compound 1c in Ref. [135], by using the dioctylamine instead of the diethylamine. X-ray quality crystals were obtained by crystallization of the compound from a Et_2O/acetone mixture. The yield is 27%, the elemental analysis calculated(%) for $C_{142}H_{270}Cr_{10}Cu_2F_{14}N_2O_{44}$ is: Cr 14.35, Cu 3.51, C 47.08, H 7.51, N 0.77; while was found: Cr 14.69, Cu 3.50, C 46.81, H 7.72, N 0.74.

The molecule $Cr_{12}Cu_2$ was obtained similarly to compound 2 in Ref. [135], by using the N,N-Diisopropylethylamine instead of the Diisopropylamine and the heating was at 140°C for 8h. X-ray quality crystals were obtained by crystallization of the compound from toluene. In this case the yield is 30%, the elemental analysis calculated(%) for $C_{146}H_{274}Cr_{12}Cu_2F_{16}N_2O_{52}$ reads: Cr 15.82, Cu 3.22, C

44.45, H 7.00, N 0.71; while was measured: Cr 15.72, Cu 3.23, C 44.55, H 7.07, N 0.69.

Finally, $Cr_{14}Cu_2Cu_2$ was obtained similarly to compound 2 reported in Ref. [136], by using the copper carbonate instead of the nickel carbonate and the recrystallization was from hot acetone. The yield is 0.3%, the calculated elemental analysis (%) for $C_{156}H_{292}Cr_{14}Cu_4F_{22}N_8O_{56}$ reports: Cr 15.91, Cu 5.55, C 40.94, H 6.43, N 2.45; experimentally was found: Cr 15.37, Cu 5.26, C 39.97, H 6.68, N 2.33.

Figure 3.1 shows the crystallographic structures of the Cr_xCu_2 systems, resolved by Dr. R. Pritchard and Dr. R. Hayes in Manchester. In Cr_8Cu_2 each Cu–Cr edge is bridged by a fluoride and a pivalate, moreover each Cr adjacent to the copper sites have terminal fluorides attached to them. In all the other cases ($Cr_{10}Cu_2$, $Cr_{12}Cu_2$, $Cr_{14}Cu_2Cu_2$) the copper centers are bridged to two adjacent chromium ions differently: to one through one fluoride and two pivalates, and to the second through only one fluoride and one pivalate. Moreover, in the case of $Cr_{14}Cu_2Cu_2$ two extra copper ions are weakly anchored by cyclen group. The Cr–Cr edges are bridged by one fluoride and two carboxylates in Cr_8Cu_2, and by one fluoride and two pivalates in all the other derivatives. As result in all the systems antiferromagnetic exchange coupling between neighboring chromium spin centers is achieved. Concluding, Cr_8Cu_2, $Cr_{10}Cu_2$, $Cr_{12}Cu_2$ and $Cr_{14}Cu_2Cu_2$ can be regarded as couples antiferromagnetic chains, of four, five, six and seven chromium ions respectively, connected to two copper ions at the edges.

3.2 Magnetic characterization

Figure 3.2 shows the ac susceptibility for all the Cr_xCu_2 derivatives. The curves rise with the temperature and are progressively higher with the increasing dimension of the ring, i. e. the χT curve of $Cr_{10}Cu_2$ is above that of Cr_8Cu_2 and so on; as expected for increasing number of paramagnetic non interacting spins. At low temperature the susceptibilities for Cr_8Cu_2 (taken from Ref. [135]) and $Cr_{12}Cu_2$ converge to the same value, explicitly 1 emu K mol^{-1} (dashed line), as expected for a $S_0 = 1$ ground state. In the case of $Cr_{10}Cu_2$, the susceptibility at low T goes toward zero consistently with a $S_0 = 0$ ground state, as predicted by theoretical calculation at very low temperature reported in Ref. [137]. Finally, χT for

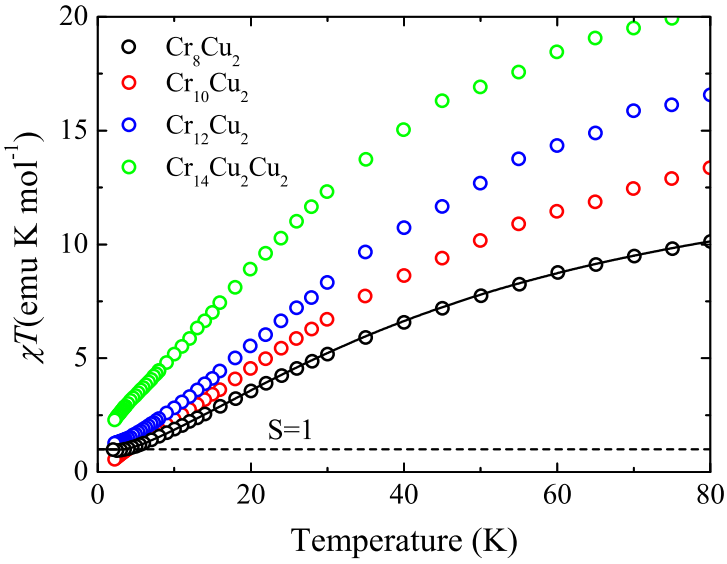

Figure 3.2: ac susceptibility product χT vs T measured for Cr_8Cu_2 (black) [135], $Cr_{10}Cu_2$ (red), $Cr_{12}Cu_2$ (blue) and $Cr_{14}Cu_2Cu_2$ (green). At low temperature Cr_8Cu_2 and $Cr_{12}Cu_2$ tend to saturate to the value 1 emu K mol^{-1} (dashed line), as expected for a $S = 1$ spin. Black solid line is the result of spin-Hamiltonian calculations for Cr_8Cu_2, as described in the text.

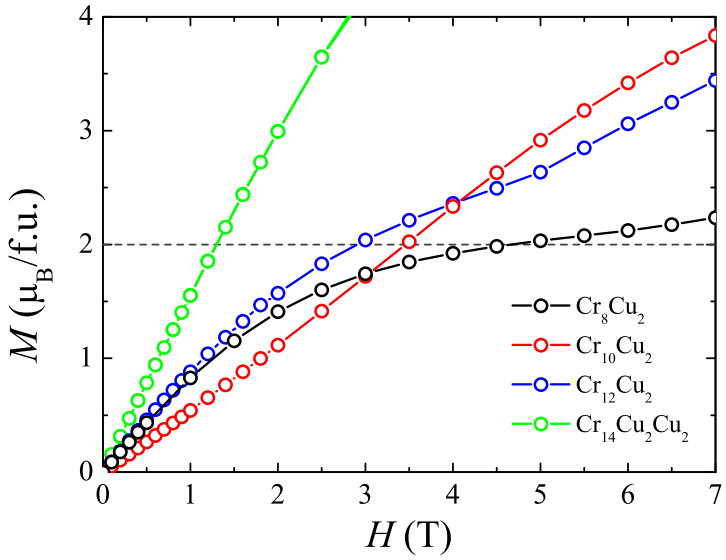

Figure 3.3: Magnetization measured at $T = 2.2$ K for Cr_8Cu_2 (black) [135], $Cr_{10}Cu_2$ (red), $Cr_{12}Cu_2$ (blue) and $Cr_{14}Cu_2Cu_2$ (green). The lines are guidelines for the eyes.

$Cr_{14}Cu_2Cu_2$ is ~ 2.30 emu K mol^{-1} at 2.2 K, but it does not saturate, indicating that at this temperature the low-lying excited states are already populated.

These results are supported by the dc magnetization measurements, plotted in Fig. 3.3 for all the derivatives at $T = 2.2$ K. In the case of Cr_8Cu_2 [135] indeed, $M(H)$ tends to saturate at the value of 2 μ_B (dashed line) pointing to $S_0 = 1$ state, despite at the highest fields the curve is still growing and 2 μ_B is surmounted. This indicates that for fields above ~ 6 T the gap between excited and ground states is reduced and comparable to the experimental temperature, consequently excited states are contributing to the magnetization. This behavior is more accentuated in $Cr_{12}Cu_2$ where a clear change of $M(H)$ is visible with a flex at about 5 T. We can deduce that in this case the excited states are closer to the ground one than in Cr_8Cu_2. For $Cr_{10}Cu_2$ and $Cr_{14}Cu_2Cu_2$, finally, magnetization curves continuously increase with field, confirming the susceptibility result that low-lying excited levels are already populated at 2.2 K.

The temperature dependence of the specific heat, $C(T)$, for different applied magnetic fields between 0 and 7 T is shown in Fig. 3.4 for the various compounds of Cr_xCu_2 family. The curves are normalized to the gas constant

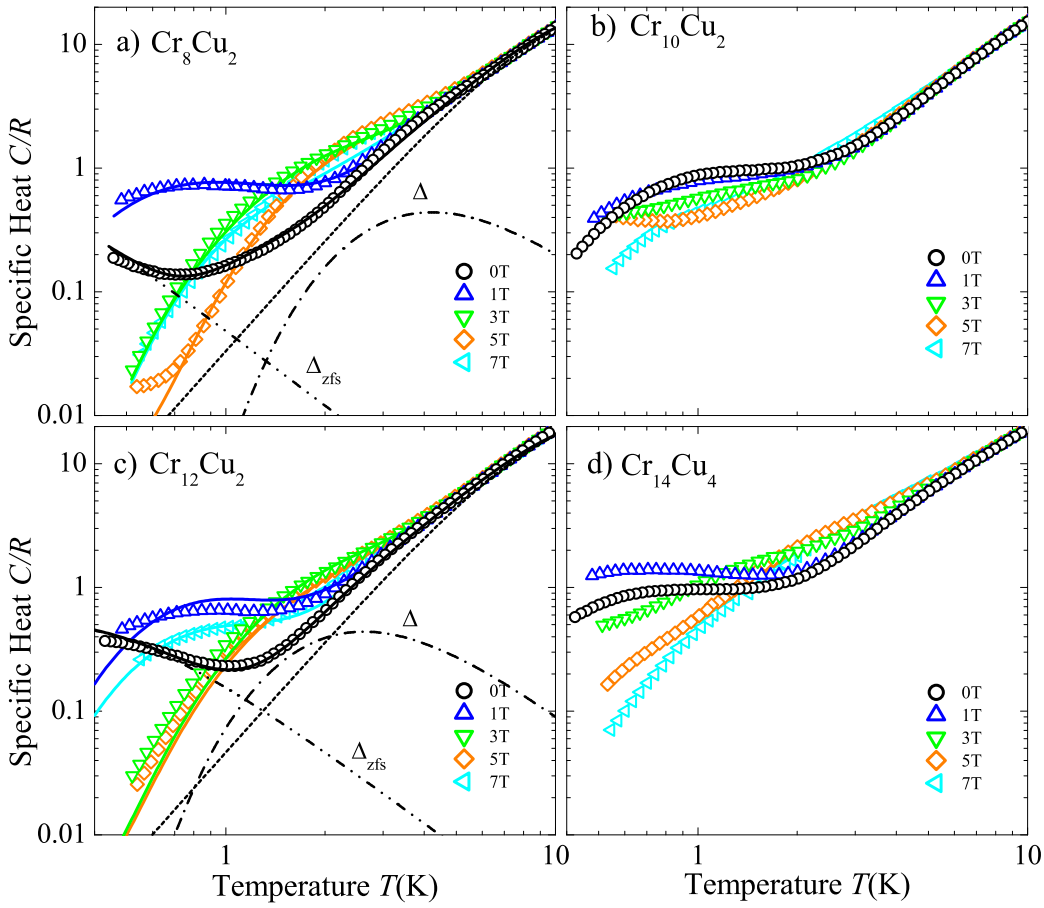

Figure 3.4: Specific heat $C(H,T)$-vs-T measured for a) Cr_8Cu_2, b) $Cr_{10}Cu_2$, c) $Cr_{12}Cu_2$ and d) $Cr_{14}Cu_4$ powder sample at different fixed applied field H. For Cr_8Cu_2 and $Cr_{12}Cu_2$ results of calculations (solid lines), explained in the text, and magnetic and lattice partial contribution to the specific heat with zero applied field (dotted and dashed dotted lines) are also reported.

$R = 8.314$ J/mol K. As common characteristic, data obtained at different magnetic fields overlap almost to each other at temperature $\lesssim 5$ K. This is due to similar lattice contribution that overwhelms the magnetic term. Conversely, for lower temperature the features of magnetic specific heat become visible, enlightening the differences between the systems. As previously observed in susceptibility and magnetization measurements, also in the specific heat a defined separation between the behavior of Cr_8Cu_2 and $Cr_{12}Cu_2$ (having even number of Cr ions in each chain) from one side, and $Cr_{10}Cu_2$ and $Cr_{14}Cu_2Cu_2$ (with odd number of Cr centers) from the other, is evident. For the former compounds the specific heat at $H = 0$ shows two Schottky anomalies that can be attributed to the zero-field splitting of the ground state multiplet (energy gap Δ_{zfs} <1 K) and to the energy gap between the ground and the exited states ($\Delta \simeq$10 K). Conversely for $Cr_{10}Cu_2$ and $Cr_{14}Cu_2Cu_2$ these two Schottky anomalies are peaked at higher temperatures and are due to the contribution of excited states, thus to be analyzed knowing the eigenstates of the Hamiltonian. The latter is quite hard to diagonalize, cause the large number of magnetic centers (a theoretical study of $Cr_{10}Cu_2$ is reported in Ref. [137], where quantum Monte Carlo method is used to bypass this problem).

In the next section I focus on Cr_8Cu_2 and $Cr_{12}Cu_2$ to obtain more quantitative information comparing the specific heat data with theoretical expressions for lattice and magnetic contributions.

3.2.1 Theoretical Models

As first step, for both Cr_8Cu_2 and $Cr_{12}Cu_2$ rings I considered an effective model taking into account only the three expected lowest-lying multiplets $S = 1$, $S = 0$ and $S = 2$ and by using as expression for the energy levels:

$$\epsilon_j(H) = \epsilon(S_i) + D\left(M_j^2 - \frac{1}{3}S_i(S_i+1)\right) + g\mu_B M_j H \tag{3.1}$$

where at the eigenvalues $\epsilon(S_i)$ of the Heisenberg exchange hamiltonian, in order, the effect of the axial crystal field anisotropy and the Zeeman effect due to external magnetic field **H** are summed. Furthermore, in order to better reproduce the behavior of the zero-field data, for the ground state also the rhombic splitting, due to the slightly squeezed shape of the wheels (see Fig. 3.1), was taken into account.

Table 3.1: Fit parameters.

	r	Θ_D(K)	δ(K^{-1})	D/k_B(K)	E/k_B(K)
Cr_8Cu_2	376	138	0.5	-0.36±0.07	0.17±0.03
$Cr_{12}Cu_2$	504	136	0.55	-0.9±0.2	0.20±0.07

The analytical expressions for the exact eigenvalues of the multiplet $S_0 = 1$, in function of D and E, axial and rhombic anisotropy constants, reported by Boča [138], then result: $(\epsilon_0, \epsilon_1, \epsilon_2) = (+D/3+(E^2+(g\mu_B H)^2)^{1/2}, -2D/3, +D/3-(E^2 + (g\mu_B H)^2)^{1/2})$ for $M(S_0) = -1, 0, +1$ respectively. The fitting curves are displayed by the solid lines in Figs. 3.4(a) and (c). The best fit is obtained by using the set of parameters reported in Table 3.1, in both cases $g = 2$ was used. The lattice parameters Θ_D and δ are obtained by least-square fitting of the specific heat in the temperature range $5 - 15$ K, while r is the number of atoms per unit cell, known by the structure formula. The other parameters are obtained in order to have a good accordance between theoretical curves and experimental data for all magnetic fields. The patterns of the resulting low-lying energy levels are reported in Fig. 3.5. As expected from magnetization results, the excite multiplet $S = 2$ for $Cr_{12}Cu_2$ is few K closer to the ground state $S_0 = 1$ than for Cr_8Cu_2 molecule.

For Cr_8Cu_2 system the exact diagonalization of the spin-Hamiltonian has been performed by Dr. A. Bianchi in Parma. To obtain the $S_0 = 1$ ground state, corresponding to a ferromagnetic alignment of the two Cu ions, as illustrated in Fig.3.6(a), it is necessary to assume three different values of exchange constants: one for the antiferromagnetic interaction between adjacent Cr, J_{Cr-Cr}, one for antiferromagnetic coupling between the Cu and one adjacent Cr, $J^{(1)}_{Cr-Cu}$, and finally one for ferromagnetic interaction between Cu and the other adjacent Cr, $J^{(2)}_{Cr-Cu}$. These parameters were already used in Refs. [135,137] for the description of Cr_8Cu_2 and $Cr_{10}Cu_2$, respectively, but the values were found by fitting only the susceptibility and magnetization, thus having poor information on the anisotropy that can be refined by using also heat capacity measurements. The system can

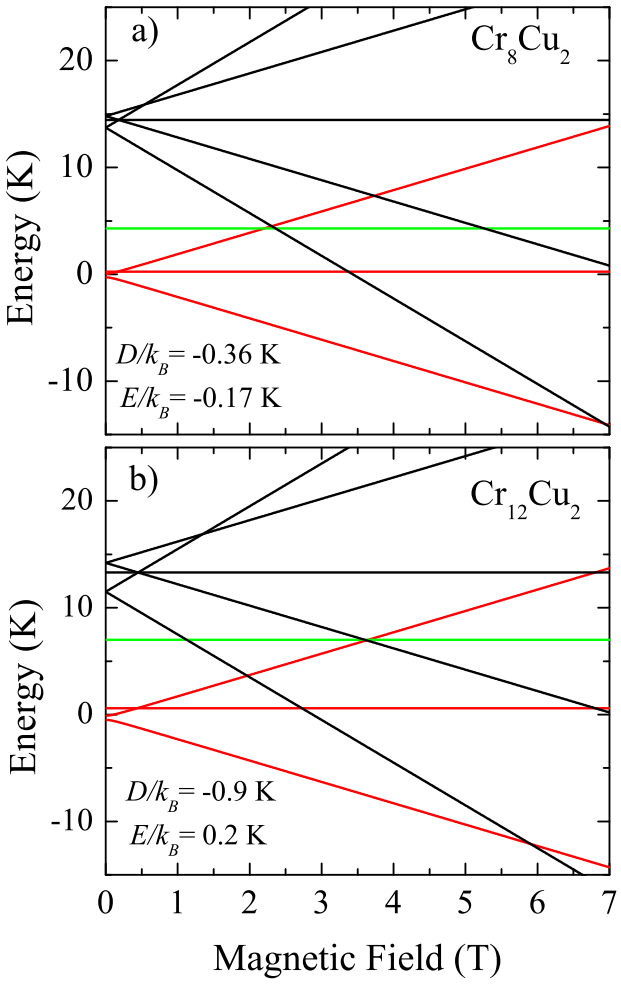

Figure 3.5: Patterns of the low-lying energy levels calculated with the parameters reported in Table 3.1 for (a) Cr_8Cu_2 and (b) $Cr_{12}Cu_2$.

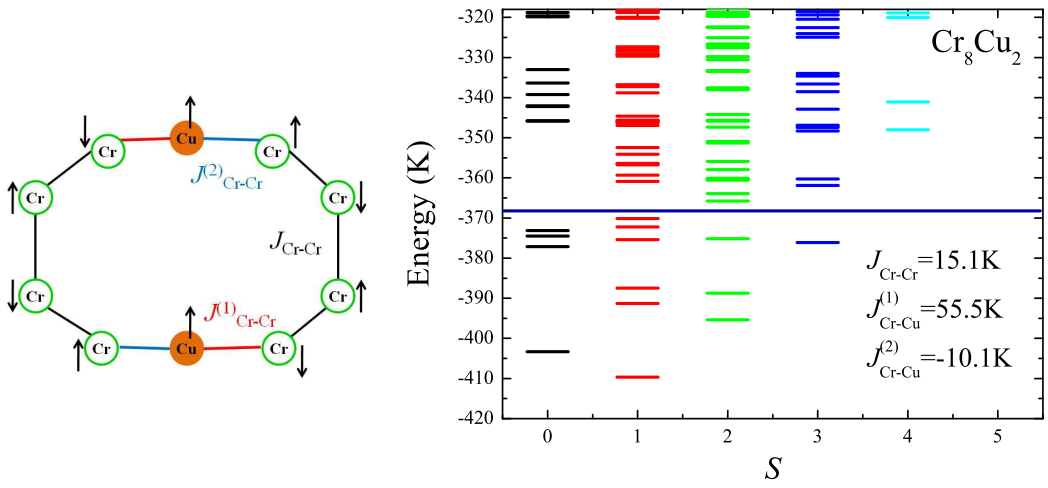

(a) (b)

Figure 3.6: a) Sketch of the interaction between the magnetic centers and spin arrangement in Cr_8Cu_2 needed to explain the $S_0 = 1$ ground state. b) Energy spectrum of Cr_8Cu_2 versus total spin quantum number S obtained through the diagonalization of only the Heisenberg spin-Hamiltonian and taking into account three different exchange constants, whose values are reported (Dr. A. Bianchi). The blue line delimited the states considered for the theoretical calculations.

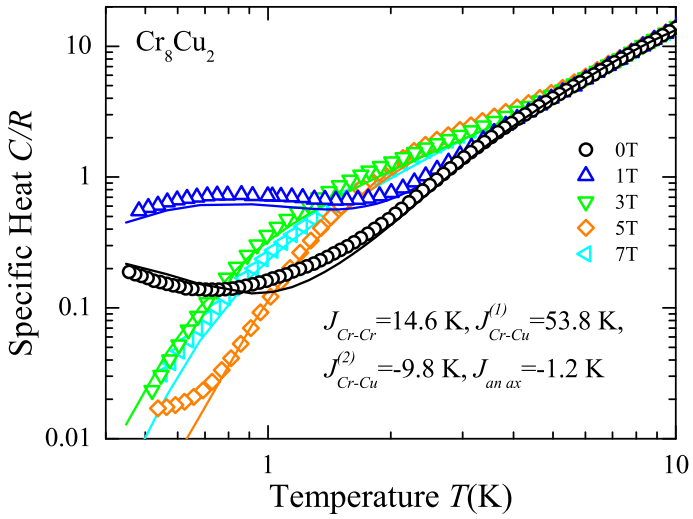

Figure 3.7: Specific heat of Cr_8Cu_2 fitted (solid lines) with the calculation obtained by diagonalization of spin Hamiltonian described in the text. The values of exchange constants used are reported.

be described by the spin Hamiltonian:

$$\begin{aligned} \mathcal{H} &= \mathcal{H}_{ex} + \mathcal{H}_{an} + \mathcal{H}_{Zeeman} \\ &= \sum_{i=1}^{10} J_i \mathbf{s}_i \cdot \mathbf{s}_{i+1} \\ &+ \sum_{i,j} J_{an-ax} \left(2\mathbf{S}_{z,i} \cdot \mathbf{S}_{z,j} - \mathbf{S}_{x,i} \cdot \mathbf{S}_{x,j} - \mathbf{S}_{y,i} \cdot \mathbf{S}_{y,j}\right) \\ &+ \mu_B g \sum_{i=1}^{10} \mathbf{H} \cdot \mathbf{s}_i \end{aligned} \tag{3.2}$$

where the first term on the right side is the isotropic Heisenberg coupling, the second accounts for the anisotropic exchange interaction between Cr and Cu ions, and the last is the Zeeman interaction with external magnetic field. As first step of analysis, only the Heisenberg part of the Hamiltonian was diagonalized by using as exchange values those found in Ref. [135] for Cr_8Cu_2: $J_{\mathrm{Cr-Cr}}$=15.1 K, $J^{(1)}_{\mathrm{Cr-Cu}} = 55.5$ K and $J^{(2)}_{\mathrm{Cr-Cu}} = -10.1$ K. The result is illustrated in the energy spectrum versus total quantum spin S in Fig. 3.6(b), where the rotational Landé band is clearly visible. Successively, also the anisotropic interaction and Zeeman

terms were included in the diagonalization. Since the temperature is very low, only the multiplets delimited by the blue line in Fig. 3.6(b) were considered in the calculation. Fitting the heat capacity, see solid lines in Fig. 3.7, the best parameter values for the isotropic exchange constants and the anisotropic one were found, giving: $J_{\mathrm{Cr-Cr}}$=14.6 K, $J^{(1)}_{\mathrm{Cr-Cu}} = 53.8$ K, $J^{(2)}_{\mathrm{Cr-Cu}} = -9.8$ K and $J_{\mathrm{an.ax}}$=-1.2 K. With these values also the susceptibility was successfully reproduced (solid line in Fig. 3.2).

Discussion

In this chapter the magnetic properties of Cr_xCu_2 were investigated by susceptibility, magnetization and heat capacity measurements. From all the experiments emerged a clear-cut separation between Cr_8Cu_2 and $Cr_{12}Cu_2$, with $S_0 = 1$ ground state, from one side and $Cr_{10}Cu_2$ ($S_0 = 0$)and $Cr_{14}Cu_2Cu_2$ (S_0 still not clear) from the other. The latter have antiferromagnetic Cr chains with an even number of chromium centers, meaning that only the copper ions ($s = 1/2$) contribute to the total spin, therefore, from the value of the ground state, we can suppose that their spins are arranged in parallel. Conversely, in the cases of $Cr_{10}Cu_2$ and $Cr_{14}Cu_2Cu_2$, that have an odd number of chromium ions in the chains, also the chromium spins contribute to the total spin S of the molecules. In conclusion, the magnetic characterization of the Cr_xCu_2 systems has evidenced the dependence of the ground state by the topology of the chromium chains.

For the 'even-chromium-chain' molecules the axial and rhombic anisotropy were estimated by means of an effective model through the analysis of the zero-field-splitting in the specific heat. Moreover, complementary information on the three exchange constants J between the metal centers was obtained by means of spin-Hamiltonian diagonalization approach for the smaller Cr_8Cu_2.

The chemical bridging between the magnetic center is very similar for all the derivatives. This allows to extend the anisotropy and exchange constants parameters found for the simplest system Cr_8Cu_2 to the others that are more complex to characterize, since the huge increasing of the dimension of matrix to diagonalize. In particular this can be very helpful in the case of the biggest derivative, $Cr_{14}Cu_2Cu_2$. This is potentially the most interesting among the Cr_xCu_2 family for further investigation for quantum communication exploitation, thank to the presence of the two extra-copper ions, external to the rings and thus more weakly coupled with respect to the chains. More specifically, further experiments by means of chemical selectivity technique, like X-ray spectroscopy, can be thought to probe locally the magnetization at the Cu edges and to investigate how the state of one Cu changes when perturbing the other, communicating via the chromium chains. Of course, the realization of such kind of experiment can not be immediate at the state of art. Demanding capabilities are necessary like the ability to initialize the system, to modify the state of the first spin in a timescale that

is short as compared to the coupling between first spin and the rest of the chain (not to perturb the rest of the system) and finally to read out the information on the second spin, locally, but also time resolved to probe the coherent dynamics. However, the characterization here reported identifies $Cr_{14}Cu_2Cu_2$ as suitable system, moreover it provides the limits requested by a possible experiment. As example, in this case, since at 2 K temperature excited states are already populated, for the initialization temperatures lower than 2 K are needed. For what concerns the operation time to excite the Cu ion, an upper limit is given by the biggest J exchange constant between the spins of the chain: 9.8 K corresponding to ~ 10 ps, if assumed equal to that of Cr_8Cu_2.

Chapter 4

Open spin rings: Cr_6InNi and Cr_7InNi

In this Chapter, the characterization of two heterometallic molecular derivatives, namely, Cr_6InNi and Cr_7InNi, which are odd- and even-membered spin cyclic systems magnetically broken by In^{3+} ($s = 0$) ion, is reported. Analysis of low-temperature specific heat, susceptibility, and magnetization allows to determine the microscopic parameters of the spin Hamiltonian and the pattern of the spin excitations. It turns out that exchange coupling and anisotropy constants in Cr_6InNi and Cr_7InNi are quite close to those in the parent Cr_7Ni-piv ring.

Based on these grounds, x-ray magnetic circular dichroism (XMCD) measurements were performed to separately investigate local symmetries, electronic configuration, orbital, and spin magnetic moments of the magnetic ions [139–142]. As result, it is shown how the spin of Ni^{2+} can be used as a marker to probe the local magnetization of spin segments by directly comparing the sign and the intensity of the dichroic signal measured in the three derivatives. This will allow, for instance, to test effects at the edges and eventually to read out information in specific positions of the spin segment.

The chapter is organized as follows: in 4.1, the chemical synthesis and structural characterization of the derivatives are reported, afterwards 4.2 is devoted to the analysis of susceptibility, magnetization and specific heat measurements; while in Appendix A.1 spectroscopic data and their analysis are reported. This work is interdisciplinary and realized by the collaboration of chemists and exper-

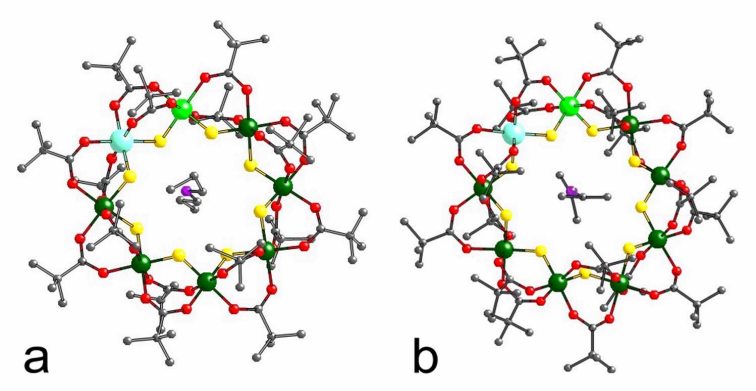

Figure 4.1: X-ray diffraction structures of a) Cr_6InNi and b) Cr_7InNi. Colors: Cr, green; Ni, light blue; In, gray, F, yellow; O, red; C, black; N, blue. Hydrogens are omitted for simplicity.

imental and theoretical physicists. In this framework, I dealt in the experimental characterization by low temperature specific heat together with Dr. A. Ghirri, while the susceptibility and magnetization were performed by Dr. Floriana Tuna at the *Lewis Magnetism Laboratory* in Manchester. The samples were synthesized by Dr. Gregory Timco within the group of Prof. Richard P. Winpenny at *School of Chemistry* in Manchester. The X-ray absorption spectroscopy experiments were carried out by Dr. Valdis Corradini, Dr. Roberto Biagi and Prof. Umberto del Pennino at the ID8 beamline of the European Synchrotron Radiation Facility (ESRF) in Grenoble. Finally, the theoretical calculations were done by Dr. Stefano Carretta, Dr. Paolo Santini and Prof. Giuseppe Amoretti at University of Parma.

4.1 Synthesis and structural characterization

The two compounds presented in this chapter and named in short Cr_6InNi and Cr_7InNi have, respectively, the chemical formulas:

$$[H_2NR_2][Cr_6InNiF_8(O_2CCMe_3)_{16}],$$

with R=C_3H_7, and

$$[H_2NR_2][Cr_7InNiF_9(O_2CCMe_3)_{18}],$$

with R=$is$$C_3H_7$. The samples were prepared by Dr. Grigore Timco and Prof. Richard Winpenny at *School of Chemistry*, University of Manchester. Full details of the synthesis are reported in Refs. [98,143], while the crystallographic data for the structures -excluding structure factors- have been deposited with the Cambridge Crystallographic Data Centre as supplementary Publication Nos. CCDC -705752 and -705753.

Crystallographic structures of Cr_6InNi and Cr_7InNi are shown in Fig. 4.1. Metals are placed at the vertex sites of regular octagon and nonagon, having a side length of 3.4 Å. Their chemical bridging occurs by means of one fluoride bridge and two 1,3-bridging pivalates either for Cr_6InNi or for Cr_7InNi. The local symmetry of each chromium, indium, or nickel is represented by an octahedron with six apical atoms: four O and two F atoms, equidistant from the metal ion (1.97±0.03 Å), which lies in a slightly distorted octahedral (Oh) environment. Due to the incomplete equivalence between F and O, the symmetry of the coordination around each ion is formally C_2. However, the very similar bond lengths and angles around the magnetic ion leads to an almost perfect equivalence between F and O, which allows the assumption of a nearly pure Oh symmetry even for what concerns the charge and spin densities as evidenced by density-functional theory calculations [144]. The similarity in the metal-F-metal and O-C-O angles, which, respectively, range between 124°-126° and 120°-123° for Cr_6InNi and between 124°-130° and 118°-123° for Cr_7InNi, indicates comparable nearest-neighbor exchange coupling in both clusters. Due to the synthetic procedure that has been followed which introduces Ni^{2+} and In^{3+} in the same starting compound, their positions will be one after the other in the final cyclic structure and this implies that $s(Ni^{2+})=1$ is at the edge of the spin segment. This is consistent with crystallographic refinements.

4.2 Thermodynamic properties

To magnetically characterize the two derivatives, in Figs. 4.2 and 4.3 the *ac*-susceptibility and magnetization are reported. The experiments were carried out at the Lewis Magnetism Laboratory in Manchester by Dr. F. Tuna by means of a superconducting quantum interference device magnetometer (Quantum Design

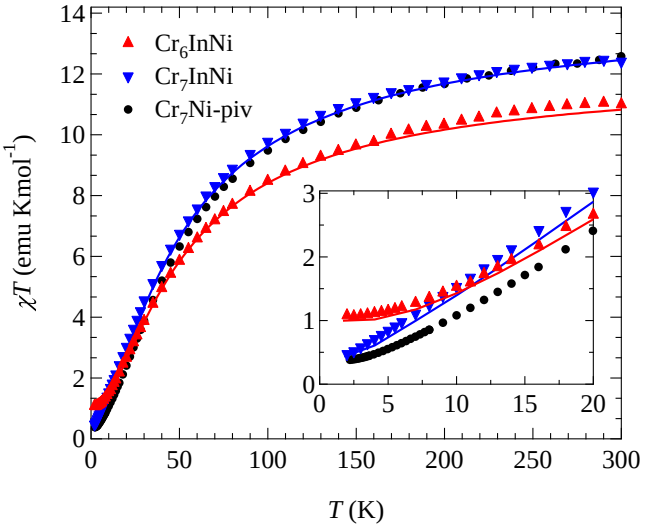

Figure 4.2: Temperature dependence of the susceptibility χT for: Cr_6InNi (red triangles), Cr_7InNi (blue triangle) and Cr_7Ni-piv (black circles) polycrystalline samples. Solid lines are results of calculation explained in the text (by Dr. Stefano Carretta).

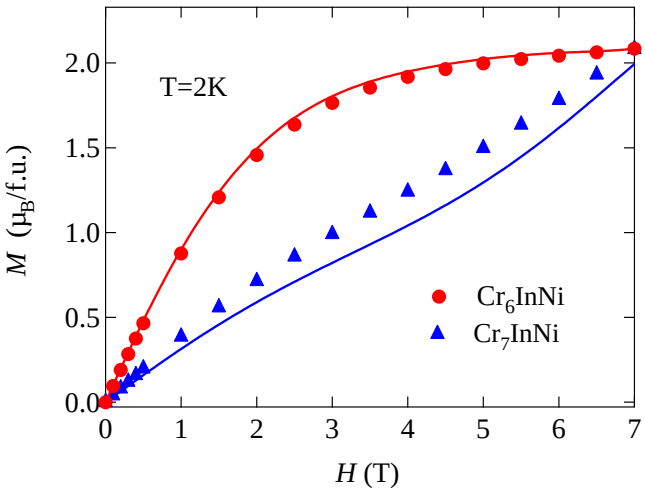

Figure 4.3: Magnetization curves at $T = 2$ K for Cr_6InNi (red circles) and Cr_7InNi (blue triangles). Solid lines represent the theoretical simulation (by Dr. Stefano Carretta).

MPMS-7T). Susceptibility data were collected by applying a fixed field of 0.1 T. In Fig. 4.2 the temperature (T) dependence of the molar susceptibility χ is plotted as χT vs T for both the Cr_6InNi and Cr_7InNi compounds. For comparison the χT vs T curve of Cr_7Ni-piv taken from Ref. [47] is also plotted in this figure. In the temperature range of $20 - 300$ K the three derivatives display a similar behavior. At room temperature the χT values are close to those expected for uncoupled paramagnetic ions: $\chi T(300\text{ K}) = 12.5$ emu K mol^{-1} for Cr_7Ni-piv and Cr_7InNi and $\chi T(300\text{ K}) = 11.4$ emu K mol^{-1} for Cr_6InNi. Below 10 K the χT vs T curves of Cr_6InNi and Cr_7InNi have a different behavior (see inset of Fig. 4.2): for the former χT saturates at 1.1 emu K mol^{-1}, suggesting a ground state with total spin $S = 1$. Conversely, for the latter, χT progressively decreases getting close to the value attained for Cr_7Ni-piv at 2 K. This suggests ground-state spin $S = 1/2$ with excited states closely spaced in energy for Cr_7InNi.

Figure 4.3 shows the magnetization (M) as a function of the applied magnetic field (H) for Cr_6InNi and Cr_7InNi. At 2 K, a different behavior for the two derivatives is well visible: for Cr_6InNi, the $M(H)$ curve is close to a simple Brillouin function saturating at about 2.1 μ_B, confirming the $S = 1$ ground state indicated by the susceptibility, whereas for Cr_7InNi the $M(H)$ curve shows a continuous increase with the field H.

In Fig. 4.4 the temperature dependence of specific heat $C(T, H)$ taken at different values of fixed magnetic field H is plotted for Cr_6InNi [panel (a)] and for Cr_7InNi [panel (b)]. For both the derivatives, at high temperature the lattice contribution dominates, while for $T <$7 K, features of the magnetic contribution become clearly visible. For Cr_6InNi, the latter indeed displays two distinct Schottky anomalies in zero field: a first one in the few K range is related to the energy gap $\Delta_{ex} \simeq 15$ K between the ground and the lowest-lying excited multiplets and a second one, peaked below 1 K, evidences the zero-field splitting of the ground state ($\Delta_{zfs} \simeq 1$ K). For Cr_7InNi, the Schottky anomaly due to the intermultiplet separation (Δ_{ex}) is found with a broad maximum at low temperatures ($\simeq 3$ K), thus indicating that the energy spacing between the lowest multiplets is smaller than in Cr_6InNi.

To have more quantitative information the measured data are compared with the simulated ones, obtained by using a spin-Hamiltonian model. The specific

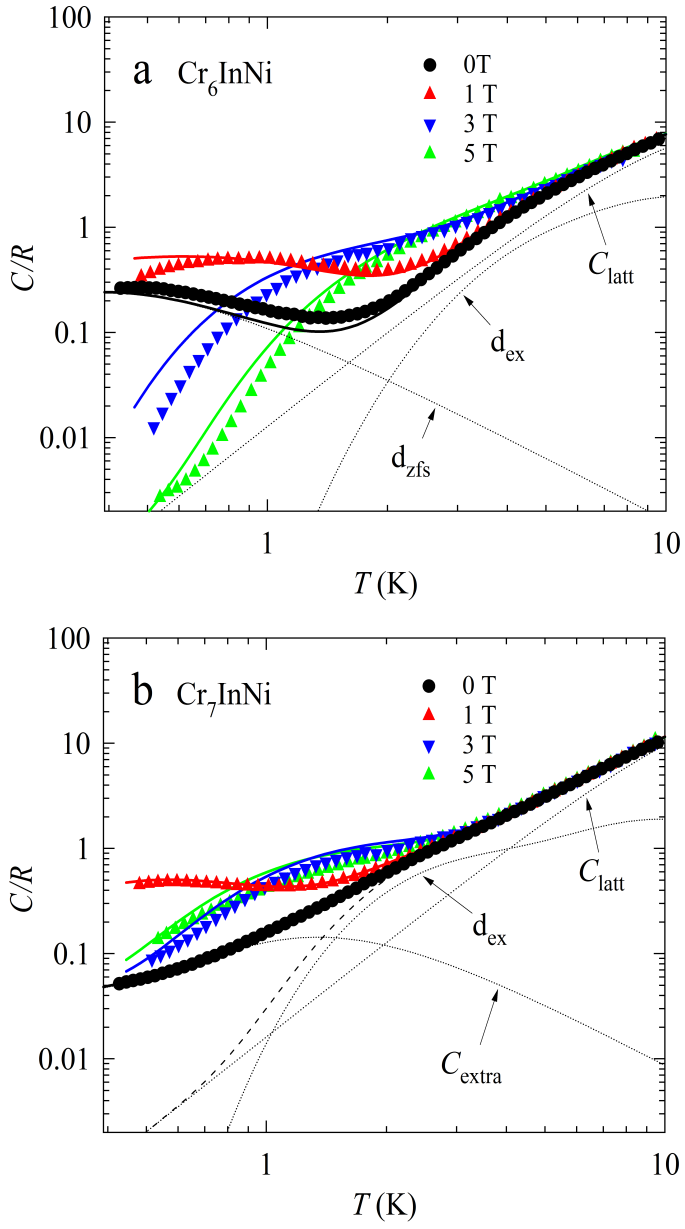

Figure 4.4: Specific Heat $C(H,T)$ measured in Cr_6InNi (upper panel), and Cr_7InNi (lower panel) microcrystalline thin pellets. The curves are measured at different magnetic fields and normalized to the gas constant R. Solid lines are calculated using Eq. (4.1), while dot and dashed lines represent the zero field splitting, the lattice and the extra contributions described in the text.

spin Hamiltonian that has already reproduced the magnetic behavior of parent compounds [49] reads

$$\mathcal{H} = \sum_{i=1}^{N-1} \mathbf{J}_i \mathbf{s}_i \cdot \mathbf{s}_{i+1} + \sum_{i=1}^{8} d_i \left[s_{z,i}^2 - s_i(s_i+1)/3 \right] + \mu_B \sum_{i=1}^{8} \mathbf{H} \cdot \mathbf{g}_i \cdot \mathbf{s}_i, \qquad (4.1)$$

with N as the number of magnetic ions. Here, the first term accounts for the dominant exchange interaction between nearest-neighboring ions ($\mathcal{H}_{ex}$); the second and third terms describe the interaction with the local (axial) crystal field ($\mathcal{H}_{cf}$) and the Zeeman coupling ($\mathcal{H}_Z$) to applied magnetic field, respectively. The eigenvalues are obtained by directly diagonalizing the dominant part of the Hamiltonian, namely, $\mathcal{H}_0 \equiv \mathcal{H}_{ex} + \mu_B g_{Cr} \mathbf{H} \cdot \mathbf{S}$. The effect of the additional terms ($\mathcal{H}_1$) are included within first-order perturbation theory, being $\mathcal{H}_1 = \mathcal{H}_{cf} + (g_{Ni} - g_{Cr}) \mathbf{H} \cdot \mathbf{s}_N$. Since the two molecular systems considered here are closely related to the unbroken Cr_7Ni-piv rings, for the physical parameters that enter in the spin Hamiltonian the same values were adopted: $J_{Cr-Cr}/k_B = 17.0$ K, $J_{Cr-Ni}/k_B = 19.6$ K, $d_{Cr}/k_B = -0.36$ K, $dNi/k_B = -7$ K, $g_{Cr} = 1.98$, and $g_{Ni} = 2.2$ [50]. The presence of a nonmagnetic ion In^{3+}, however, modifies from the magnetic point of view the topology of the molecule, making it an open, rather than a cyclic structure.

The theoretical simulations of specific heat, susceptibility and magnetization (solid lines in Fig. 4.4, 4.2 and 4.3) are respectively obtained by substituting the eigenvalues of Eq. (4.1) in the expressions: (1.17), (1.23) and (1.18). The calculations were averaged on the relative orientation of magnetic field and easy axis direction in order to reproduce the random orientation of the molecules in the powder sample. For the specific-heat plots (Fig. 4.4), C_{latt} has been estimated by using Eq. (1.14) together with $r = 295$, $\Theta_D = 175$ K, and $\delta = 0.55$ K^{-1} for Cr_6InNi and $r = 329$, $\Theta_D = 168$ K, and $\delta = 0.32$ K^{-1} for Cr_7InNi. The agreement with the experimental data is remarkably good even by using for both Cr_6InNi and Cr_7InNi the same values of the exchange and the anisotropy constants reported in Ref. [50] for Cr_7Ni-piv (see above). This clearly demonstrates the capability of selectively introducing local changes in the chemical composition and topology of a given molecule, without altering the remaining interactions within the molecule. The resulting patterns of the lowest-lying energy levels are plotted in Fig. 4.5 as a function of the magnetic field. For Cr_6InNi the ground state ($S = 1$) is separated

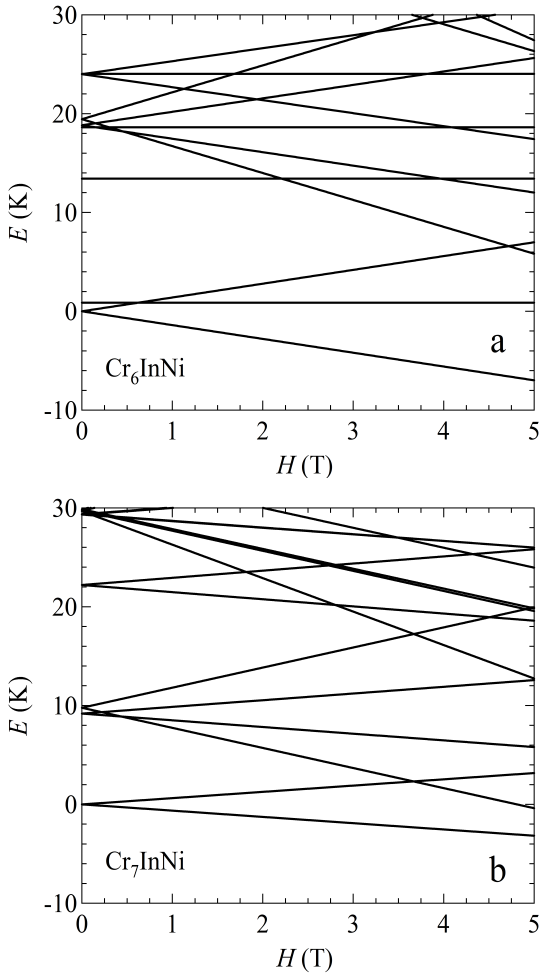

Figure 4.5: Low-lying energy levels $E(H)$ of Cr_6InNi and Cr_7InNi calculated by diagonalization of the spin-Hamiltonian as reported in the text (by Dr. Stefano Carretta). In the calculations the magnetic field is perpendicular to the plane of the ring.

by an energy gap of 13.4 K from the first excited state ($S = 0$). The overlying multiplets are found with barycenter at 19.0 K ($S = 2$) and 24.0 K ($S = 1$). For Cr_7InNi, the energy gaps between the ground state ($S = 1/2$) and the barycenters of the first excited ($S = 3/2$) and second-excited ($S = 1/2$) multiplets are at 9.5 and 22.2 K, respectively. The specific-heat curves at $H = 0$ and 1 T of Cr_7InNi are reproduced by adding an extra background C_{extra} at temperatures below few K. With reference to panel (b) of Fig. 4.4, the measured C/R (markers) is found close to 0.1 at 1 K while the model calculations (dashes) display a progressive decrease in $C(H = 0)$ vs T for $T < 2$ K, as expected for the ground doublet. We note, however, that the maximum of C_{extra} is only $C/R \approx 0.1$ at 1 K, which is almost one order of magnitude smaller than what expected for any Schottky anomaly involving the whole sample. Therefore it is reasonable to conclude that this background anomaly of the C vs T curves is due to a small fraction (few percent) of impurity (damaged rings, isolated monomers, etc.) in this sample.

Conclusions

I carried out calorimetry measurements on two new molecular derivatives, namely, Cr_6InNi and Cr_7InNi, which are good examples of even- and odd-membered antiferromagnetic spin segments with a Ni^{2+} spin at one edge. Specific heat, susceptibility and magnetization measurements allow us to determine the microscopic parameters of the spin Hamiltonian and the pattern of the spin excitations of the molecules. It turns out that the ground state are $S = 1$ for Cr_6InNi and $S = 1/2$ for Cr_7InNi. Moreover, the exchange coupling and the anisotropy constants in both the derivatives are quite close to those in the well known Cr_7Ni-piv molecule. These results are at the base of further investigation on the local magnetization, through XMCD spectroscopy, of the Cr^{3+} and Ni^{2+} metal ions compared with Cr_7Ni-piv molecular rings. Spectroscopic results, reported in Appendix A.1, show that the dichroic signal taken at the Ni $L_{2,3}$ edges is particularly sensitive to the topology or nuclearity of the cyclic system, evidencing that, in magnetically broken rings, the spin of nickel tends to be aligned along the magnetic-field direction. Simulations performed within a spin-Hamiltonian model and using the same microscopic parameters estimated for the Cr_7Ni-piv closed ring are in good agreement with all the above measurements. This clearly demonstrates the capability of introducing selective changes in the spin-chain topology or nuclearity without affecting the remaining interactions.

Chapter 5

Chromium-based triangles

In this chapter the homometallic Chromium-based triangle Cr_3 is firstly presented in 5.1. In the successive section 5.2, the case of Cr_2Cu, heterometallic and thus magnetically isosceles triangle, is investigated. My contribution to this work concerns the experimental characterization, performed together with Dr. Andrea Candini, by low temperature susceptibility, magnetization and specific heat, as well as collection and discussion of all results. The samples were synthesized by Dr. Gregory Timco within the group of Prof. Richard P. Winpenny at *School of Chemistry* in Manchester. The X-ray absorption spectroscopy experiments, reported in Appendix for Cr_2Cu molecules, were performed at the ID8 beamline of the European Synchrotron Radiation Facility (ESRF) in Grenoble (France) by Dr. Valdis Corradini, Dr. Roberto Biagi and Prof. Umberto del Pennino. Finally, the theoretical calculations were done by Dr. Stefano Carretta, Dr. Elena Garlatti, Dr. Paolo Santini and Prof. Giuseppe Amoretti at University of Parma.

5.1 Cr_3

The first trimer I present is the homometallic:

$$[Cr_3O(O_2CC_6H_5)_6(C_5H_{10}NH)_3]ClO_4,$$

Cr_3 in short; whose chemical synthesis is reported in Ref. [150]. In Fig. 5.1(a) the crystallographic structure of Cr_3 is shown. The metallic ions are placed at the vertexes of an equilateral triangle with side length 3.314 Å, as shown in Fig. 5.1(b).

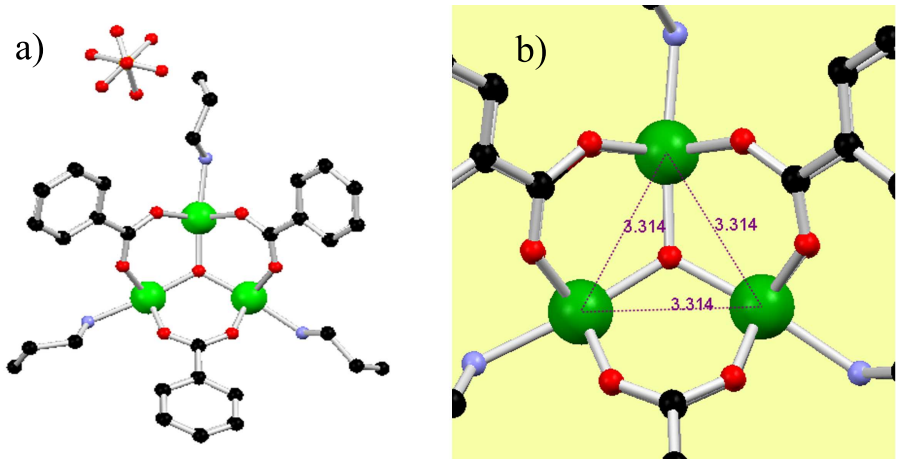

Figure 5.1: a), b) X-ray diffraction structure of Cr_3. Colors: Cr, green; N, light blue; C, black; O, red. Hydrogens are omitted for simplicity. In b), in order to enlighten the geometry of Cr_3, the structure a) is magnified around the magnetic ions and measurements of Cr-Cr distances in Å are reported.

The structure of the whole molecule is highly symmetric: there is a central Oxygen, a pyridine group attached to each Cr and for each couple of adjacent metal centers two carboxylates provide both the chemical bridging and the antiferromagnetic (AF) superexchange coupling. Thus the local symmetry of each Cr is represented by a slightly distorted octahedron with five Oxygens and one Nitrogen. The four in plane O are equidistant from the metal ion (1.97 ± 0.04 Å) while along the out of plane direction the octahedron results asymmetrically stretched with the distance between the Cr and the O equal to 1.91 ± 0.04 Å; finally the Cr-N distance is 2.16 ± 0.04 Å.

5.1.1 Magnetic characterization

Figure 5.2 shows the ac-susceptibility of the Cr_3 compound plotted as the product χT vs T. Below ~ 10 K, it saturates at 0.375 emu K/mol, i.e. the value expected from the Curie's law for a paramagnet with spin $S = 1/2$. Since the saturation happens at a relatively high temperature, we expect that the energy ground state is well separated from the excited levels. This is suggested also by the magnetization M vs H shown in Fig. 5.3, where a simple Brillouin-like curve is

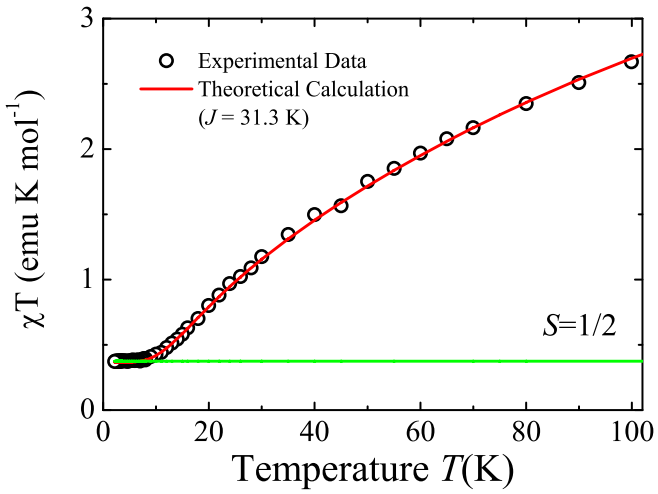

Figure 5.2: (Markers) Temperature dependence of susceptibility χT measured for Cr_3 microcrystalline sample. Solid lines: (red) is the result of calculations assuming $J = 31.3$ K; (green) value expected for a $S = 1/2$ paramagnet following Curie's law. Data were measured with an ac field of 10 Oe and at the frequency of 90 Hz on powders sample.

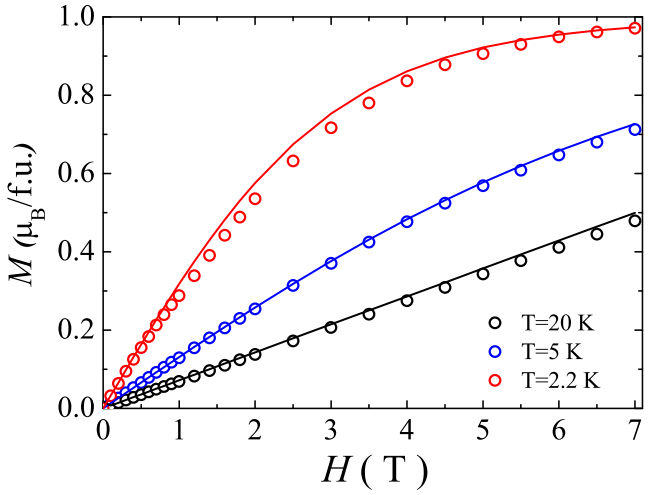

Figure 5.3: (Open circles) dc-magnetization vs magnetic field $M(B,T)$ measured at different temperatures for the Cr_3 system. (Solid lines) theoretical calculations obtained by diagonalizing the microscopic Hamiltonian discussed in the text assuming only one exchange constant, $J = 31.3$ K.

observed: the saturation value at 2 K is 1 μ_B in agreement with the hypothesis that only the $S = 1/2$ level is populated. In order to have a quantitative analysis, the system can be modeled assuming an antiferromagnetic Heisenberg interaction between adjacent magnetic ions of the type $\mathcal{H} = JS_iS_j$ and a Zeeman energy term, present when the external field H is switched on. If J is the same for all the couples (equilateral triangle), the lowest energy level will be a (doubly) degenerate $S = 1/2$ state [26]. Taking into account also the excited multiplets by exact diagonalization of the Hamiltonian and assuming $J = 31.3$ K, both susceptibility and magnetization data are well reproduced (solid lines in Figs. 5.2 and 5.3). However, the low temperature specific heat data in Fig. 5.4 exhibit a pronounced Schottky anomaly at around 0.6 K in zero field curve. Since such peaks are related to gaps between low energy levels, it turns out that the ground state is made of two doublets split by ~ 1 K. An explanation can be found in the magnetically frustrated triangular structure of Cr_3. Due to frustration indeed, we may expect that the equilateral trimer undergoes an isosceles distortion (likely at low temperature) to reach a more stable configuration, where two different interactions are present: one between the ions at the basis (labelled J) and one between the atoms at the basis and the one at the vertex of the triangle (labelled J'). This lifts the degeneracy by an amount equal to $\Delta = J - J'$ [26]. Considering as effective model only the two ground state doublets (see the central inset of Fig. 5.4), the evolution of the Schottky anomaly with the external field in the specific heat is well simulated (solid lines in Fig. 5.4) assuming the second coupling constant $J' = 29.7$ K, and thus giving an energy split $\Delta = 1.6$ K.

Finally, regarding the specific heat data shown in Figure 5.4, it should be said that the discrepancies between the theoretical and the experimental curves in zero field are caused by the broadening of the Schottky peak in the latter. Such feature, that can not be simply ascribed to a wrong estimation of any microscopic parameters, is likely originated by the presence of different types of molecular isomers inside the macroscopic measured samples.

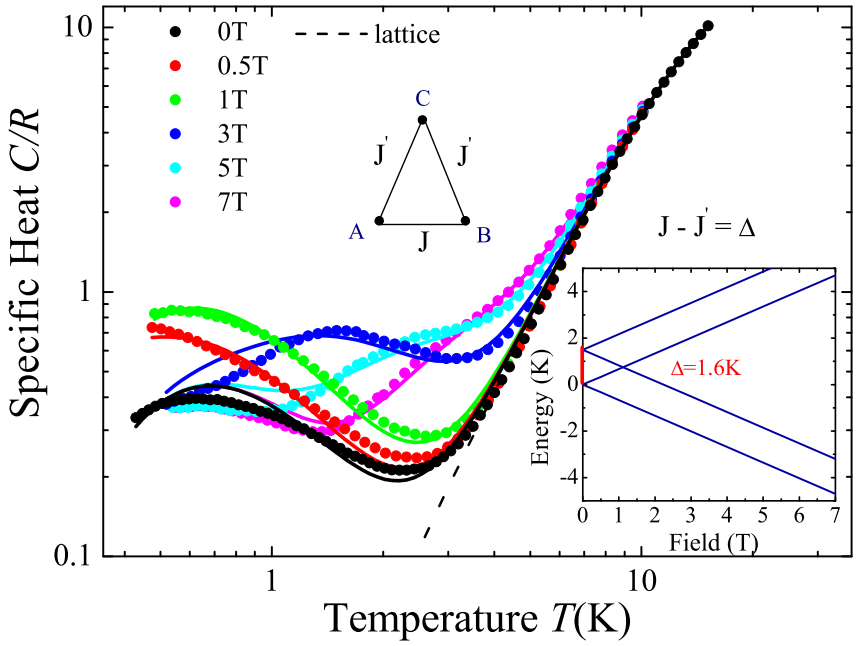

Figure 5.4: Specific heat normalized to gas constant R measured for Cr_3 for several magnetic fields. Solid lines represent result of the calculations explained in the text. (Inset at right bottom) Energy levels of the doubly $S = 1/2$ ground state as a function of magnetic field and calculated assuming two different exchange constants between the vertexes of Cr_3 triangle as schematized in the central inset.

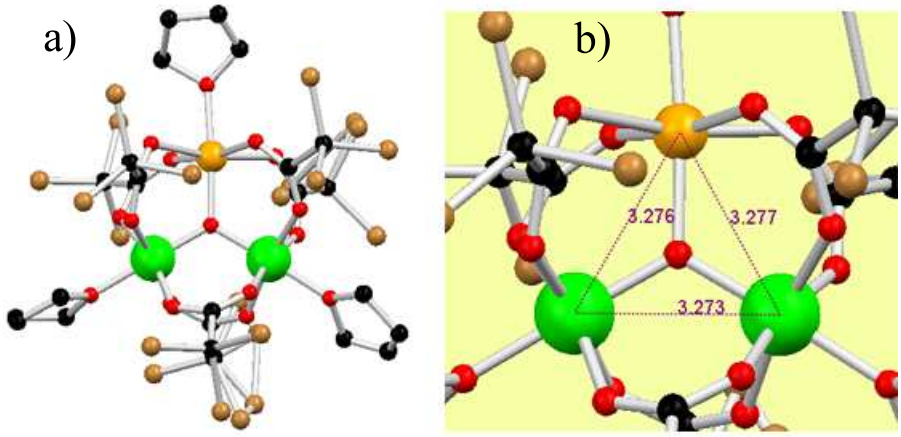

Figure 5.5: a) X-ray diffraction structures of Cr_2Cu. Colors: Cr, green; N, light blue; C, black; O, red; Cu, orange; Br, brown. Hydrogens are omitted for simplicity. b) magnification of a) with measurements of Cr-Cr and Cr-Cu distances measured in Å.

5.2 Cr_2Cu

If a Chromium ion ($s = 3/2$) is substituted by another $3d$ metal, we obtain an heterometallic trimer with intrinsically two J constants, regardless of the actual geometrical structure. Here the case where a vertex of the Cr triangle is substituted by one copper ($s = 1/2$) is reported. Low temperature susceptibility, magnetization and specific heat experiments have been performed. These allow to determine the microscopic parameters of the spin hamiltonian that was diagonalized exactly. The final aim of this work, is to use heterometallic trimers to probe the local magnetic features within spin clusters by X-rays Magnetic Circular Dichroism (XMCD), analogously to what done for the case of Cr_6InNi and Cr_7InNi (see the previous chapter). XMCD spectra, reported in Appendix A.2, were used to separately investigate local symmetries, electronic configuration, orbital, and spin magnetic moments of the magnetic ions. Information on the magnetization obtained by XMCD have been compared with microscopic spin hamiltonian derived from bulk measurements.

5.2.1 Structure

Microcrystalline samples of:

$$[Cr_2CuO(O_2CCBr_3)_6(C_4H_8O)_3],$$

Cr_2Cu in short, were prepared as reported in [99] and references therein. Crystallographic structure of Cr_2Cu is shown in Fig. 5.5(a) and (b). The metallic ions are placed at the vertexes of isosceles triangle being 3.273 Å the base side length (Cr-Cr distance) and 3.277(6) Å the other sides ($Cr_{1,2}$-Cu distance), as enlightened by Fig. 5.5(b). Their chemical bridging occurs by means of the central Oxygen and two 1,3-bridging pivalates that provide antiferromagnetic (AF) superexchange coupling between metal centers. The local symmetry of each Chromium or Copper, is represented by an octahedron with six apical O atoms. Each Cr is in a slightly distorted octahedral environment, with the six O equidistant from the metal ion (1.97 $\pm$ 0.1 Å). On the contrary, the CuO_6 octahedron is stretched along the c-axis by Jahn-Teller effect (D_{4h}), with four in-plane O equidistant from the metal ion (1.95 $\pm$ 0.04 Å) and the two out of plane more distant (2.24 $\pm$ 0.04 Å). However, the very similar bond lengths and angles around the Cr^{3+} and Cu^{2+} ion leads the assumption of a nearly pure O_h symmetry even for what concerns charge and spin densities. Supplementary crystallographic data for this compound are contained in the CCDC-792732 and CCDC-792733 that can be consulted free of charge from The Cambridge Crystallographic Data Centre via www.ccdc.cam.ac.uk/data_request/cif.

5.2.2 Thermodynamic characterization

The magnetic features of Cr_2Cu clusters have been fully characterized by means of bulk measurements at low temperature: ac susceptibility, magnetization and specific heat. All the experiments were carried out on microcrystalline samples. The ac-susceptibility $\chi(T)$, obtained by applying an oscillating field of 10 Oe at frequencies 90 Hz frequency, is reported in Fig. 5.6. Qualitatively, it is possible to notice that the susceptibility starts to saturate at 10 K suggesting that the ground state is relatively well separated from the excited levels. Below $\sim$ 10 K the χT vs T curve approaches the value of 1.74 emu K mol^{-1} pointing to a spin $S = 3/2$

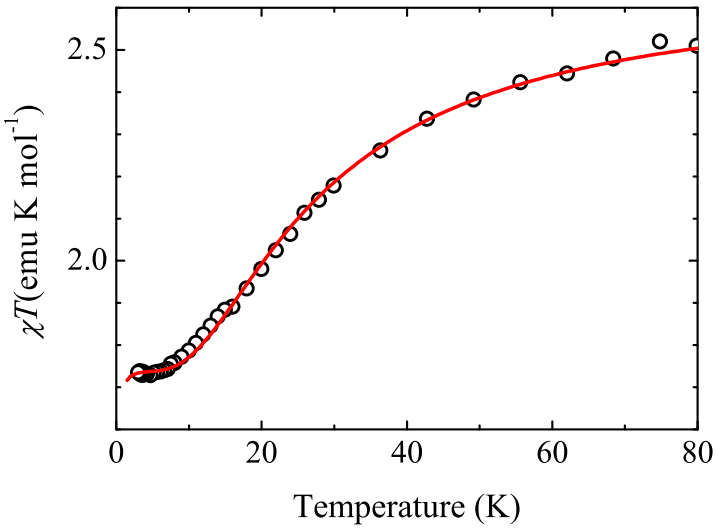

Figure 5.6: ac-susceptibility χT vs T (empty black circles), the red solid line is the best fit curve calculated from the diagonalization of Eq. 5.1 as described in the text.

ground state of the molecule in zero magnetic field. In Figure 5.7 magnetization $M(H)$ curves measured by using extraction method and static magnetic fields up to 7 Tesla are shown. At 2.2 K the magnetization data tends to saturate to 3 μ_B, confirming the presence of an $S = 3/2$ ground state. The temperature dependence of the specific heat $C(T)$ at different applied magnetic fields is shown in Fig. 5.8. The $C(T)$ curve at zero field exhibits a pronounced Schottky anomaly due to splitting of the ground state. This anomaly has maximum at around 0.4 K that, in a simple two level Schottky model, gives an energy gap between two equally degenerated multiplets of about 1 K.

For a more quantitative analysis, each Cr_2Cu magnetic molecule can be described by the following microscopic spin Hamiltonian:

$$\begin{aligned} H &= \sum_{i,j} J_{i,j} \overrightarrow{S}_i \cdot \overrightarrow{S}_j + \mu_B \overrightarrow{H} \cdot \sum_i g_i \overrightarrow{S}_i + \\ & D_{ex} \sum_{i=1,2} (2S_{i,z}S_{3,z} - S_{i,x}S_{3,x} - S_{i,y}S_{3,y}) \end{aligned} \tag{5.1}$$

where site 3 corresponds to the Cu^{+2} ion. The first term in Eq. 5.1 is the isotropic Heisenberg exchange coupling, the second term is the Zeeman interaction and

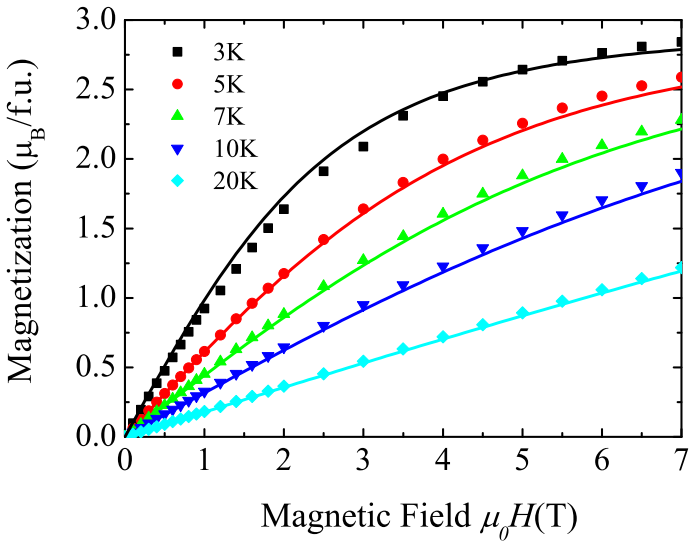

Figure 5.7: dc-magnetization vs magnetic field at different temperatures. 3 K curve tends to saturate to $3\mu_B$ at 7 Tesla, as expected for $S = 3/2$ ground state. Solid lines are result of best fit calculations explained in the text.

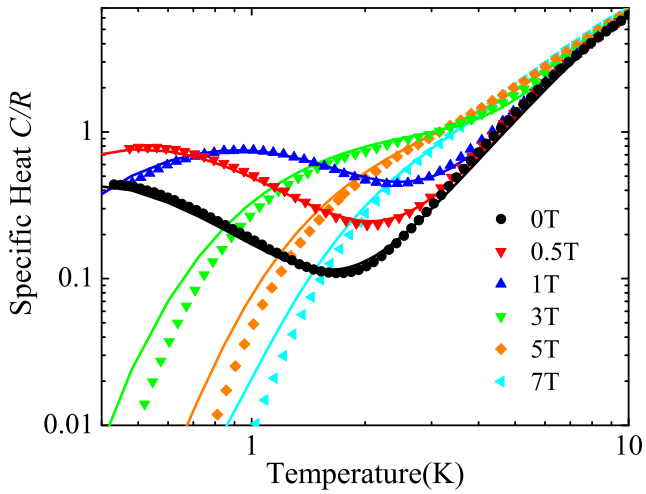

Figure 5.8: Temperature dependence of specific heat normalized to the gas constant R and measured for different constant magnetic fields. Solid lines are the best fit results obtained from diagonalization of Eq. 5.1.

the last one describes the axial contribution to the Cr-Cu anisotropic exchange coupling. Non-axial anisotropy contributions are neglected because they are not needed to reproduce experimental data. It was checked that axial crystal-field interactions at Cr sites produce very small effects on the energy levels of Cr_2Cu. The Hamiltonian has been exactly diagonalized and all the states have been included in the calculations of the observables. Two distinct isotropic exchange parameters $J_{i,j}$ were assumed, one describing Cr-Cr interaction and one the Cr-Cu coupling. These parameters have been determined by fitting the temperature-dependence of the magnetic susceptibility (see Fig. 5.6), yielding $J_{Cr-Cr} = 89$ K and $J_{Cr-Cu} = 446$ K. As far as gyromagnetic factors are concerned, $g_{Cr} = 1.98$ and $g_{Cu} = 2.25$ have been used. The first one is the typical value of Cr^{3+} and the second one is determined from XMCD (see Appendix A.2). The large difference between the two exchange constants removes magnetic frustration and leads to a $S = 3/2$ ground quartet separated by about 40 K from excited states. In the lack of anisotropy the spin wavefunctions corresponding to this quartet are $|S_{1,2} = 2, S = 3/2, M >$, where $\overrightarrow{S}_{1,2} = \overrightarrow{S}_1 + \overrightarrow{S}_2$ and M is the total spin projection quantum number. In Fig. 5.9 the low-lying energy level pattern is plotted. The energy levels are obtained from the diagonalization of Eq. 5.1 and with an external magnetic field oriented at $\Theta = 0°$ and $\Theta = 90°$ respect to the $\widehat{z}$ axis. The model is characterized by an $S = 3/2$ ground multiplet separated by about 40 K from excited states. The low-temperature anomaly in the zero-field specific heat implies a splitting of the ground multiplet into two doublets (as magnified in the inset of Fig. 5.9), due to magnetic anisotropy. The temperature and magnetic field dependence of the specific heat can be well reproduced by assuming $D = 0.7$ K (see solid lines in Fig. 5.8). Finally, the calculated temperature and magnetic-field dependence of the powder-averaged magnetization (solid lines in Figure 5.7) is in very good agreement with experimental results.

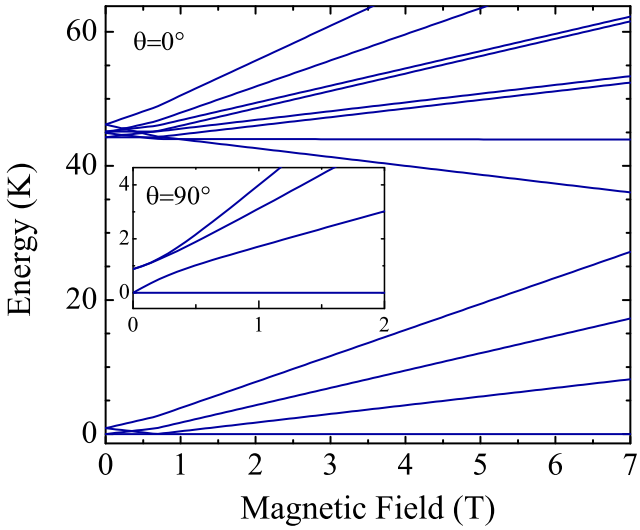

Figure 5.9: Energy levels scheme resulting from the theoretical modelling described in the text and calculated for $\Theta = 0°$. Energy is plotted as $E - E_0$, being E_0 the energy of the ground state. (Inset) magnification of the ground state energy levels calculated for $\Theta = 90°$

Conclusions

In this chapter I have extensively studied the magnetic properties of two new molecular Cr-based spin trimers, namely Cr_3 and Cr_2Cu. I characterized both the derivatives by low temperature susceptibility, magnetization and heat capacity measurements and this allowed to extract the essential parameters of their microscopic spin Hamiltonians. It turns out that in Cr_3, the degeneracy of the $S = 1/2$ ground state due to spin frustration is removed by a distortion of the triangle leading to two doublets separated by about 1 K. The system is well described by the two exchange constants $J = 31.3$ K and $J' = 39.7$ K that take into account the structural distortion of the equilateral trimer. In the case of Cr_2Cu, that is intrinsically isosceles, the ground state turns out to be a $S = 3/2$ multiplet, split in two doublets with $\sim$1 K zero field splitting, and well separated ($\sim$ 40 K) from the first excited state $S = 5/2$. To describe this system the exchange constant referred to the Cr-Cr base side is 89 K, very different to that of 446 K relative to the Cr-Cu sides. In the case of Cr_2Cu, spin hamiltonian calculations, based on fitting susceptibility, magnetization and specific heat allow to analyze further X-ray circular dichroism measurements, performed to study the local properties of the different metal ions. From the analysis of spectroscopic data, reported in Appendix A.2, a detailed description of the oxidation states and the local symmetries was obtained. Finally, the separate contributions of Cu and Cr to the total magnetic moment of Cr_2Cu were analyzed. It was found that, in presence of an applied magnetic field, the projection of the Cu spin is opposite to that of Cr. This is a local property that reflects the ground state of the molecule and it is evident only at low temperature.

All the experimental techniques and theoretical description reported have contributed together to a sophisticated level of description of the physical state. Overall, these results show a deep control of the magnetic features of molecular trimers that may constitute the basis to more sophisticated experiments.

Chapter 6

Magnetic coupling in supramolecular Cr_7Ni spin systems

In this chapter the study of magnetic coupling between novel Cr_7Ni rings derivatives tailored by supramolecular chemistry is presented. In detail, the work is organized as follows. Section 6.1 is devoted to a complete magnetic characterization of new type of *purple*-Cr_7Ni, that constitutes the brick for the novel supramolecular derivatives. The characterization is supported by means of low temperature thermodynamic properties and spin Hamiltonian calculations. In the successive section 6.2, the magnetic coupling in supramolecular structures consisting of more than two Cr_7Ni weakly coupled antiferromagnetic rings is discussed. In 6.3 the attention is focus on mixed linked derivatives, constituted by different Cr_7M units in the *purple* and *green* derivative. Finally, in section 6.4 a systematic investigation of inter-ring interaction on dimers formed by identical units but with different linkers is carried out by means of experimental characterization. The results are in agreement with Density Fluctuation Theory (DFT) calculations, reported in Appendix B for completeness, that, in addiction, explain the mechanism behind the transmission of spin information through the chemical linkers.

My contribution to this work concerns the thermodynamic characterization of all the derivatives by low temperature specific heat, ac-susceptibility in the temperature range $2 - 300$ K and dc-magnetization by means of 7T-PPMS system.

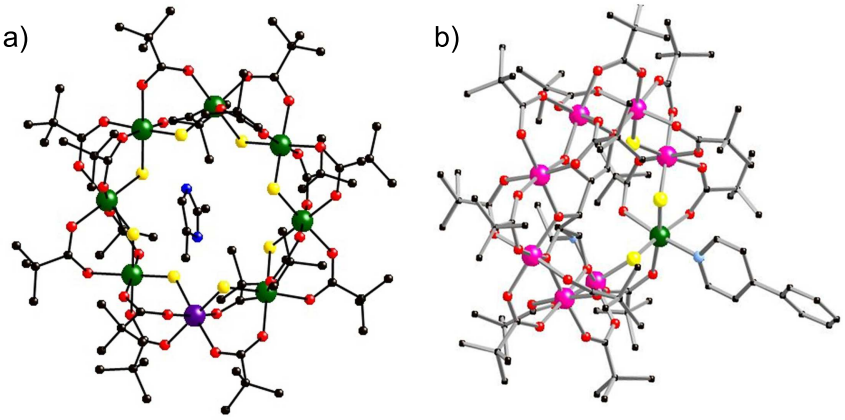

Figure 6.1: Crystalographic structures of a) *green*-Cr_7Ni and b) *purple*-Cr_7Ni. Colors: Cr, green(a), purple(b); Ni, purple(a), green(b); F, yellow; O, red; C, black; N, blue. Hydrogens are omitted for simplicity.

The chemical synthesis of the samples was carried out by Dr. Gregory Timco and coworkers of the group of Prof. Winpenny in Manchester. Micro-SQUID magnetization was performed in Grenoble by Dr. Andrea Candini and Dr. Wolfgang Wernsdorfer. Spin-hamiltonian calculations were carried out by Dr. Stefano Carretta in Parma. Finally, spin density analysis on the *purple*-Cr_7Ni dimers was effected by Dr. Valerio Bellini in Modena.

6.1 *Purple*-Cr_7Ni ring

In 2008 a new derivative of Cr_7Ni, hereafter called *purple*-Cr_7Ni, was synthesized [154]. As visible in Fig. 6.1, in the new molecule, with respect to the original *green*-Cr_7Ni ring derivative [47], five bridging fluorides are substituted by alkoxides. The replacement of fluoride with alkoxide within the coordination sphere of the majority of Cr^{+3} ions causes a change in color of the crystals from dark green to purple, from this the names. This also affects the magnetic levels of each ring, as shown in the characterization below. Besides, and most importantly, thank to the presence of a terminal ligand, *purple*-Cr_7Ni offers an ideal opportunity to link the rings anchoring directly onto the Ni sites organic linkers with or without

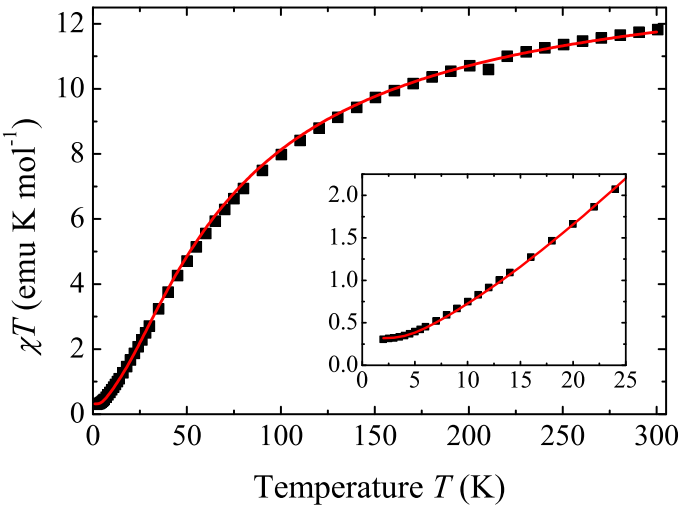

Figure 6.2: ac-susceptibility χT vs T of purple-Cr_7Ni rings (squares). Solid line represents theoretical simulation obtained from the microscopic spin Hamiltonian Eq. 6.1, described in the text, with a single average exchange constant $J/k_B = 22.9$ K. Inset: Magnification at low temperatures. The measurement was performed in Manchester by Dr. F. Tuna by means of a commercial SQUID in the 2 K $< T <$ 300 K temperature range.

metal ions. Finally, exploiting faster chemical reaction at Ni site, it is possible to systematically change the aromatic linker thus tuning the degree of conjugation.

In Fig. 6.2 the temperature-dependence of susceptibility χ for single *purple*-Cr_7Ni ring is reported. Results are plotted as χT vs T. At low temperature the curve saturates and, as visible from the inset, at 2 K reaches the value of 0.3 emu K/mol, in agreement with the behavior of an effective $S = 1/2$, as found for the *green* derivative.

The low-temperature specific heat (C) at different applied magnetic fields (H) is shown in Fig. 6.3. The specific heat measurements are performed on pressed microcrystals by using the two-tau method; data are normalized to the gas constant R. The $C(T; H = 0)$ curve shows a dominant lattice contribution at high temperature, while the magnetic term is characterized by a Schottky anomaly at around 4 K, mainly due to the doublet-quadruplet energy difference; no evidence of a zero field splitting appears below 1 K. The appearance, for $H \neq 0$, of a well defined Schottky anomaly at low temperature and its dependence

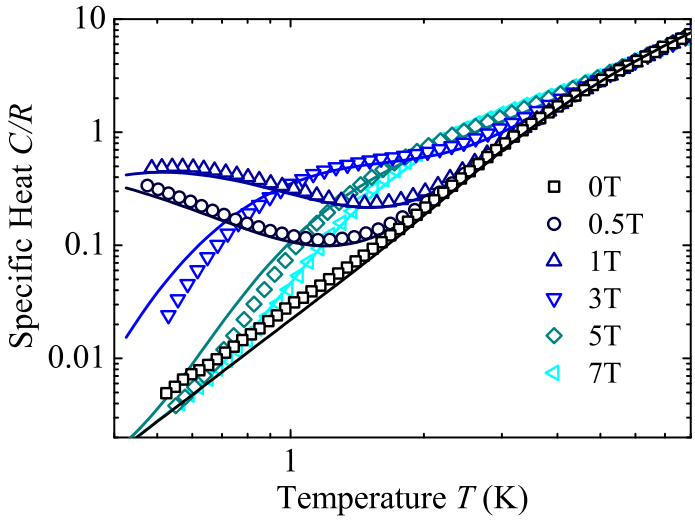

Figure 6.3: Heat capacity normalized to the gas constant R of *purple*-Cr_7Ni. (Solid lines) are theoretical results obtained diagonalizing Eq. 6.1 (Dr. S. Carretta).

on the magnetic field essentially reflects the removal of the Kramers degeneracy in the ground-state doublet and the lowering in energy of the $S = 3/2$ multiplet. These $C(T, H)$ curves are very similar to those measured for the *green*-Cr_7Ni rings, reported in Ref. [49]. The small differences between the specific heat of the two derivatives can be explained by different values of ion-ion exchange interaction and anisotropy in the rings. As matter of fact these variations are evident at zero field and at the highest field where the different gaps between multiplets become more significant.

To have a more quantitative analysis, the experimental data can be theoretically interpreted by a microscopic spin-Hamiltonian approach. In fact, despite the complexity of the molecular system, the magnetic behavior of the ring can be described by [23, 50]:

$$\begin{aligned}\mathcal{H} &= \sum_{i=1}^{8} J\mathbf{s}_i \cdot \mathbf{s}_{i+1} + \sum_{i=1}^{8} d_i \left[s_{z,i}^2 - s_i(s_i+1)/3\right] \\ &+ \sum_{i<j=1}^{8} D_{ij}[2s_{z,i}s_{z,j} - s_{x,i}s_{x,j} - s_{y,i}s_{y,j}] + \mu_B \sum_{i=1}^{8} \mathbf{H} \cdot \mathbf{g}_i \cdot \mathbf{s}_i, \qquad (6.1)\end{aligned}$$

where z is the ring axis, site 8 corresponds to the Ni^{2+} ($s = 1$) ion and sites 1-7 to Cr^{3+} ($s = 3/2$). The four terms in $\mathcal{H}$ account for the isotropic exchange, the axial contributions to the crystal-field and the intracluster dipole-dipole, and for the Zeeman interactions, respectively. The values of the crystal-field parameters are assumed to coincide with those of the *green*-Cr_7Ni compound [52]: $d_{Cr} = -0.35\,\mathrm{K}$ and $d_{Ni} = -4\,\mathrm{K}$. The dipolar coefficients D_{ij} have been calculated in the point-dipole approximation, while the gyromagnetic tensor components of the Cr ions are: $g_{xx}^{1-7} = g_{yy}^{1-7} = g_{zz}^{1-7} = 1.98$. The average exchange parameter (considering only one J for all the ring) is determined by simultaneously fitting $C(T, H)$ and $\chi(T)$ obtaining the value $J/k_B = 22.9$ K, about 34% greater than the *green*-Cr_7Ni exchange constant $J_{Cr-Cr}/k_B = 17$ K (in that case a different exchange constant to describe the Ni-Cr interaction was used), indicating a stronger antiferromagnetic coupling between the ions in the *purple*-Cr_7Ni ring. This leads to a splitting $\Delta = 19$ K between the $S = 1/2$ ground doublet and the first $S = 3/2$ excited quadruplet. The result of simulations for susceptibility and specific heat, performed by Dr. S. Carretta in Parma, are the solid lines reported in Figs. 6.2 and 6.3, respectively. For the lattice parameters we used the set of values provided by the best fit of Eq.(1.14): $\Theta_D = (147 \pm 10)$ K, $\lambda = (0.48 \pm 0.03)$ K^{-1}. Finally, the analysis of the EPR data measured in Manchester (reported in the next chapter in Fig. 7.7) allows a precise estimate of the gyromagnetic tensor components. The single *purple*-Cr_7Ni ring spectrum is characteristic of a ground state doublet, with lines sharper than those measured in *green*-Cr_7Ni; this might be due to the F-substitution, that reduces the hyperfine-induced decoherence [55]. The effective values for the g tensor of the ground doublet are: $\bar{g}_{xx} = \bar{g}_{yy} = 1.84$ and $\bar{g}_{zz} = 1.78$. These can be reproduced by assuming a slightly anisotropic Ni gyromagnetic tensor ($g_{xx}^{Ni} = g_{yy}^{Ni} = 2.19$, $g_{zz}^{Ni} = 2.24$). In calculating all the above quantities, a spherical average has been performed to account for the random orientation of the molecules in the powder sample.

6.2 Supramolecular systems $(Cr_7Ni)_n$ with $n > 2$

Purple derivatives

In Fig. 6.4 are depicted the structures of some *purple*-Cr_7Ni linked rings, showing the capability to vary the type or length of the linker and the number of units to link. In particular, in Fig. 6.4(c) a 'trimer' of *purple*-(Cr_7Ni) cluster is depicted. This has the chemical formula:

$$[Cr_7NiF_3(Etglu)(O_2CtBu)_{15}]_3, \text{ shortly } (Cr_7Ni)_3,$$

with 2,4,6-*Tri*(4-*pyridyl*)-1,3,5-*triazine* as organic linker; while the simplest tetramer, represented in Fig. 6.4(d), is

$$[Cr_7NiF_3(O_2CCMe_3)_{15}(C_8H_{14}NO_5)]_4, \ (Cr_7Ni)_4 \text{ in short,}$$

with 5,10,15,20-*Tetra*(4 − *pyridyl*)*porphyrin* linker. This last can be synthesized adding to the linker a central Cu (Fig. 6.4(e)) or a Zn (not shown), named in short $(Cr_7Ni)_4Cu$ and $(Cr_7Ni)_4Zn$, respectively.

Figure 6.5 shows the specific heat for all these derivatives. The curves are compared with the signal of the single *purple*-Cr_7Ni (solid lines) multiplied by three in the case of the 'trimer' (panel (a)) and by four in the case of the 'tetramers' (panels (b)-(d)). Moreover, for $(Cr_7Ni)_4Cu$, also the contribution of the copper with $S = 1/2$ was summed. Looking at the in-field curves, the features are very similar for each derivative and the data overlap with those referring to the single rings. This confirms that the magnetic features of the single ring are preserved. For the zero-field specific heat curves only slight differences can be noted with respect to the single ring behavior. In particular, for $(Cr_7Ni)_4Cu$ an upturn below 0.5 K is visible, but it is difficult, since the high number of rings involved, to associate quantitatively to an inter-ring interaction. Also the EPR spectra measured in Manchester (not shown here) are quite broaden thus it is not possible to distinguish inter-ring interactions. This induces to think that, in view of the number of bonds and the length of the linkers, the magnetic coupling, is too weak to be detected at the current temperatures. In spite of this the *purple*-$(Cr_7Ni)_n$ remain intriguing system that should be investigated more deeply and they demonstrate the capability achieved by chemists to control and to engineer supramolecular structures also with more than two molecular units.

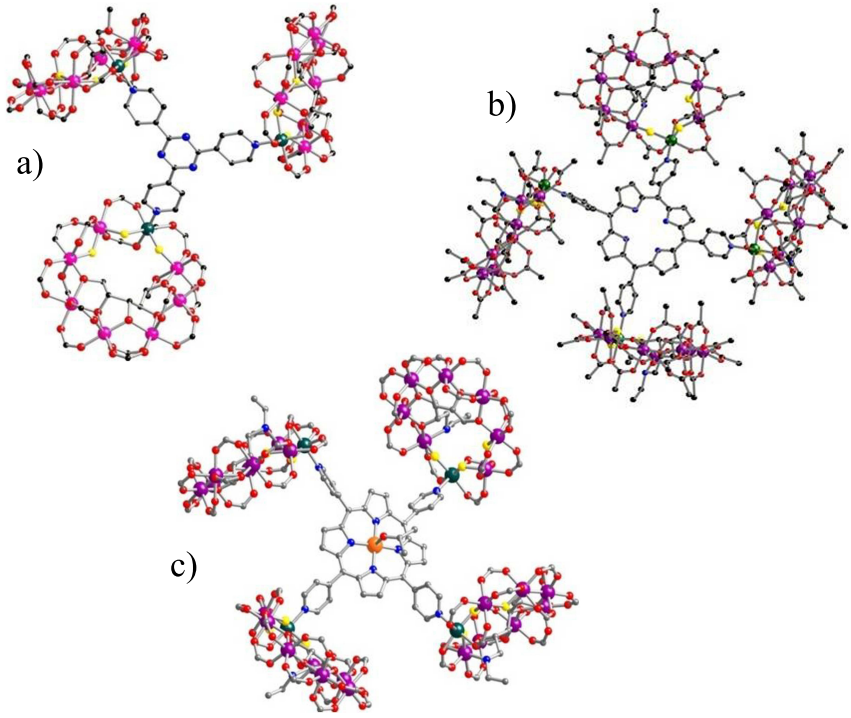

Figure 6.4: Crystallographic structures of some linked *purple*-Cr_7Ni rings. In a) is depicted a trimer, while in b) and c) four rings are bridged respectively with organic and metallo-organic linker.

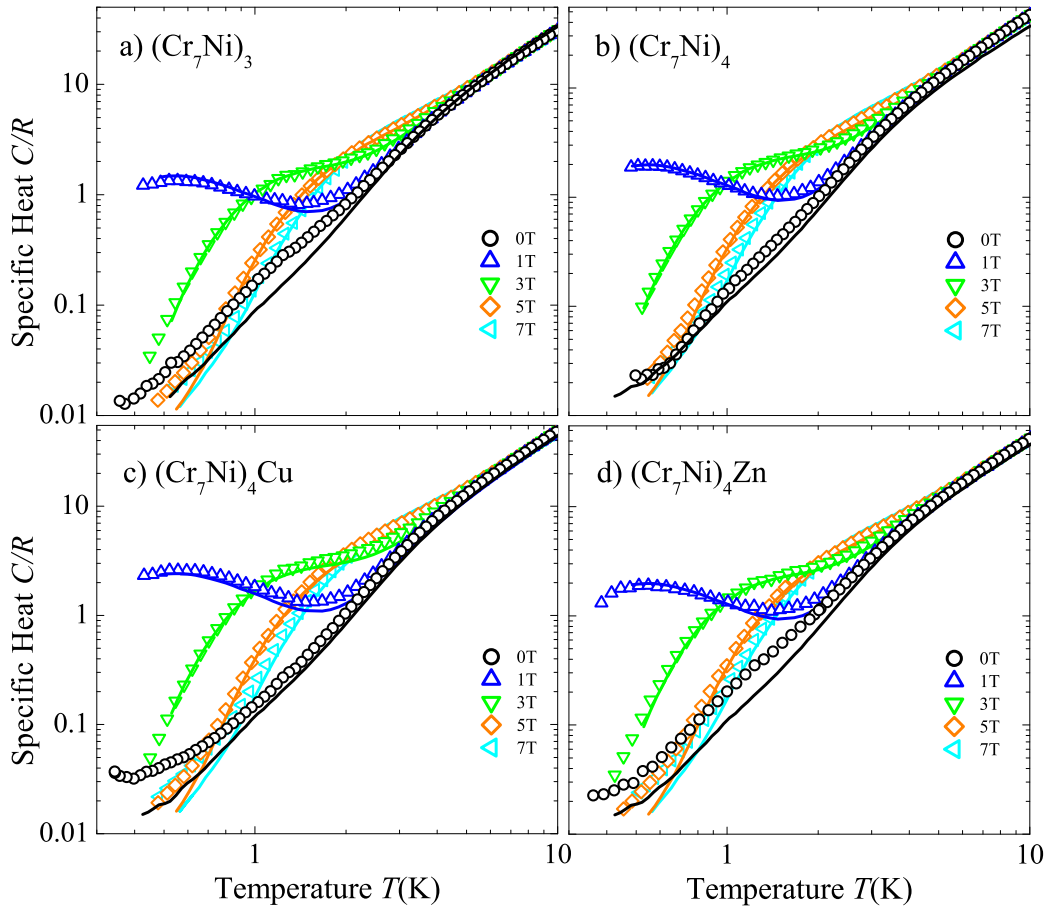

Figure 6.5: Specific heat as function of the temperature for: a) $(Cr_7Ni)_3$, b) $(Cr_7Ni)_4$, c) $(Cr_7Ni)_4Cu$ and d) $(Cr_7Ni)_4Zn$. For each system the curves are compared with the signal of the single *purple*-Cr_7Ni ring (solid lines) multiplied by three for a) and by four for the others. In the case of c) also the contribution of Cu with $S = 1/2$ was summed for comparison.

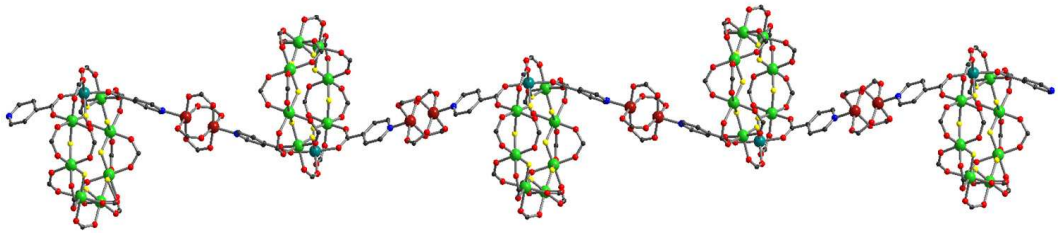

Figure 6.6: Crystallographic structures of *green*-Cr_7Ni infinite chain in which Cr_7Ni rings are alternate to dimers of Cu ions.

Green-$(Cr_7Ni)Cu_2$ chain

In the case of *green*-Cr_7Ni derivative an infinite chain was recently synthesized, its chemical formula is:

$$[\{(C_3H_7)_2NH_2Cr_7NiF_8(O_2CCMe_3)_{14}(O_2CC_5H_4N)_2\}\{Cu_2(O_2CCMe_3)_4\}]_n,$$

shortly named $(Cr_7Ni)Cu_2$ chain.

The structure, shown in Fig. 6.6, is constituted by the alternation of one *green*-Cr_7Ni ring and one dimer of Cu ions, thus representing the iteration of the finite linked system presented in the introductive chapter, in Fig. 1.4(c). For the finite dimer, the magnetic interaction was demonstrated [70] to be permanently switched off by the copper ions that are antiferromagnetically arranged giving $S = 0$. We can then expect a similar result also for the infinite chain.

In the upper panel of Figure 6.7 the ac-susceptibility product χT versus T for the $(Cr_7Ni)Cu_2$ chain is reported. Data are compared with those of the single *green*-Cr_7Ni, taken from Ref. [47], showing similar behavior and saturation value at 2.2 K (see the inset) and indicating $S = 1/2$ ground state. This confirms that the chain, from the magnetic point of view, behaves as a collection of non-interacting Cr_7Ni rings. Magnetization curve of the chain at $T = 2.2$ K, plotted in the lower panel of Fig. 6.7, rises with field similarly to that of the single ring (red circles) [47] up to 3.5 T. For higher fields data referred to single ring start to bend, while those relative to the chain continue to rise approximately with the same rate, indicating that the excited levels of the chain are closer (and thus more populated at 2.2 K and high fields) with respect to those of the single ring.

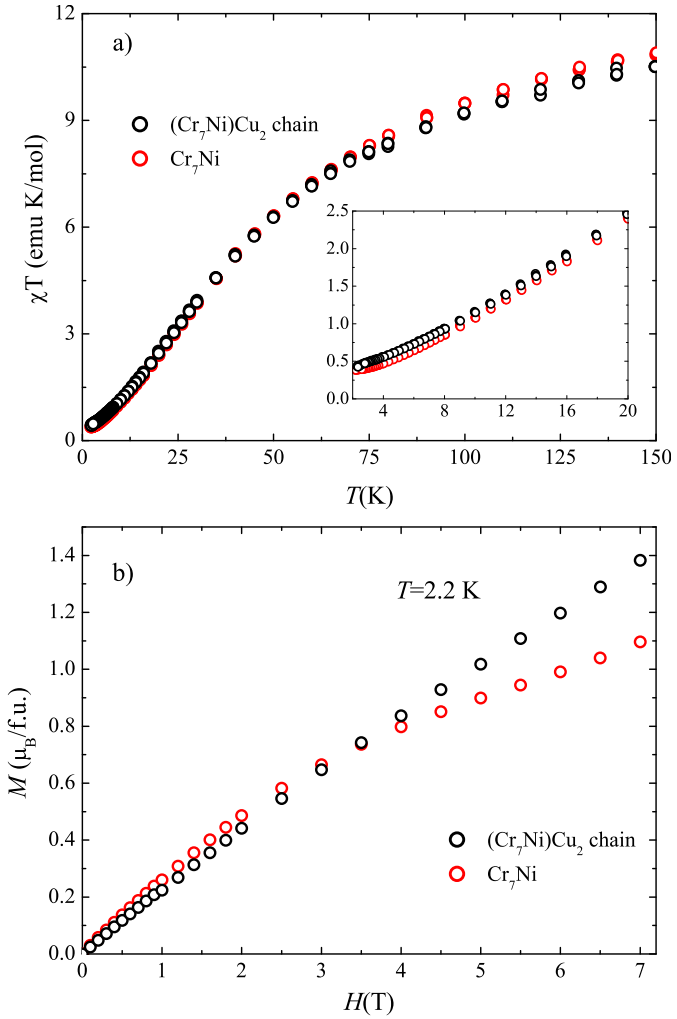

Figure 6.7: a) ac-susceptibility and b) dc-magnetization for $[(Cr_7Ni)Cu_2]_n$ (black) compared with those of Cr_7Ni (red) [47].

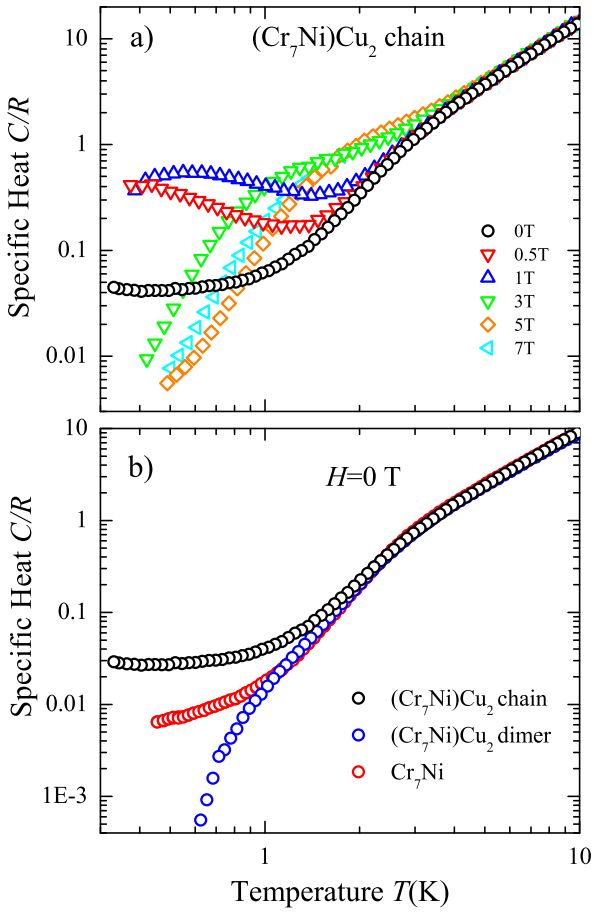

Figure 6.8: a) Temperature dependence of the specific heat for $(Cr_7Ni)Cu_2$ chain at several magnetic field values. b) Comparison of zero field curve for $(Cr_7Ni)Cu_2$ chain (black) with those of the dimer $(Cr_7Ni)Cu_2$ (blue) [70] and of the single ring Cr_7Ni (red) [49]; data are scaled on that of the single ring to enlighten the differences.

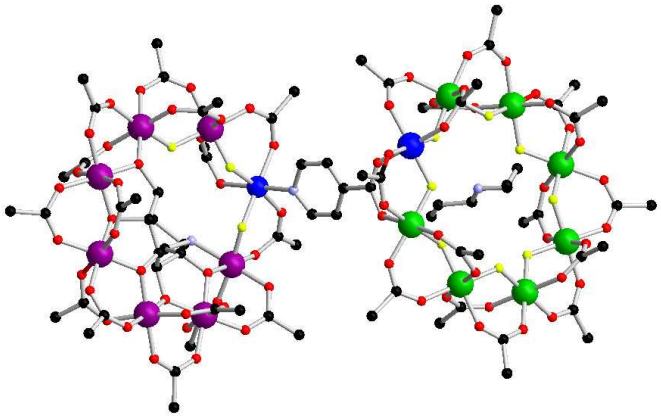

Figure 6.9: Structure of *purple*-(Cr_7M)/*green*-(Cr_7M') dimers deduced by X-ray diffraction experiment. Color: M, blue; Cr, purple/green; O, red; C, black; F, yellow; N, light blue. To make a clearer picture pivalate groups are truncated, while Hydrogens are omitted.

In Figure 6.8(a) the specific heat of the $(Cr_7Ni)Cu_2$ chain for several magnetic field is shown. The in-field curves are very similar to the specific heat of the single Cr_7Ni at the corresponding fields; while in the case of zero field a plateau is present for temperatures below ~ 1 K (see Fig. 6.8(b)). This behavior is different also to specific heat curve at zero field of the $(Cr_7Ni)Cu_2$ dimer [70], reported in the lower panel of the same figure, that abruptly goes toward zero for $T < 1$ K. The plateau is an indication of weak coupling between different molecular spin clusters. However, EPR spectra do not show any visible interaction, so further work is needed to clarify if and how rings are connected.

6.3 *Purple*-(Cr_7M)/*Green*-(Cr_7M') dimers

Very recently, Cr_7M antiferromagnetic rings were synthesized in the *purple* and *green* variations, analogously to Cr_7Ni molecules, substituting to the Ni ion other $3d$ metals M with $+2$ oxidation state (like Mn and Zn). This opens up the possibility to produce novel mixed structures, linking together *purple*-Cr_7M and *green*-Cr_7M' clusters. The dimer shown in Fig. 6.9 is an example with a pyridine group as linker and with the general chemical formula:

$$\{[Cr_7MF_3(O_2CCMe_3)_{15}(C_8H_{14}NO_5)]\ [(C_3H_7)_2NH_2]$$

$$[Cr_7M'F_8(O_2CCMe_3)_{15}(O_2CC_5H_4N)]\}$$

In the following are discussed some representative cases of such dimer having:

- *purple*-Cr_7Ni/*green*-Cr_7Ni;
- *purple*-Cr_7Ni/*green*-Cr_7Mn and *purple*-Cr_7Mn/*green*-Cr_7Ni;
- *purple*-Cr_7Zn/*green*-Cr_7Ni.

The specific heat of the first molecule, *purple*-(Cr_7Ni)/*green*-(Cr_7Ni), is shown in Fig. 6.10. In the top panel of the figure, data are compared with the sum of the specific heat measured for the *purple*-Cr_7Ni and *green*-Cr_7Ni single rings. The in-field curves are almost superimposed, denoting that also in this dimer, analogously to the supramolecular *purple* derivatives shown previously, the features of the single rings are preserved. Conversely, zero field curves are clearly divergent for temperatures below about 1 K. The upturn in the zero-field specific heat is produced by the Schottky anomaly due to the gap between singlet and triplet state, thus demonstrating that there is an interaction between the two effective $S = 1/2$ spin rings.

To have a quantitative analysis we consider an effective model as sketched in the inset of Fig. 6.10(b) where we take into account only the singlet and triplet state that are separated by the energy gap Δ. Moreover, a small anisotropy can be included which causes the energy splitting Δ_{an} in the triplet state. The simulation, solid lines plotted in Fig. 6.10(b), is in good agreement with the experimental data taking as best fit values $\Delta = 0.15$ K and $\Delta_{an} = 0.07$ K.

A different situation occurs when in one ring a Mn ($s = 5/2$) ion is substituted to the Ni ($s = 1$). In this case indeed, also the ground state spin of the modified ring is changing from $S = 1/2$ to $S = 1$ [50, 155]. The resulting specific heat is shown in Fig. 6.11 considering both the cases where Mn is substituted in the *green* (upper panel) or in the *purple* (lower panel) ring. In Fig. 6.11(a) the specific heat of the dimer is compared with the sum of the specific heats of the single *purple*-Cr_7Ni and *green*-Cr_7Mn (solid lines). Data referred to the single rings are completely superimposed to those of the dimer both for the curves in field than for (C, $H = 0$). Thus, it is possible to say that the moieties in the dimer are integer but if there is some interaction this is too weak to be appreciated at

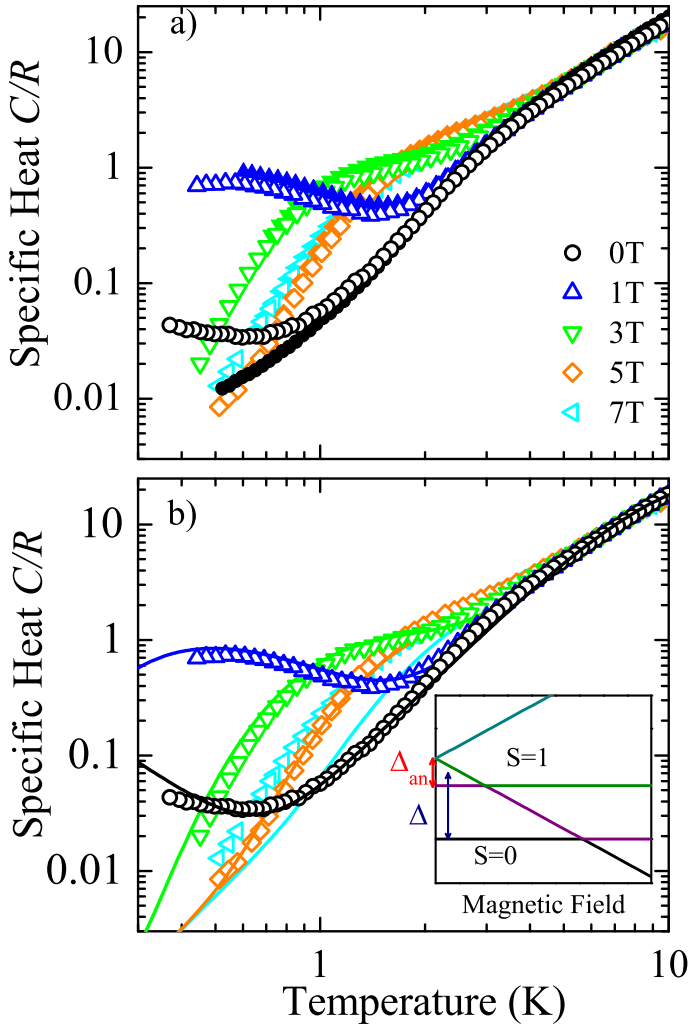

Figure 6.10: (Empty markers) specific heat for *purple*-(Cr_7Ni)/*green*-(Cr_7Ni) dimer taken on polycrystalline sample and normalized to the gas constant R. In a) the curves are directly compared with the sum of the experimental specific heats of *purple*-Cr_7Ni and *green*-Cr_7Ni single rings at the corresponding magnetic fields (full markers). In b) the specific heat is simulated (solid lines) considering for the interacting rings the low-lying energy levels depicted in the inset and depending by the two parameters Δ and Δ_{an}.

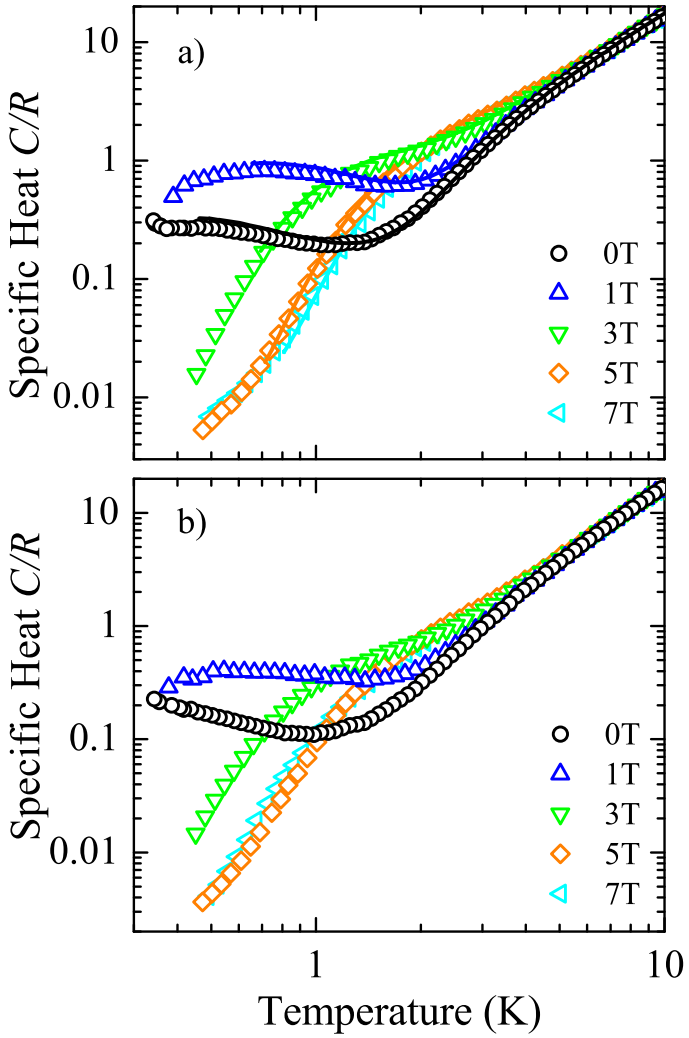

Figure 6.11: Specific heat for a) *purple*-(Cr_7Ni)/*green*-(Cr_7Mn) and b) *purple*-(Cr_7Mn)/*green*-(Cr_7Ni) dimers normalized to the gas constant R and for several magnetic field values. In a) solid lines represent the sum of the measured specific heats of *purple*-(Cr_7Ni) and *green*-(Cr_7Mn) single rings.

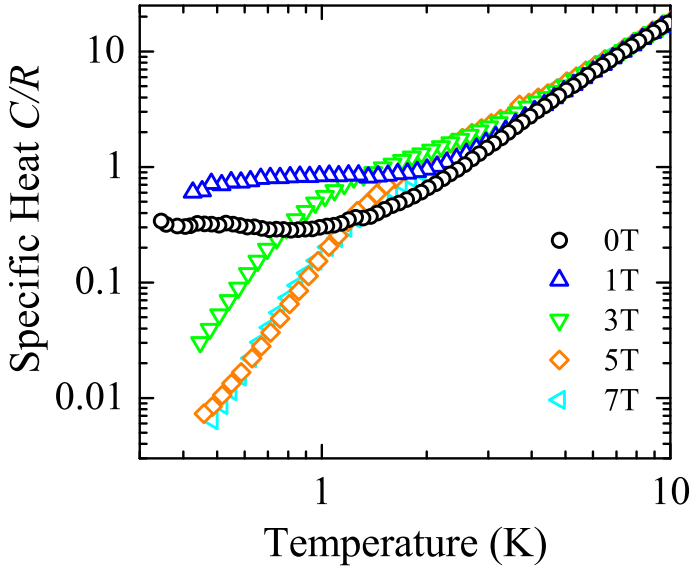

Figure 6.12: Specific heat for *purple*-(Cr_7Zn)/*green*-(Cr_7Ni) dimers normalized to the gas constant R and for several magnetic field values.

our lowest temperature (~ 0.3 K). Moreover, in this case also the closer excited states contribute to the broad Schottky anomaly, thus making more difficult to recognize an interaction.

The last case presented is when a Zn ($s = 0$) replaces the Ni in the *purple* ring, thus giving an effective $S = 3/2$ [50] cluster. The specific heat for this dimer is shown in Fig. 6.12. Analogously to the previous case, also here the zero-field curve presents an evident flat trend for temperatures below about 1 K. This is probably due to the already populated excited states.

Note: in these days the missing specific heat measurements for the single purple-Cr_7Mn and purple-Cr_7Zn rings will be performed and completed with complementary techniques. After that it will be possible to discuss if in these derivatives a inter-ring magnetic interaction is present or not.

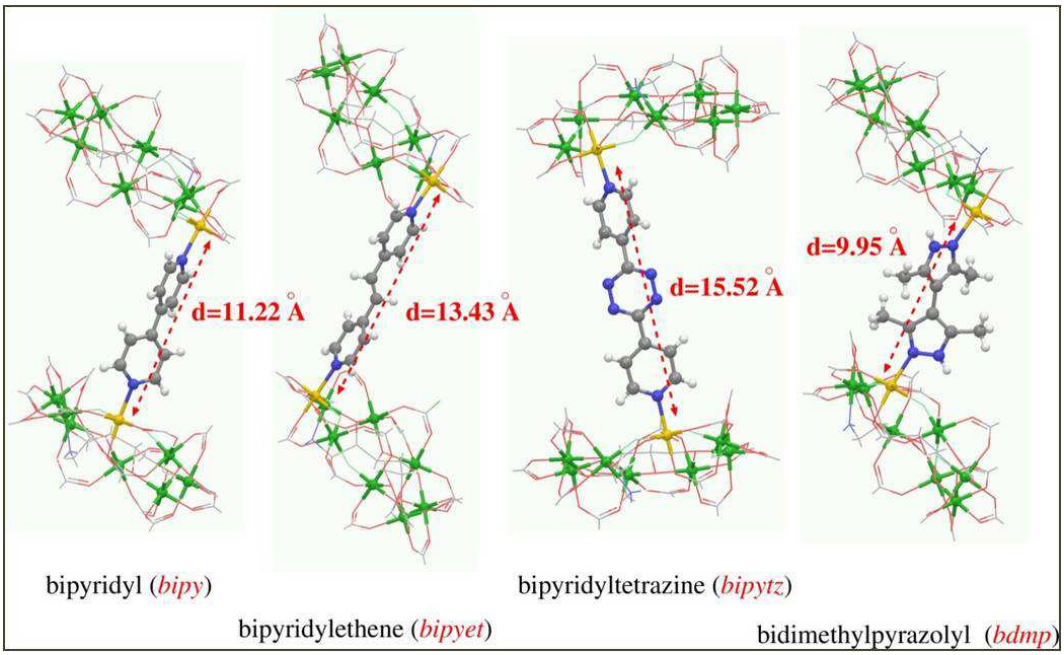

Figure 6.13: Sketch of the four dimers of Cr_7Ni rings that differ only for the organic linkers: *bipy*, *bipyet*, *bipytz* and *bdmp*. The atoms of the linkers (N, blue; C, gray; H, white) and the metal ions in the rings (Ni, yellow; Cr, green) have been highlighted. The inter-rings through-space Ni-Ni distance measurements (d) are also given for each dimer.

6.4 Changing the linker in *purple*-$(Cr_7Ni)_2$ dimers

In order to understand the mechanism of magnetic inter-ring interaction and how it depends from the linker, i. e. how the propagation of spin information at the supra-molecular (nanometer) scale works, four *purple*-Cr_7Ni dimers that differ each other only for the heteroaromatic linker between the rings were systematically investigated.

6.4.1 Experimental characterization

The *purple*-$(Cr_7Ni)_2$ dimers taken into account are sketched in Fig. 6.13. The different linkers, highlighted in the picture, are respectively:

$$\begin{aligned} L == \quad & 4,4' - bipyridyl\ (bipy,\ \text{in short}), \\ & trans - 1,2 - bipyridylethene\ (bipyet), \\ & bipyridyltetrazine\ (bipytz)\ \text{and} \\ & bidimethylpyrazolyl\ (bdmp). \end{aligned}$$

These are only four representative derivatives of a larger family of dimers, which can be synthesized. The structures of the individual rings do not vary between the derivatives, and in each case the nitrogen from a di-imine is coordinated to nickel, giving the nickel a 2F, 3O, 1N coordination sphere. Chemical synthesis and structure information of these molecules are reported in Refs. [154, 156].

In order to check the magnetic properties of the single rings upon the dimer formation, ac-susceptibility and specific heat measurements have been carried out. The product χT per ring is reported in [156]. The room temperature value, below that expected for seven Cr^{+3} ions and a single Ni^{+2} site, is consistent with the weak anti-ferromagnetic exchange within the rings. At lower temperatures, χT falls, again consistently with anti-ferromagnetic intra-ring exchange. Fitting the variable temperature susceptibility behaviour with a Hamiltonian only involving intra-ring interactions, gives an average exchange interaction of $J/k_B = 22.9$ K. To fit the magnetic susceptibility there is no need to allow for the differing bridging by fluoride and alkoxide groups within the ring. This value is completely consistent with the one obtained studying crystals of single *purple* rings.

In Fig. 6.14 the low temperature specific heat $C(T)$ for the four derivatives (colored markers) taken in presence of an external fixed 1 T magnetic field is reported. Data, relative to microcrystalline samples, are plotted as a function of temperature (T) and normalized to the gas constant R. The specific heat of the dimers has been compared with the one multiplied by two of the single *purple*-Cr_7Ni ring (black triangles) that constitutes each dimer. The theoretical calculations for the magnetic contribution to the specific heat of the single ring at $H = 1$ T are also reported (dashed line). The curves of the four compounds overlap with each other almost perfectly, reproducing the behavior of the single ring

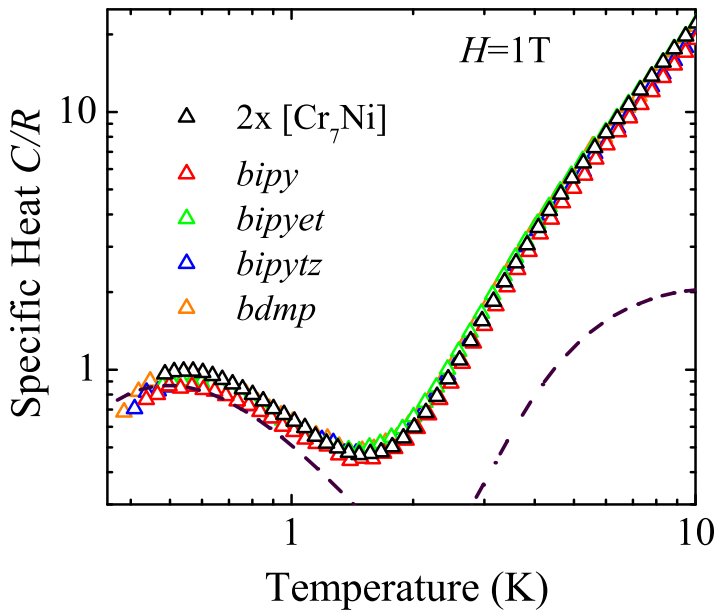

Figure 6.14: Low temperature dependence of the specific heat $C(T)$, normalized to the gas constant R and in presence of 1 T external magnetic field, for: *bipy* (red), *bipyet* (green), *bipytz* (blue), *bdmp* (orange). (Black triangles) specific heat of the single Cr_7Ni ring at 1 T and multiplied by two. (Dashed line) theoretical simulation of the specific heat magnetic contribution of the single ring calculated by the spin Hamiltonian at $H = 1$ T. In the next Chapter a detailed study of the specific heat for *bipy* dimer is reported.

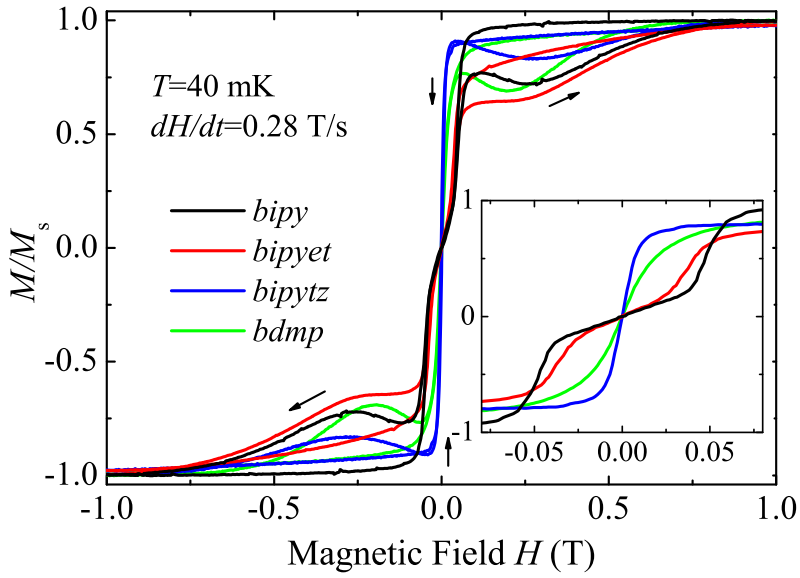

Figure 6.15: Micro-SQUID magnetization $M(H)$ vs magnetic field for: *bipy* (black), *bipyet* (red), *bipytz* (blue), *bdmp* (green). The experiments were performed at $T = 40$ mK, using a fast field sweeping rate of $dH/dt = 0.28$ T/s. Data are normalized to the saturation value M_S. (Inset) Magnification of $M(H)$ between $H = \pm 0.1$ T. For simplicity only decreasing field data are plotted. For *bipy* and *bipyet* two knees are clearly visible, evidencing the inter-rings coupling. The transitions between low and high spin states occur in correspondence of the crossing fields ± 0.05 T for $-$*bipy* and ± 0.04 T, for *bipyet*. For *bipytz* and *bdmp* similar features are not visible, indicating that the interaction between the rings is weaker than 100 mK. In the next chapter, systematic studies of micro-SQUID magnetization loops for the single ring and for the *bipy* dimer are reported.

specific heat at moderate field (1 T). This demonstrates that the pattern of the lowest lying states of the single Cr_7Ni rings are preserved also in the supramolecular systems. In particular the presence of well defined Schottky anomaly at 1 T shows that energy split between the $S = 1/2$ ground state and the first excited $S = 3/2$ state is conserved with no relevance to inter-molecular interaction that should be in energy scale below 1 K. A detailed and more quantitative study of the *bipy* dimer properties is reported in Chap. 7.

To reveal the presence of inter-rings interaction, micro-SQUID magnetization measurements at 40 mK were performed by Dr. W. Wernsdorfer. The resulting magnetization curves, normalized to the saturation value M_S, are plotted in

Fig. 6.15 for all the derivatives. In Fig. 6.15, in order to enlighten the transition between the singlet and triplet states, the magnetization cycle is magnified between $H = \pm 0.1$ T (inset of Fig. 6.15). For simplicity only the part of the hysteresis loop with decreasing field is reported. If the $S = 0$ state is the ground state in zero-field, it should be possible to see a spin-state crossing by increasing the field, with one component of the paramagnetic $S = 1$ state falling in energy as the field increases (visible as an inflection point of the magnetization curve). The crossing point in the magnetization, i.e. the gap between inflection points, can then be related to the energy gap between the $S = 0$ and $S = 1$ states. From the inset in Fig. 6.15 is clear that the level crossings occur at $H = \pm 0.05$ T for *bipy* and at $H = \pm 0.04$ T for *bipyet*. For the other two compounds (*bipytz* and *bdmp*), the magnetic coupling is too small, and no inflection points are visible in the magnetization curves, as evident in the inset plots where we have zoomed in a small field region around zero field. These results are fully consistent with EPR data (reported in [156]), and we can thus conclude that in compounds *bipytz* and *bdmp* the interaction energy of the two rings must be weaker than 100 mK.

Conclusions

The problem of establishing magnetic coupling between single units is very interesting. In this chapter the large family of linked Cr_7Ni rings was experimentally investigated by principally low temperature thermodynamic measurements.

Firstly, the new type of *purple*-Cr_7Ni which constitute the building block of the supramolecular structures was presented. By fitting complementary measurements of susceptibility, magnetization, EPR and specific heat, the spin Hamiltonian parameters were fully characterized.

Systems with more than two linked moieties demonstrate, above all the others, the refined capability achieved in engineering the coordinated structures without perturbing the properties of the single units. In these cases, however, the inter-ring magnetic interaction results weaker and harder to detect.

To have more quantitative information on the inter-ring coupling, a systematic investigation on four *purple*-$(Cr_7Ni)_2$ dimers that differ only for the heteroaromatic linker between the clusters was performed. The study was carried out by means of low temperature specific heat, micro-SQUID magnetization and EPR measurements. For each system the measurements were compared with those of the composing single rings. As result, a different level of conjugation between the rings is found tuned by the linkers. Moreover, from all the experiments, *bipyridyl* results to be the linker that allows the stronger interaction. These results are confirmed by DFT calculations (reported in Appendix B) that, in addition, explains how the spin information can propagate through the heteroaromatic linkers. As result, the crucial factors for an efficient transmission of the interaction are principally two: the length of the linker (the number of bond the spin density has to pass through) and, less intuitive, the shape of heteroaromatic rings constituting the linker. A good shape is the hexagonal one that allows a constructive interaction of the spin density.

From the analysis of *purple*-(Cr_7M)/*green*-(Cr_7M') dimers, *purple*-(Cr_7Ni)/ *green*-(Cr_7Ni) dimer results a very promising linked system. Zero-field specific heat, supported by an effective model, reveals an inter-ring coupling of about 0.15 K, stronger than in the other dimers. This is in agreement with the 'guidelines' previously found by DFT calculations. The linker between the rings is indeed only a pyridine group where spin density can interfere constructively and

passing through a smaller number of bonds than in the *bipyridyl* linker previously analyzed. For this reason, we can expect for these dimer even a stronger magnetic interaction between the rings than in the *bipyridyl* case. Besides and most important, in this case the two molecular units are different, same $S = 1/2$ ground state but with different energy level patterns (so excitable separately). Thus, *purple*-(Cr_7Ni)/*green*-(Cr_7Ni) dimer can be suitable for further experiments to selectively excite the state of only one unit.

Chapter 7

Spin entanglement between two Cr_7Ni molecular clusters

In the previous Chapter *purple*-Cr_7Ni was characterized in detail and identified as our ideal building block with well defined effective $S = 1/2$ spin. The capability of engineering weak magnetic coupling between the rings, preserving the magnetic features of the single units, has been demonstrated. Finally, from the systematic analysis of the magnetic coupling in *purple*-Cr_7Ni dimers, *bipy* linker results the one that can afford the strongest coupling. Here, the attention is focused on the $(Cr_7Ni)_2$-*bipy* derivative, shown in Fig. 7.1, to investigate if quantum entanglement between the molecular rings is established.

The study is divided in two parts. Firstly, in section 7.1, the complete experimental characterization of the dimer compound is presented, reporting the microscopic model and the results of fits that allow to use a two-qubit picture for the system. Then, in section 7.2 the entanglement is experimentally demonstrated by using low temperature susceptibility as entanglement witness. Results are in agreement with the theoretical quantification by means of concurrence calculation, reported in Appendix C.

My contribution to this work concerns the experimental magnetic characterization by means of specific heat. Micro-SQUID magnetization was performed in Grenoble by Dr. Andrea Candini and Dr. Wolfang Wernsdorfer, while EPR spectra were measured in Manchester by Dr. Floriana Tuna. For the theoretical simulations: the spin Hamiltonian diagonalization was made by Dr. Stefano Car-

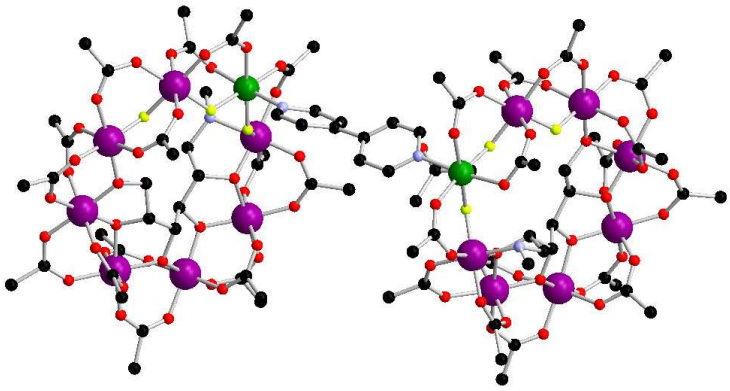

Figure 7.1: Structure of $(Cr_7Ni)_2$-*bipy* as determined by x-ray diffraction. Colors: Cr, purple; Ni, green; F, yellow; O, red; C, black; N, blue. Hydrogens are omitted and pivalate groups are truncated for simplicity.

retta in Parma while the concurrence calculations were carried out by Dr. Filippo Troiani in Modena.

7.1 Magnetic characterization

In section 6.4 of the previous chapter specific heat and low temperature magnetization were reported as qualitative proofs, respectively, of *purple*-Cr_7Ni integrity in dimer compounds and of inter-rings coupling. Here the characterization is deepened and completed giving further exhaustive details and quantitative analysis using a spin-Hamiltonian approach to fit the experimental results.

In Fig. 7.2 the specific heat of $(Cr_7Ni)_2$-bipy is shown for several values of magnetic field. The behavior of all the in-field curves is essentially the same than the curves measured for the single ring (see Fig. 6.3) at the corresponding fields, as seen for 1 T specific heat presented in section 6.4. In the case of zero magnetic field, this is no longer true. As enlightened in Fig. 7.3, for both the single ring and the dimer, a Schottky anomaly around 4 K, due to the energy gap (Δ) between the ground and excited states, is present. Conversely, at low temperature the shape of the curves is different for the two derivatives. For the *purple*-Cr_7Ni, the specific heat goes to zero, while for $(Cr_7Ni)_2$-*bipy* there is an upturn below

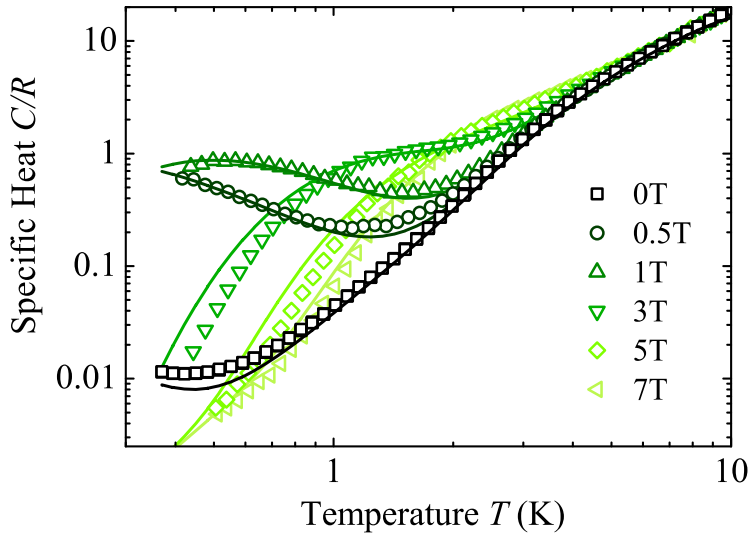

Figure 7.2: Low-temperature specific heat C, normalized to the gas-constant R for $(Cr_7Ni)_2$-*bipy* dimers. Symbols and solid lines correspond to experimental data and theoretical simulations, respectively, for different values of the applied magnetic field.

0.5 K due to the energy splitting of levels (Δ_0) in the ground state multiplet. To have a quantitative analysis, the lattice and magnetic contribution were estimated by fitting $C(T, H)$ for $(Cr_7Ni)_2$-*bipy* at different values of the applied magnetic field H by means of Eqs. (1.14) and (1.17) respectively. The resulting separate contributions are reported in Fig. 7.3. The lattice parameters provided by best fit are the following set of values: $\Theta_D = (153 \pm 10)$ K, $\lambda = (0.59 \pm 0.03)$ K^{-1}.

Low-temperature magnetization measurements M, obtained by micro-SQUID on a single crystal, allow to further characterize the inter-ring interaction. In Figs. 7.4 and 7.5, respectively, the systematic investigations of magnetization loops $M(H)$ of the single *purple*-Cr_7Ni ring and the $(Cr_7Ni)_2$-*bipy* dimer are reported. Measurements were carried out on monocrystalline sample at $T =$ 40 mK and for different sweeping rates, dH/dt. For each derivative, the $M(T, H)$ curves presented in the upper panels show the butterfly behavior, typical of the phonon-bottleneck regime, that becomes clearer as the sweeping rate increases (which allows to keep the temperature of the spin bath even lower than that of the cryostat). Zooming the magnetization curves $M(H)$ (lower panels), it

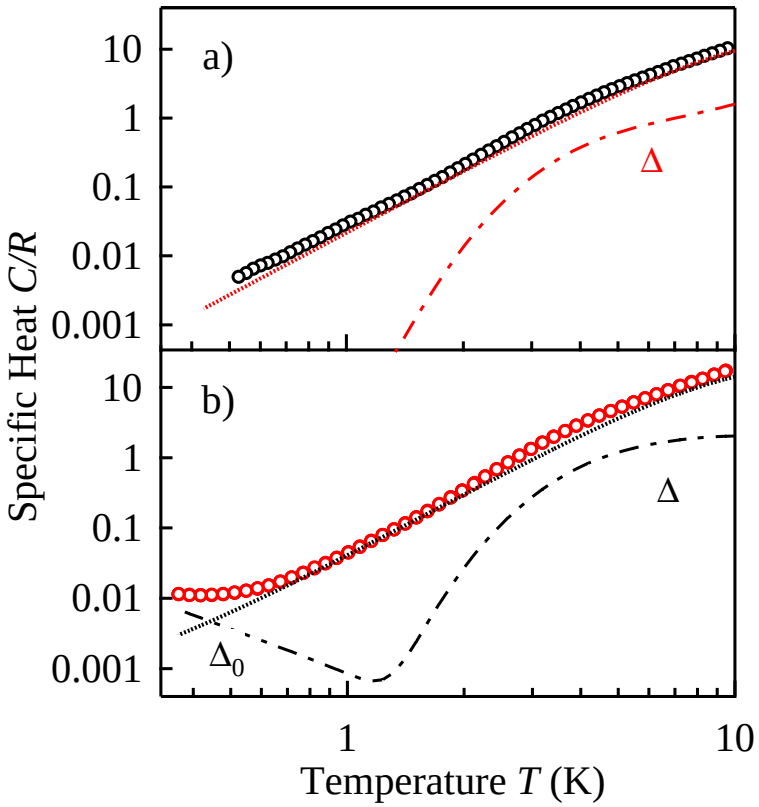

Figure 7.3: Specific heat vs temperature at zero magnetic field for a) single purple-Cr_7Ni ring and b) dimer $(Cr_7Ni)_2$-*bipy*. Theoretical lattice (dotted line) and magnetic (dot-dashed line) contributions are reported. Δ is the main energy splitting between the ground doublet and the first excited quadruplet, while Δ_0 is the energy splitting arising from the inter-rings coupling.

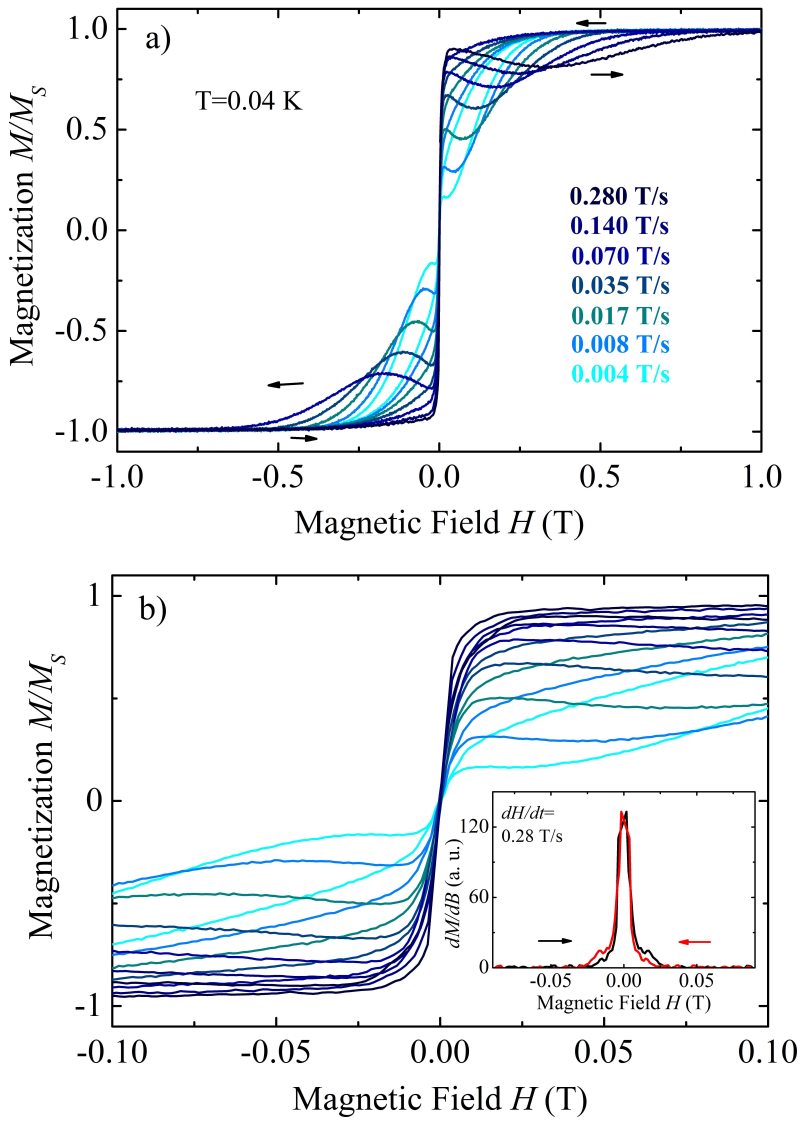

Figure 7.4: Experimental magnetization loops *M(T, H)* of the *purple*-Cr_7Ni. a) Data taken at T=40 mK on single crystal sample for different sweeping rates. b) Magnification of (a). Inset: Derivative of magnetization dM/dH vs H for a sweeping rate $dH/dt = 0.28$ T/s.

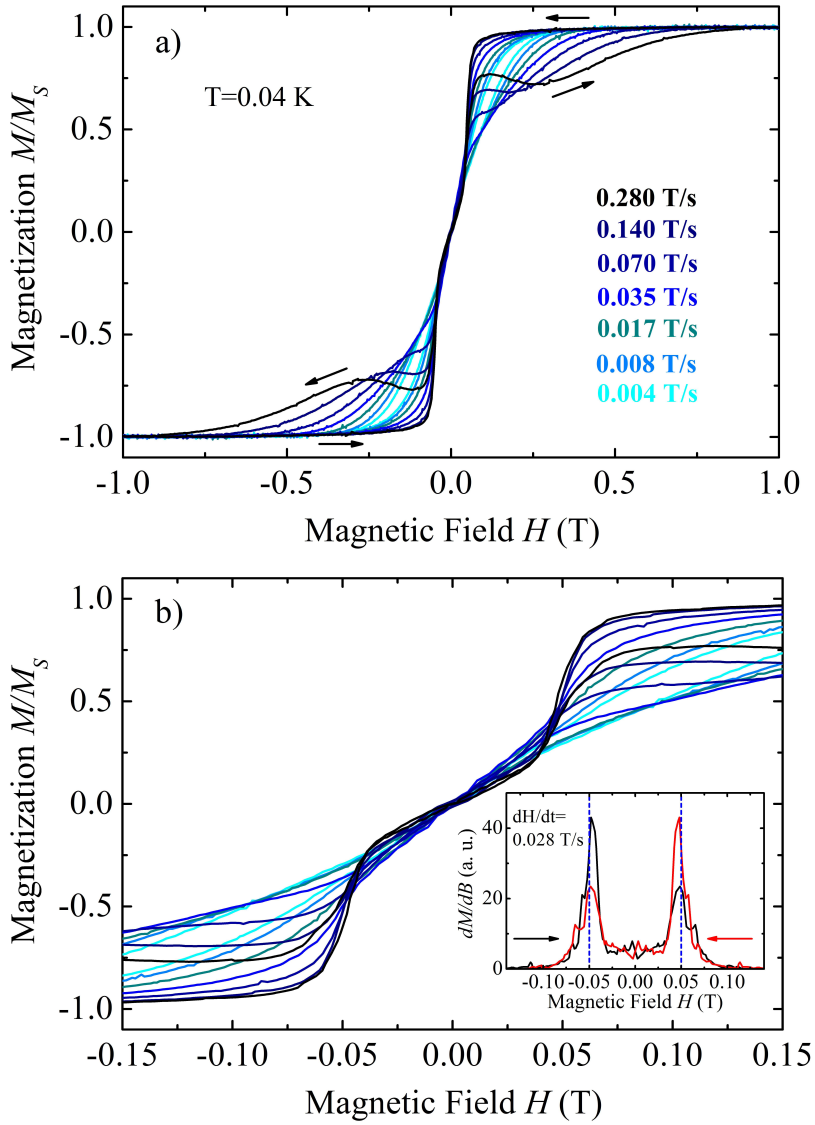

Figure 7.5: Experimental magnetization loops *M(T, H)* taken for $(Cr_7Ni)_2$-*bipy* dimer single crystal sample. a) Data taken at T=40 mK and different sweeping rates of the magnetic field. b) Magnification of (a). Inset: *dM/dH* vs *H* curve taken for *dH/dt*=0.28 T/s.

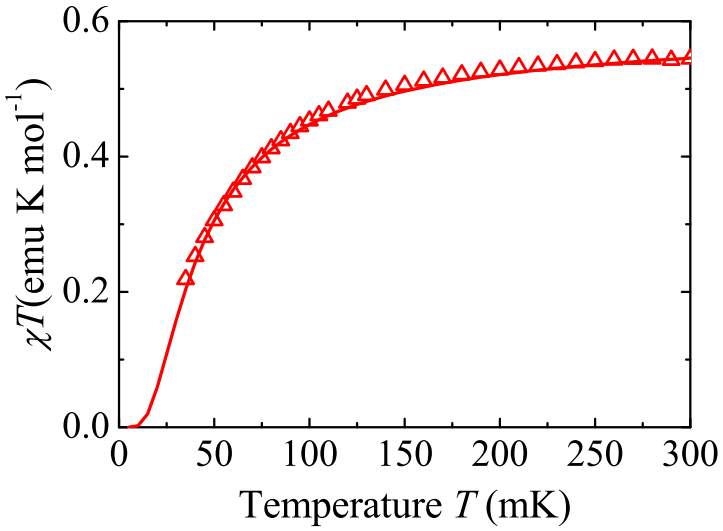

Figure 7.6: dc-susceptibility obtained as derivative of magnetization dM/dH for small value of H and measured at very low sweeping rate $dH/dt = 0.004$ T s^{-1}. Solid line represents the simulation calculated from spin Hamiltonian diagonalization.

is possible to observe that the $(Cr_7Ni)_2$-*bipy* dimer presents additional feeble knees at $H = \pm 0.05$ T. These are clearer in the derivative of magnetization for $dH/dt = 0.28$ T/s, the faster sweeping rate available, as shown in the insets. These knees are not present in the single *purple*-Cr_7Ni ring and they indicate a crossing between low and high spin states of the dimer as H is swept from zero to finite values.

From the magnetization data is possible to obtain the dc susceptibility, defined as $\chi = dM/dH$ for small values of H, and measured with sweeping rates that are small enough to keep the system at the thermal equilibrium with the cryostat ($dH/dt = 0.004$ Ts^{-1}). The susceptibility so obtained is depicted in Fig. 7.6, where the absolute value of χ, reported in emu mol^{-1} K units, was normalized by using as reference high temperature χ measured on powders. The downwards curvature of χT below 0.2 K demonstrates the presence of a weak antiferromagnetic coupling between the two rings.

The inter-ring coupling is confirmed also by Electron Paramagnetic Resonance (EPR) data reported in Fig. 7.7. Additional structures appear in the EPR spec-

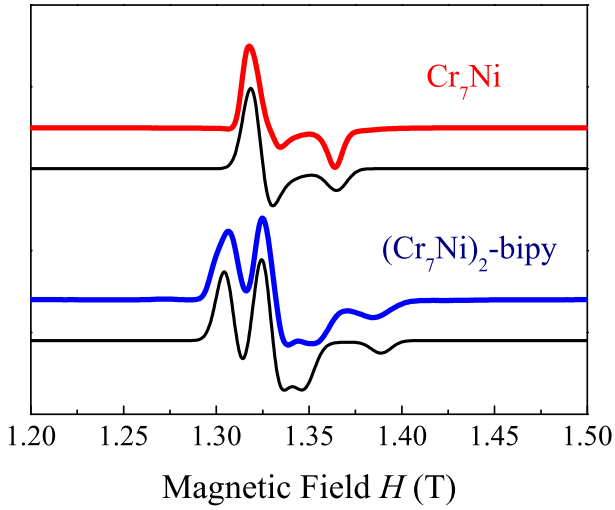

Figure 7.7: Simulated Q-band EPR spectra of purple-Cr_7Ni and $(Cr_7Ni)_2$-*bipy* dimer (solid black lines), obtained within the microscopic spin-Hamiltonian approach (see text). The experimental data (colored lines), taken from [154], have been obtained at T=5 K.

trum of $(Cr_7Ni)_2$-*bipy* dimer with respect to the single ring case, clearly showing interactions between the two molecular rings and mainly involving the ground doublets of the two rings. The microscopic intermolecular coupling between the two rings in the $(Cr_7Ni)_2$-*bipy* dimer can be described by the isotropic Heisenberg term involving the Ni ions

$$\mathcal{H}_{AB} = J' S^A_{Ni} \cdot S^B_{Ni},$$

used also to fit DFT calculations (see Appendix B).

In order to calculate the low-energy (E) properties of the dimer, the coupling Hamiltonian $\mathcal{H}_{AB}$ can be represented on the product basis $|i_A, j_B\rangle$, being $|i_\alpha\rangle$ the single-ring eigenstates of $\mathcal{H}$ in Eq. 6.1. Since $J' \ll J$, the low-E eigenstates are well approximated by truncating the product basis to include only the four lowest-lying multiplets of the rings. The resulting simulations are compared with the experimental results: specific heat (Fig. 7.2), *dc*-susceptibility (Fig. 7.6) and EPR (Fig. 7.7) data of $(Cr_7Ni)_2$-*bipy* are well reproduced by assuming $J'/k_B = 0.16$ K. The sign of J' is fixed by the low-T decrease of the *dc*-susceptibility (Fig. 7.6). At 0.05 T our model also predicts a ground state crossing involving one of the triplet

states (Fig. C.1(b)), in excellent agreement with low-temperature magnetization data (Fig. 7.5).

7.2 Measurement of the entanglement

The quantitative agreement between the microscopic spin-Hamiltonian approach and the whole set of experimental data, based on the use of only four free parameters (J, J', $g_{xx}^{Ni} = g_{yy}^{Ni}$, and g_{zz}^{Ni}), demonstrates a detailed understanding of the intra- and inter-ring interactions and allows the derivation for the dimer of a two-qubit picture. Within such picture, it is possible to discuss the experimental demonstration, through magnetic susceptibility, of entanglement between the two rings, and its theoretical quantification through concurrence. In fact, for $T \ll J/k_B$ [49], each Cr_7Ni ring can be regarded as an effective 1/2 spin, and the effect of intermolecular coupling can be described by projecting $\mathcal{H}_{AB}$ onto the low-energy subspace $\mathcal{S} = \{|i_A, j_B\rangle\}$, with $i_A, j_B = 1, 2$. The resulting effective Hamiltonian, expressed as a function of the total spins of the two rings, reads:

$$\mathcal{H}_0^{eff} = J_{AB}\, \mathbf{S}_A \cdot \mathbf{S}_B + D_{AB}\, (2S_z^A S_z^B - S_x^A S_x^B - S_y^A S_y^B), \tag{7.1}$$

where $J_{AB} \simeq 0.4J'$ and $D_{AB} \simeq 0.1J'$. Here, the second contribution is due to anisotropic crystal-field and intramolecular dipolar interactions. In the presence of a magnetic field, the Hamiltonian of the coupled effective spins $S_A = S_B = 1/2$ thus reads: $\mathcal{H}^{eff} = \mathcal{H}_0^{eff} + \mathcal{H}_1^{eff}$ with $\mathcal{H}_1^{eff} = \mu_B \sum_{\alpha=A,B} \mathbf{H} \cdot \bar{\mathbf{g}} \cdot \mathbf{S}_\alpha$.

For a system of exchange-coupled spins, as discussed in the introductive Chapter (see section 1.2), we can use the absolute value of the magnetic susceptibility, averaged over three orthogonal directions, as entanglement witness [89]. As result, the density matrix ρ of the two effective spins $\mathbf{S}_\alpha$ is non-factorizable if:

$$\sum_\beta \chi_\beta / \bar{g}_\beta^2 < N_A \mu_B^2 / k_B T, \tag{7.2}$$

where $\beta = x', y', z'$ are the three axes and the threshold refers to an Avogadro's number of dimers. Figure 7.8 shows the temperature dependence of the measured (triangles) and simulated (solid lines) dc-susceptibility components for the ring dimer derived by the micro-SQUID magnetization on single crystals and scaled

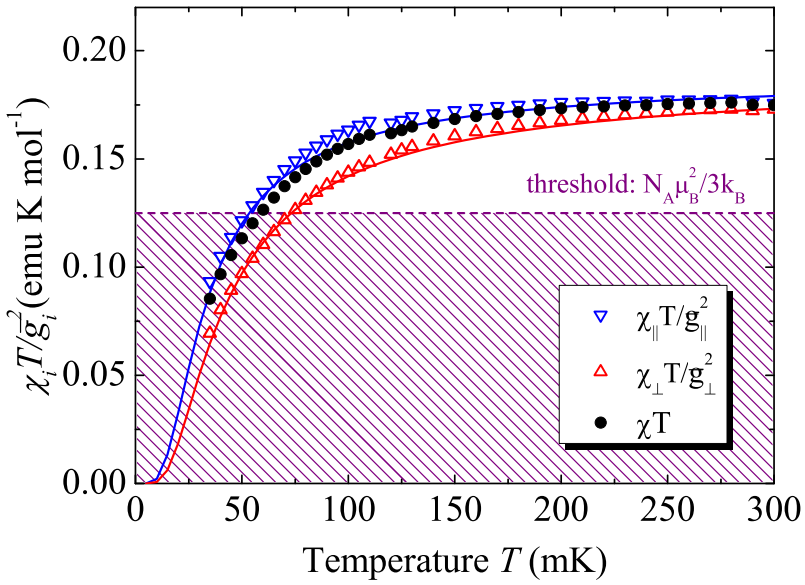

Figure 7.8: dc-susceptibility measured for $(Cr_7Ni)_2$-*bipy* single crystals with magnetic field oriented parallel (blue triangles) and perpendicular (red triangles) to the largest surface of the crystal. Data are scaled to the value of corresponding g-tensor component. (Solid lines) theoretical calculations. Average $(\chi_\perp/\bar{g}_\perp^2+2\chi_\parallel/\bar{g}_\parallel^2)\,T/3$ (black circles) is compared with the threshold for a mole of dimer $N_A\mu_B^2/3k_B$ to find the temperature condition for entanglement (shaded area).

to the squared of the correspondent g tensor component. $\chi_\perp$ (red) is the component perpendicular to the largest surface of the crystal; this direction forms on average an angle of 16° with the z axis, perpendicular to the rings plane. $\chi_\parallel$ refers to the directions parallel to the crystal plane; rotation of magnetic field within this plane does not evidence changes in the magnetic response. The average $(\chi_\perp/\bar{g}_\perp^2+2\chi_\parallel/\bar{g}_\parallel^2)\,T/3$ (circles) is compared with the threshold for a mole of dimers, $N_A\mu_B^2/3k_B$, in order to identify the temperature range where the two rings are entangled (shaded area). As visible from the plot in Fig. 7.8, for $T \lesssim 50$ mK, the inequality 7.2 is fulfilled, thus providing a direct experimental evidence of entanglement between the two Cr_7Ni rings. This result is in agreement with concurrence calculation, reported for completeness in Appendix C, that in addition gives also a quantification of the entanglement and its dependence from magnetic field.

As final consideration, it should be noted that in the present case, the coupling between the effective spins $\mathbf{S}_\alpha$ includes an anisotropic contribution ($D_{AB} \neq 0$), due to which the condition $[\mathcal{H}_0^{eff}, \mathcal{H}_1^{eff}] = 0$ is only fulfilled for $\mathbf{H} \parallel \hat{\mathbf{z}}$. This might in principle result in a difference between the magnetic susceptibility and the entanglement witness [89]. However, for small enough values of D_{AB}/J_{AB}, the difference between the susceptibility and the entanglement witness is negligible with respect to the threshold, as the case presented here (see Fig. 7.9).

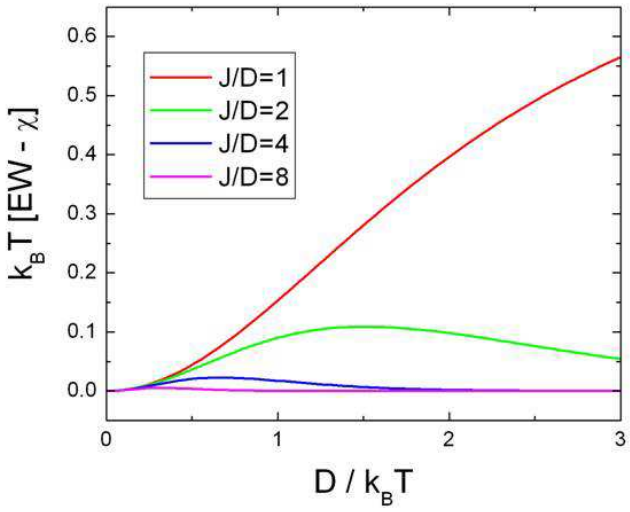

Figure 7.9: Difference between the susceptibility of the two spins with finite D_{AB} and the same quantity with D_{AB}=0. The dimer that is presented here corresponds to the case $J_{AB}/D_{AB} = 4$ (blue curve), where the difference between the susceptibility and the entanglement witness is negligible, with respect to the threshold, which in these units is $\chi_{th} = 1$. The quantities refer to one pair of rings.

Conclusions

In summary, magnetic coupling between molecular cluster in the *purple*-$(Cr_7Ni)_2$-*bipy* dimer was experimentally characterized in detail by heat capacity, micro-SQUID magnetization and EPR. In particular, intra- and inter-ring interactions are modeled through a microscopic spin- Hamiltonian approach that reproduces all the experimental data quantitatively and legitimates the use of an effective two-qubit picture. Moreover, spin entanglement between the rings is experimentally demonstrated using magnetic susceptibility below 50 mK as entanglement witness. Besides, based on a microscopic modelling of the dimer, the ring-ring entanglement was quantified by calculating the concurrence (see Appendix C) and obtaining finite values for an experimentally accessible range of physical parameters.

Part III

General Conclusions

Chapter 8

Conclusions

The aim of this thesis work was to explore different issues of quantum mechanics in several antiferromagnetic molecular spin clusters by using standard thermodynamic measurements and by developing a new experimental setup for Hall micro-probe magnetometry.

Entanglement is an intriguing property of quantum systems that is essential for the implementation of quantum information processing. AF Cr_7Ni spin rings were recognized as possible qubits for quantum computation [49, 54]. Furthermore, promising results were predicted for tripartite system consisting of two Cr_7Ni rings and a Cu ion, for which maximally entangled states can be generated in times much shorter than the expected decoherence time [70]. In this context, important results have been achieved during my thesis work on a new family of linked Cr_7Ni rings (Chapters 6 and 7). Magnetic coupling, although not sufficient, is a crucial prerequisite for the establishment of spin entanglement. In this work its tailoring by supramolecular chemistry was demonstrated. Systematic study of molecular Cr_7Ni dimers with different heteroaromatic linkers has allowed to investigate in-depth how the coupling is tuned by the linkers. Moreover, the mechanism behind the transmission of spin information through the chemical linkers was rationalized by DFT calculations [87, 156]. In the case of one of these dimers, Cr_7Ni-*bipy*, the entanglement between the molecular units was experimentally demonstrated by using the susceptibility as entanglement witness and theoretically quantified by the calculation of concurrence [86]. This is the first, and till now also unique, result of direct measurement of entanglement in finite

molecular spin systems. Finally, it represents a step forward for the realization of quantum computation in molecular qubits.

Another topic treated during my Ph.D. work is the identification of local probes, i.e. experimental techniques that may locally probe the magnetization within a spin systems. This will allow, for instance, to test effects at the edges and eventually to read out information in specific positions of a spin segment. For this purpose, the combination of chemically selective techniques and heteronuclear spin systems can be a good approach. Nuclear magnetic resonance, for instance, has been already used to probe the local spin moment distribution in molecular Cr_7Cd rings [21]. Following this idea, in this thesis work a strategy for probing the local magnetization by means of X-ray Magnetic Circular Dichroism (XMCD) is reported. This is applied to the heterometallic AF Cr_6InNi and Cr_7InNi spin rings (Chapter 4), using the spin of Ni^{2+} as a marker to probe the local magnetization [98]. The results of the magnetic characterization I performed allowed to understand the properties of these systems and to have a comparison with the total magnetic moment obtained from XMCD spectra by using sum rules. Afterwards, the same technique was used also for the heterometallic spin trimer Cr_2Cu (Chapter 5), in this case using the 'extra' Cu ion [99]. The AF Cr_2Cu trimer have an additional advantage with respect to Cr_6InNi and Cr_7InNi rings: the gap energy between its ground state and the first excited is more than 40 K, much lower than the operational temperature for XMCD experiments ($\sim$ 10 K), thus, populating only the ground state, it is easier to interpret the magnetization in terms of moment of spin.

One dimensional infinite chains of Heisenberg interacting spins are textbook examples to study spin waves. An interesting issue is to investigate the effects of the finite size and topology in the spin excitations. Molecular spin clusters offer unique opportunity in this respect, due to the capability to control the length and the spin values of the chain at synthetic level. In Cr_6InNi and Cr_7InNi rings the presence of non magnetic In ion creates a break in the cyclic spin chain within the rings, that makes them good examples of spin segments. The topological and size effects were studied using as comparative system the unbroken Cr_7Ni-piv. Another family suitable for this type of investigation is that of Cr_xCu_2 wheels. The extensive magnetic characterization that has been performed (Chapter 3)

allowed to find the ground states of the systems. It turns out a dependence of the total spin value on the number of Cr ions within the ring, giving different results for the even and the odd membered chains. Finally, these derivatives are proposed for further investigation on local detection of magnetization at the edges of the spin chains and to study spin state transmission along the chains, in order to implement possible application in the field of quantum communication.

For the characterization of static and dynamic properties of molecular spin clusters the countercheck of theory with experimental results is fundamental. One problem to determine the magnetization of molecule with low spin is the requirement of high sensitivity to detect the tiny signals together with the necessity to work at very low temperatures to populate only the ground state. The development of new high-duty experiments is thus very important. Part of my work was dedicated to the development of a new experimental setup for high sensitivity Hall magnetometry measurements combined with resonant absorption of microwaves (Chapter 2). I have successfully produced GaAs/AlGaAs heterostructures Hall probe devices by optical lithography process. Test measurements on Mn_{12} single crystals show the typical steps in the hysteresis loop due to quantum tunneling of magnetization and their shift in presence of resonant absorption of GHz radiation. This demonstrates that both the lithographed devices and the whole setup work. The experiments were performed with a pre-existing setup that can achieve a base temperature of 1.8 K. Afterwards the Hall probe magnetometers were mounted in the new ^{3}He cryostat for which the electrical and detection setup was entirely realized. The operativity of the technique with the new setup has been tested by preliminary measurements on Cr_8Cd at the base temperature of 0.5 K. The work is still in progress and we intend to verify also the functionality in presence of GHz radiation. Finally, we plan to further improve the system implementing it also for magnetization dynamics measurement like electron paramagnetic resonance.

Appendix A

Probing edge magnetization: X-ray Magnetic Circular Dichroism

A.1 Cr_6InNi and Cr_7InNi

The structure of Cr_6InNi and Cr_7InNi, i. e. magnetically broken wheels of chromium with an extra Ni ion at the edge, makes these systems good test-beds to develop an experimental method to read out the magnetic excitations of a finite spin chain (chromium ions) using a local probe (the Ni ion). A powerful technique in this context is the X-ray absorption spectroscopy (XAS) that, thanks to its chemical selectivity, allows to separately investigate local symmetries, electronic configuration, orbital, and spin magnetic moments of the magnetic ions. By means of XAS (here not reported for brevity), we demonstrated in Ref. [98] the equivalence of oxidation states and chemical environment for the Cr^{3+} and Ni^{2+} ions in Cr_6InNi, Cr_7InNi and a similar sample of Cr_7Ni-piv closed ring. In order to discuss the possibility to use the Ni ion as local probe of magnetization, X-Ray Magnetic Circular Dichroism (XMCD) experiments on thick films of the two considered derivatives compared with the results obtained for Cr_7Ni-piv [142] are reported. Measurements were performed by Dr. Valdis Corradini, Dr. Roberto Biagi and Prof. Umberto del Pennino at the ID8 beamline of the European Synchrotron Radiation Facility (ESRF) in Grenoble (France). For further

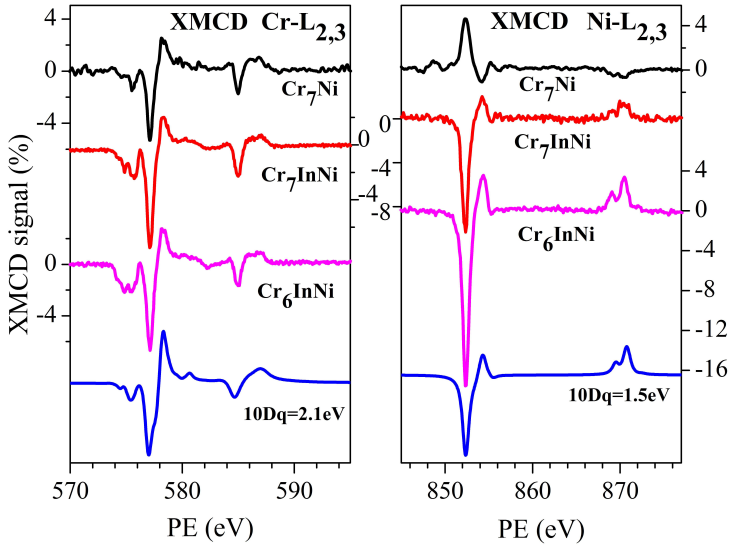

Figure A.1: XMCD spectra taken at the Cr-$L_{2,3}$ (left) and Ni-$L_{2,3}$ (right) edges at the temperature of 10 K and applied field $H = 5$ T, compared with theoretical XMCD (TT multiplet program) calculated for Cr^{3+} and Ni^{2+} in O_h symmetry ($10Dq = 2.1$ eV).

experimental details see Ref. [98] and references therein.

Figure A.1 shows the XMCD spectra taken at Cr (left panel) and Ni (right panel) $L_{2,3}$ edges at $T = 10$ K and with $H = 5$ T external field for the Cr_6InNi, Cr_7InNi, and Cr_7Ni-piv. At bottom of panels calculations of the $L_{2,3}$ edges absorption for the Ni^{2+} and Cr^{3+} using the ligand-field multiplet model implemented by Thole [145, 146] is plotted (where $10Dq$ is a crystal-field parameter). The intensity of dichroic signal provides information on the local magnetic moments while the sign carries information on the nature of the exchange interactions [139, 147]. The intensities of Cr $L_{2,3}$ dichroic signals are comparable for the three specimens and the sign is the same (Fig. A.1). In particular, the negative signal at the Cr L_3 edge and the positive one at the L_2 edge show that, in the range of temperature and field that we have considered, the total Cr magnetic moment points parallel to **H** in each system. Conversely, the dichroic signal taken at the Ni $L_{2,3}$ edges changes significantly (intensity and sign) from case to case. For magnetically broken Cr_6InNi and Cr_7InNi rings, a negative XMCD peak at the L_3 edge and a positive one at the L_2 edge show that the Ni^{2+} magnetic moment is parallel to

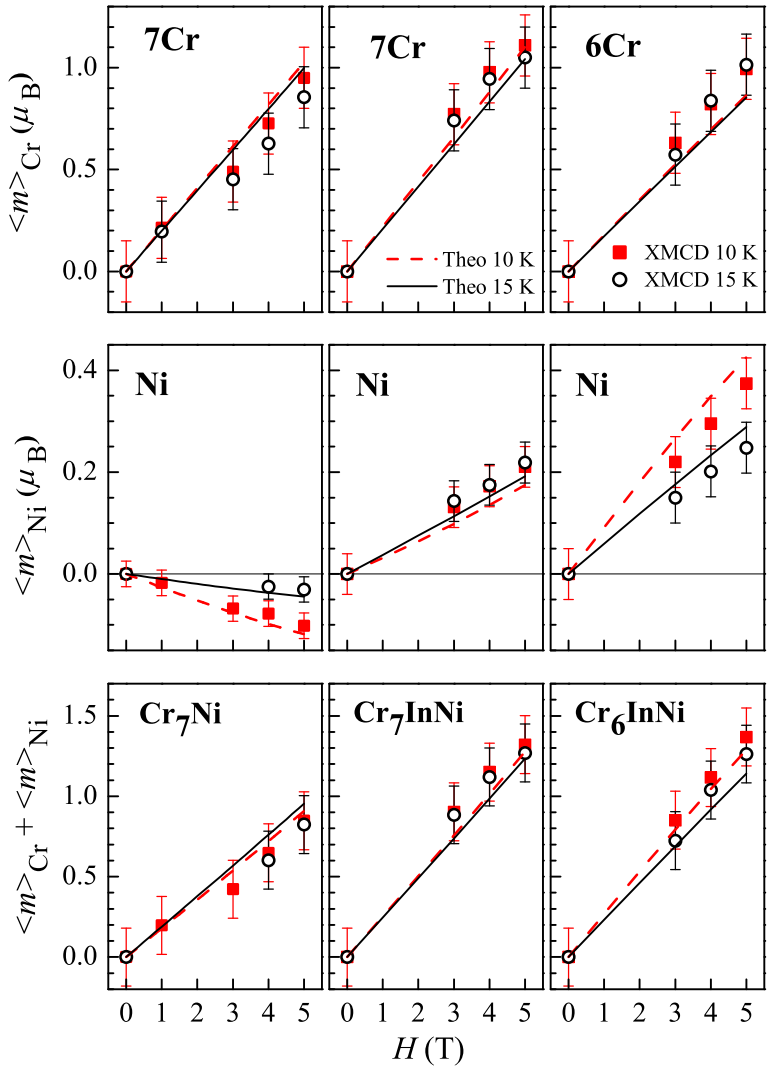

Figure A.2: Magnetic moment-vs-field curves extrapolated from the XMCD spectra. Data related to the same derivative are arranged in columns, where the rows show respectively the partial contribution of chromium, nickel and their sum. Solid lines represent results of theoretical simulations.

H. On the contrary, for cyclic Cr_7Ni-piv rings the magnetic moment of Ni lies antiparallel to **H** [142]. Interpretation is not straightforward since the magnetization of a specific site is determined by the state of the whole spin segment and, at 10 K, different low-lying states are significantly populated (see Fig. 4.5). Yet, the sign of Ni spin is determined by a competition between the Heisenberg antiferromagnetic coupling with the neighbor spins and the Zeeman interaction. In Cr_7Ni-piv closed ring, spins are arranged in a staggered configuration and the magnetization at the Ni site turns out to be opposite to the average magnetization at Cr sites at 10 K [142]. Due to the presence of In^{3+}, which breaks the Heisenberg exchange coupling, we expect that the behavior of the magnetic moment of nickel is dominated by the Zeeman term in both Cr_6InNi and Cr_7InNi, and the sign of magnetization at the Ni site turns out to be the same as the total magnetization of Cr, i.e., parallel to the applied magnetic field. This fact qualitatively proves that Ni is sensitive to the spin arrangement along the ring or segment.

Quantitative information on the Cr^{3+} and Ni^{2+} spin and orbital magnetic moments can be obtained by using the XMCD sum rules [148, 149]. In Fig. A.2 it is shown the mean value of the spin and orbital magnetic moments $< m >=< m_o + m_s >$ vs magnetic field for $T = 10$ and 15 K, calculated from XMCD data by the procedure reported in Ref. [98]. For Cr^{3+} data derived from the dichroic signal reflect the mean value of the magnetic moments over the six or seven sites of the segment, as expected the curves look similar for the three derivatives because the local information is washed out. Conversely, $< m >_{Ni}$, calculated from the dichroic signal of Ni^{2+}, shows remarkable differences from one cluster to another (central panels). According to Fig. A.1, the magnetic moment of Ni has negative slope in cyclic Cr_7Ni-piv rings and positive slope in magnetically Cr_6InNi and Cr_7InNi rings. Furthermore, the bigger size for Cr_6InNi with respect to Cr_7InNi at 10 K shows how the magnetic moment of Ni is sensitive to the topology of the spin segment. The solid lines in Fig. A.2 represent quantitative description derived from the spin-Hamiltonian calculations considering 100 eigenstates, weighted by the Boltzmann factors. The calculated curves, obtained without applying any fitting procedure, are in good agreement with experimental curves derived by XMCD data.

A.2 Cr_2Cu

Here, X-ray absorption spectra (XAS) and X-ray magnetic circular dichroism (XMCD) measurements on thick films (powders) of Cr_2Cu are reported. The experiments were performed at 15 K and with 5 T external magnetic field. Further experimental details can be found in Ref. [99]. The local symmetries of chromium and copper in Cr_2Cu can be obtained by comparing their $L_{2,3}$ XAS and XMCD spectra with those of different known oxides. In particular, in the left panels of Fig. A.3, the Cr $L_{2,3}$ XAS and XMCD spectra are compared with the Cr_2O_3 XAS and the $Cr_{0.07}Al_{1.93}O_3$ XMCD, presenting the same eight similar features in the profile. This is a direct fingerprint of the presence of Cr^{3+} in an O_h environment. Analogously, in the right top panel of Fig. A.3, the Cu $L_{2,3}$ XAS is compared with the CuO signal, showing the same single sharp peak, which indicate the presence of Cu^{2+}. Since CuO compound is not dichroic, for the XMCD signal a direct comparison is instead not possible.

Information on the nature of the intramolecular exchange interactions can be extracted by studying the sign of dichroic signal. Indeed, as an external magnetic field is applied, we expect an interplay between the antiferromagnetic coupling between nearest neighboring ions -favoring a magnetic moment staggered configuration at low temperature- and the Zeeman interaction, tending to align all magnetic moments along the field direction. The Cr_2Cu XMCD spectra, reported in Fig. A.3, provides information on this interplay. The negative dichroic signal at the Cr-L_3 edge and the positive one at the L_2 edge (L_3(-) and L_2(+) in short) implies that the total magnetic moment of Cr ions is parallel to H. This occurs for all the monitored temperatures (T) and external magnetic fields (H). The opposite behavior (i.e. L_3(+), L_2(-)) has been observed for Cu (see Fig. A.3, right bottom panel), implying that the Cu total magnetic moment is antiparallel to Cr at 15 K. Quantitative information on the Cr and Cu spin and orbital magnetic moments can be obtained by using XMCD sum rules [148, 149]. The upper and central panels of Fig. A.4 display the separate contributions of Cr and Cu to the total magnetic moment of the Cr_2Cu, determined by the sum rules, as a function of $\mu_B H$ at 15 and 25 K. For chromium ion the calculation is carried out with (open symbols) and without (filled symbols) considering the dipolar term T_z (see Ref. [99] for the details). Results are in good agreement with the

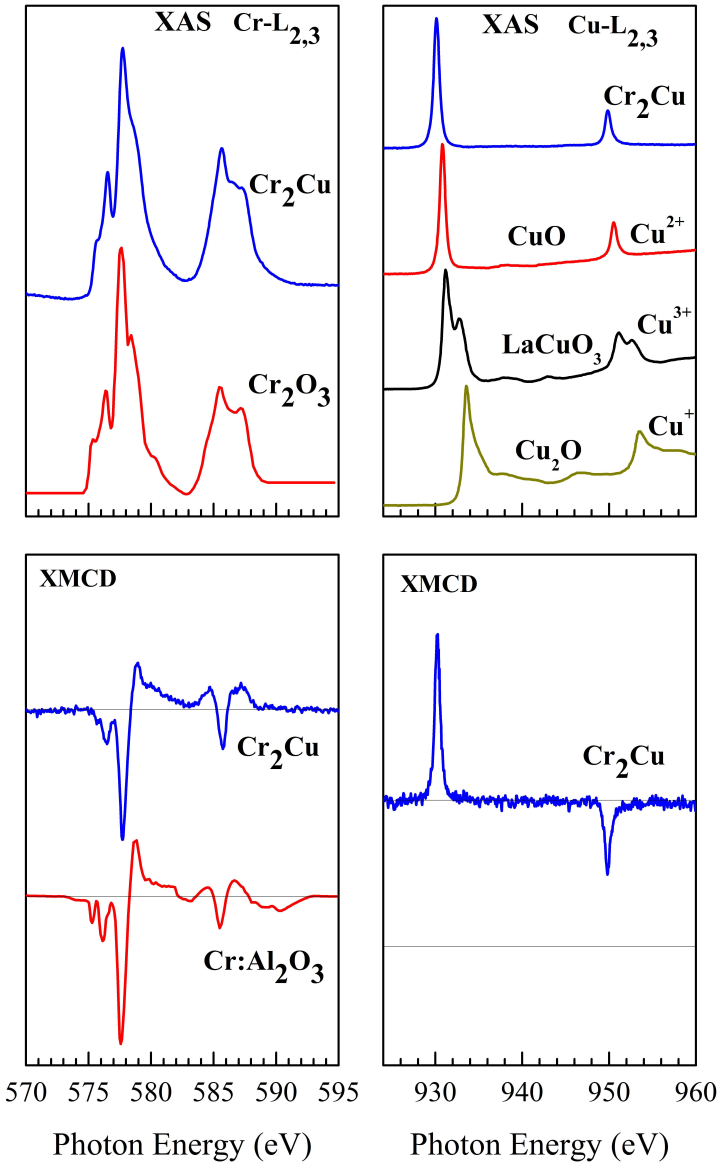

Figure A.3: (Left panels) The Cr $L_{2,3}$ XAS and XMCD spectra for Cr_2Cu, taken at 15 K and 5 T, compared with those of Cr_2O_3 [151]. (Right panels) The Cu $L_{2,3}$ XAS and XMCD spectra for Cr_2Cu compared with those of Cu_2O [152], CuO [152] and $LaCuO_3$ [153].

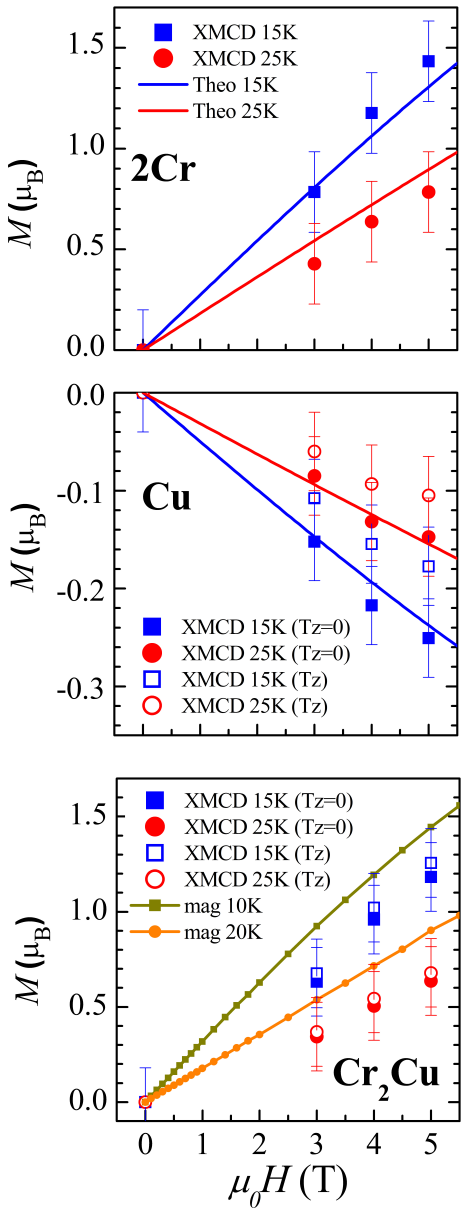

Figure A.4: Magnetic moment vs field curves extrapolated from the XMCD spectra of Cr_2Cu at 15 and 25 K. The panels from the top to the bottom show respectively the partial contribution of chromium, copper and their sum. For copper the results which include Tz (open symbols) can be compared with the results without Tz (filled symbols). Solid lines represent the spin-Hamiltonian calculations, while lines and symbols in the lower panel are the bulk magnetization measured on polycrystalline sample at 10 and 20 K of Fig. 5.7.

spin-Hamiltonian calculations (continuous lines). Finally, in the bottom panel the Cr_2Cu total magnetic moments derived by the sum rules are compared with bulk like magnetization of Fig. 5.7.

Appendix B

Propagation of spin information: Density Functional Theory calculations

In order to deepen the understanding on the mechanism behind magnetic interactions through heteroaromatic bridges in *purple*-$(Cr_7Ni)_2$ dimers and account for the observed experimental behavior, density-functional theory (DFT) analysis on these systems are reported. Calculations were performed by Dr. Valerio Bellini by means of the NWChem quantum chemistry package [157] and by taking into account the full systems (rings+bridge), for further details see Ref. [156].

In Figure B.1 the spin-polarized electron density iso-surfaces for a very low iso-value (= ± 0.0005 electrons/a.u.^{3}) is plotted and zoomed onto the relevant Ni-linker-Ni coupling region. Looking at Fig. B.1, in all the linkers, following the bond paths, we can observe an alternation of spin polarization when moving from one atom to the next. Moreover, from the shape of the isosurfaces it is possible to deduce that this polarization involves primarily orbitals with π character. Polarization of σ orbitals in the linkers, although present on the N atoms bound to Ni, fades away within few bonds, and vanishes altogether for inner C atoms.

In the case of *bipy* dimer (see Fig. B.1(a)), the spin density from the Ni site splits and propagates along the two branches of the hexagonal group following the spin alternation rule. At the C atom that closes the hexagon of the *pyridine* there is constructive interference thank to the equal paths that the spin density

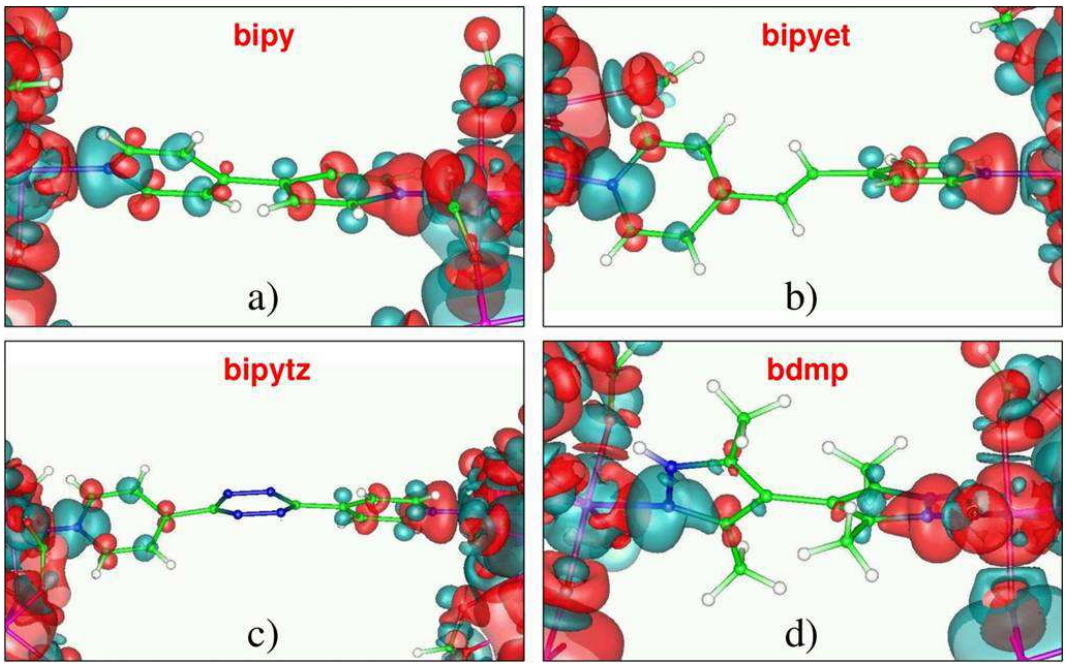

Figure B.1: Spin polarization density plots for: a) *bipyridyl*, b) *bipyridylethene*, c) *bipyridyltetrazine* and d) *bidimethylpyrazolyl*, for isovalues of + (cyan) and − (red) 0.0005 electrons/a.u.^{3}

has passed through. Thus, the spin information in the *bipy* dimer can achieve the inner part of the link and the magnetic interaction between the rings is appreciable.

For the *bipyet* and *bipytz* linkers, see Figs. B.1(b) and (c) respectively, that are based on hexagonal groups too, it enters into play the larger number of bonds that such interaction should travel through. Delocalization of π system orbitals becomes less and less efficient as the number of bonds increases, so that only a small fraction of spin-polarization survives in the two facing C atoms in the center of the linkers (π spin polarization interaction becomes visible only for isovalues 5 times smaller than the one used in Fig. B.1, i.e. $= 0.0001$ electrons/a.u.^{3}).

Finally, in the case of the *bdmp* linker, depicted in Fig. B.1(d), moving from the Ni atoms to the inner C atoms, there are two different possible paths on the two sides of the five-membered rings, through N–C or through N–N–C, composed respectively by two and three bonds. Because of the spin alternation rule, spin frustration is present in the inner C atoms, and destructive interference between the two paths leads to a very low spin-polarization of the orbitals in the inner region of the *bdmp*, despite the fact that the two Ni centers are closer to each other (see the Ni-Ni distances reported in Fig. 6.13).

Spin-density analysis is in good agreement with EPR [156] and the micro-SQUID magnetization experiments, supporting that among the linkers analyzed (sketched in Fig. 6.13) inter-ring magnetic interaction is largest via the *bipyridyl* linker. In order to provide further support, total energy calculations of projected broken-symmetry Ising spin configurations were performed, and mapped onto the microscopic spin Hamiltonian:

$$\mathcal{H}_{\mathcal{AB}} = J' S^A_{Ni} \cdot S^B_{Ni} \tag{B.1}$$

where J' is the isotropic exchange between the Ni spin moments, and S^A_{Ni} and S^B_{Ni} are the spin moments of the two Ni ions ($S^A_{Ni} = S^B_{Ni} = 1$) of the two rings labeled A and B. J' is then given by 1/4 of the total energy difference between the singlet and triplet states of the Cr_7Ni_2 dimer, and positive values are relative to a preferred antiferromagnetic coupling between the rings, i.e. a singlet spin ground state. The calculated J' values are 10, 0.5, 4 and 2 μeV for *bipy*, *bipyet*, *bipytz* and *bdmp* respectively. Exchange interaction is therefore found to be largest in *bipyridyl*-linked dimers, in agreement with the experimental observations. Moreover, I

anticipate that the complete spin Hamiltonian approach, reported in the next chapter, will give an exchange constant $J' = 0.16$ K; much greater than the value found by DFT. We also note that the coupling in compound *bipyet* is predicted to be much less than the one of compound *bipy*, while experimentally these values are rather close to each other. These, however, are tiny interactions, which are near the numerical precision of the DFT method.

Appendix C

Entanglement quantification: Concurrence calculation

A quantitative, though indirect, estimate of entanglement is provided by the concurrence ($\mathcal{C}$) [72], whose value ranges from 0 for factorizable states to 1 for maximally entangled ones. The equilibrium density matrix of the dimer ρ_{eq}^{AB}, in the case $\mathbf{H} \parallel \hat{\mathbf{z}}$, is a statistical mixture of the eigenstates $|S, M\rangle$, each weighted by its Boltzmann factor $P_{S,M}$. The resulting expression for the concurrence is $\mathcal{C}(\rho_{eq}^{AB}) = \max\{\, |P_{1,0} - P_{0,0}| - 2(P_{1,1}\, P_{1,-1})^{1/2}\,,\, 0\,\}$, if $\max\{P_{1,0}, P_{0,0}\} > (P_{1,1}\, P_{1,-1})^{1/2}$, and $\mathcal{C}(\rho_{eq}^{AB}) = 0$ otherwise. In the range where the concurrence is finite, its dependence on T and on the physical parameters in $\mathcal{H}^{eff}$ is given by the following expression:

$$\mathcal{C}(\rho_{eq}^{AB}) = \frac{1 - e^{-\frac{J_{AB}}{k_B T}} \left(e^{\frac{D_{AB}}{k_B T}} + 2e^{-\frac{D_{AB}}{2k_B T}} \right)}{1 + e^{-\frac{J_{AB}}{k_B T}} \left[e^{\frac{D_{AB}}{k_B T}} + 2e^{-\frac{D_{AB}}{2k_B T}} \cosh\left(\frac{\bar{g}_{zz}\mu_B B}{k_B T} \right) \right]}.$$

The resulting concurrence is plotted in Fig. C.1(a) as function of temperature and magnetic field. For $H = 0$, the dimer is maximally (hardly) entangled if the temperature is much smaller than (comparable to) the singlet-triplet splitting $E_{1,0} - E_{0,0} = J_{AB} - D_{AB}$. The transition from entangled to factorizable states corresponds to $T \simeq 50$ mK, in agreement with that estimated through the entanglement witness. At vanishing temperature, the concurrence undergoes an abrupt transition from $\mathcal{C} = 1$ to $\mathcal{C} = 0$ as the value of the magnetic

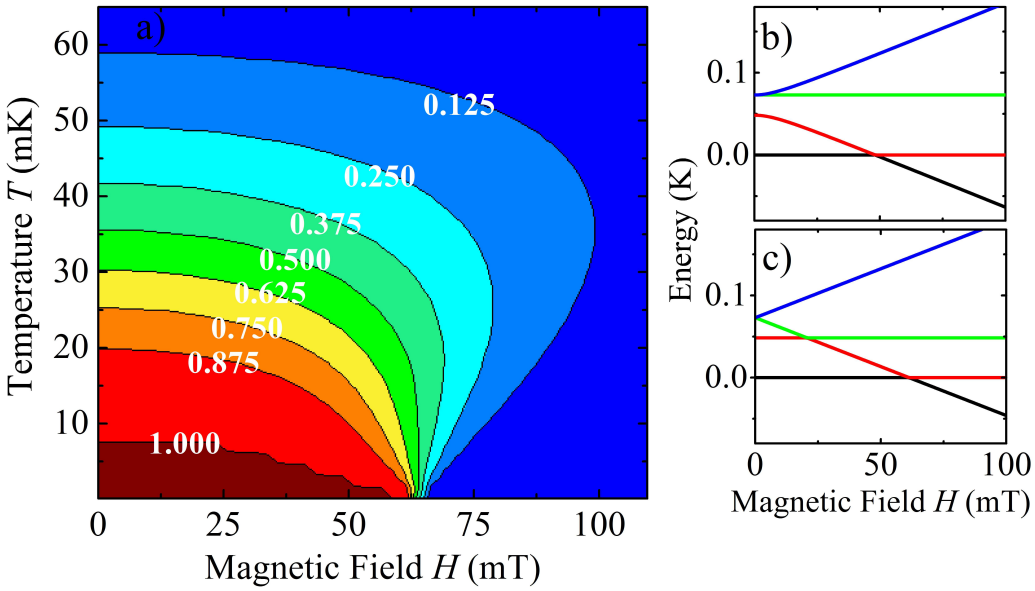

Figure C.1: (a) Concurrence of the $(Cr_7Ni)_2$ dimer at equilibrium at temperature T in the presence of an external magnetic field H (along z). Panels in the right-hand side show the low-energy spectrum of the dimer, derived from the microscopic spin Hamiltonian, for $\mathbf{H} \parallel \hat{\mathbf{x}}$ (b) and $\mathbf{H} \parallel \hat{\mathbf{z}}$(c)

field exceeds $H_c = (J_{AB} + D_{AB}/2)/\mu_B \bar{g}_{zz}$, where, a crossing takes place between $|S = 0, M = 0\rangle$ and $|S = 1, M = 1\rangle$ [Fig. C.1(c)]. Altogether, the two rings are entangled in the temperature range $\bar{g}_{zz}\mu_B(H - H_c) \lesssim k_B T \lesssim J_{AB} - D_{AB}$, that includes experimental conditions reported in the manuscript.

Bibliography

[1] Eugenio Coronado and Carlos J. Gomez-Garcia. Polyoxometalate-based molecular materials. *Chemical Reviews*, 98(1):273–296, 1998. PMID: 11851506.

[2] Achim Muller, Frank Peters, Michael T. Pope, and Dante Gatteschi. Polyoxometalates: Very large clustersnanoscale magnets. *Chemical Reviews*, 98(1):239–272, 1998. PMID: 11851505.

[3] J. Lehmann, A. Gaita-Ario, Coronado E., and D. Loss. Spin qubits with electrically gated polyoxometalate molecules. *Nature Nanotechnology*, 2:312, 2007.

[4] T. C. Kobayashi, M. Takiguchi, C. U. Hong, K. Amaya, A. Kajiwara, A. Harada, and M. Kamachi. Magnetic phase transition of organic radical magnets. *Journal of Magnetism and Magnetic Materials*, 140-144(Part 2):1447 – 1448, 1995. International Conference on Magnetism.

[5] Cyrille Train, Lucie Norel, and Martin Baumgarten. Organic radicals, a promising route towards original molecule-based magnetic materials. *Coordination Chemistry Reviews*, 253(19-20):2342 – 2351, 2009. Deutsche Forschungsgemeinschaft Molecular Magnetism Research Report.

[6] T. Lis. *Acta Crystallographica Section B*, 36:2042, 1980.

[7] A. Caneschi, D. Gatteschi, R. Sessoli, A.L. Barra, L.C. Brunel, and M. Guillot. Alternating current susceptibility, high field magnetization, and millimeter band EPR evidence for a ground $S = 10$ state in $[Mn_{12}O_{12}(Ch_3COO)_{16}(H_2O)_4]_2CH_3COOH_4H_2O$. *Journal of the American Chemical Society*, 113:5873–5874, 1991.

[8] Jonathan R. Friedman, M. P. Sarachik, J. Tejada, and R. Ziolo. Macroscopic Measurement of Resonant Magnetization Tunneling in High-Spin Molecules. *Phys. Rev. Lett.*, 76(20):3830–3833, May 1996.

[9] R. Sessoli, D. Gatteschi, A. Caneschi, and M. A. Novak. Magnetic bistability in a metal-ion cluster. *Nature (London)*, 365:141, 1993.

[10] L. Thomas, F. Lionti, R. Ballou, D. Gatteschi, R. Sessoli, and B. Barbara. Macroscopic quantum tunnelling of magnetization in a single crystal of nanomagnets. *Nature*, 383:145, 1996.

[11] Luc Thomas and Bernard Barbara. Quantum Tunneling of the Magnetization In Mn_{12}-Ac. *Journal of Low Temperature Physics*, 113:1055–1060, 1998. 10.1023/A:1022516703754.

[12] D. Gatteschi and R. Sessoli. Quantum Tunneling of Magnetization and Related Phe- nomena in Molecular Materials. *Angewandte Chemie International Edition*, page 268, 2003.

[13] C. Sangregorio, T. Ohm, C. Paulsen, R. Sessoli, and D. Gatteschi. Quantum Tunneling of the Magnetization in an Iron Cluster Nanomagnet. *Phys. Rev. Lett.*, 78(24):4645–4648, Jun 1997.

[14] W. Wersdorfer and R. Sessoli. Quantum Phase Interference and Parity Effects in Magnetic Molecular Clusters. *Science*, 284:133, 1999.

[15] F. Luis, F. L. Mettes, J. Tejada, D. Gatteschi, and L. J. de Jongh. Observation of quantum coherence in mesoscopic molecular magnets. *Phys. Rev. Lett.*, 85(20):4377–4380, Nov 2000.

[16] G. L. Abbati, A. Caneschi, A. Cornia, A. C. Fabretti, D. Gatteschi, W. Malavasi, and L. Schenetti. Modulated Magnetic Coupling in Alkoxoiron(III) Rings by Host-Guest Interactions with Alkali Metal Cations. *Inorg. Chem.*, 36:6443, 1997.

[17] M. Affronte, J. C. Lasjaunias, A. Cornia, and A. Caneschi. Low-temperature specific heat of fe_6 and fe_{10} molecular magnets. *Phys. Rev. B*, 60(2):1161–1166, Jul 1999.

[18] Kingsley L. Taft, Christopher D. Delfs, Georgia C. Papaefthymiou, Simon Foner, Dante Gatteschi, and Stephen J. Lippard. $[Fe(OMe)_2(O_2CCH_2Cl)]_{10}$, a Molecular Ferric Wheel. *Journal of the American Chemical Society*, 116(3):823–832, 1994.

[19] G. L. Abbati, A. Caneschi, A. Cornia, A. C. Fabretti, and D. Gatteschi. $[Fe(OCH_3)_2(dbm)]_{12}$: synthesis, solid-state characterization and reactivity of a new molecular ferric wheel. *Inorg. Chim. Acta*, 297:291, 1999.

[20] S. P. Watton, P. Fuhrmann, L. E. Pence, A. Caneschi, A. Cornia, G. L. Abbati, and S. J. Lippard. *Angew. Chem. Int. Ed.*, 36:2774, 1997.

[21] E. Micotti, Y. Furukawa, K. Kumagai, S. Carretta, A. Lascialfari, F. Borsa, G. A. Timco, and R. E. P. Winpenny. Local spin moment distribution in antiferromagnetic molecular rings probed by NMR. *Phys. Rev. Lett.*, 97(26):267204, Dec 2006.

[22] F. Borsa, A. Lascialfari, and Y. Furukawa. NMR in magnetic molecular rings and clusters. *New developments in Magnetic Resonance*, 2006.

[23] S. Carretta, J. van Slageren, T. Guidi, E. Liviotti, C. Mondelli, D. Rovai, A. Cornia, A. L. Dearden, F. Carsughi, M. Affronte, C. D. Frost, R. E. P. Winpenny, D. Gatteschi, G. Amoretti, and R. Caciuffo. Microscopic spin hamiltonian of a Cr_8 antiferromagnetic ring from inelastic neutron scattering. *Phys. Rev. B*, 67(9):094405, Mar 2003.

[24] D.M. Low, G. Rajaraman, M. Helliwell, G. Timco, J. van Slageren, R. Sessoli, S. T. Ochsenbein, R. Bircher, C. Dobe, O. Waldmann, H. U. Güdel, M. A. Adams, E. Ruiz, S. Alvarez, and E. J. L. McInnes. *Chem.-Eur. J.*, 12:1385, 2005.

[25] R. H. Laye, M. Murrie, S. Ochsenbein, A. R. Bell, S. J. Teat, J. Raftery, H. U. Güdel, and E. J. L. McInnes. *Chem. -Eur. J.*, 9:6215, 2003.

[26] Olivier Kahn. *Molecular Magnetism*. Wiley-VCH, 1993.

[27] J Schnack. Effects of frustration on magnetic molecules: a survey from Olivier Kahn until today. *Dalton Trans.*, 39:4677, 2010.

[28] O. Kahn. Competing spin interactions and degenerate frustration for discrete molecular species. *Chem. Phys. Lett.*, 265:109, 1997.

[29] B. Cage, F. A. Cotton, N. S. Dalal, E. A. Hillard, Rakvin B., and C. M. Ramsey. Observation of Symmetry Lowering and Electron Localization in the Doublet-States of a Spin-Frustrated Equilateral Triangular Lattice: $Cu_3(O_2C_{16}H_{23})\cdot 1.2C_6H_{12}$. *J. Am. Chem. Soc.*, 125:5270, 2003.

[30] G. Chaboussant, R. Basler, A. Sieber, S. T. Ochsenbein, A. Desmedt, R. E. Lechner, M. T. F. Telling, P. Kgerler, Mller A., and H.-U. Gdel. Low-energy spin excitations in the molecular magnetic cluster V_{15}. *Europhys. Lett.*, 59:291, 2002.

[31] S. Ferrer, F. Lloret, I. Bertomeu, G. Alzuet, J. Borras, S. Garca-Granda, Liu-Gonzlez M., and J. Haasnoot. Cyclic Trinuclear and Chain of Cyclic Trinuclear Copper(II) Complexes Containing a Pyramidal $Cu_3O(H)$ Core. Crystal Structures and Magnetic Properties of $[Cu_3(\mu_3\text{-}OH)(aaat)_3(H_2O)_3](NO_3)_2H_2O$ [aaat = 3-Acetylamino-5-amino-1,2,4-triazolate] and $[Cu_3(\mu_3\text{-}OH)(aat)_3(\mu_3\text{-}SO_4)]6H_2O_n$ [aat = 3-Acetylamino-1,2,4-triazolate]: New Cases of Spin-Frustrated Systems. *Inorg. Chem.*, 41:5821, 2002.

[32] G. Chaboussant, S. T. Ochsenbein, A. Sieber, H.-U. Gdel, H. Mutka, Mller A., and B. Barbara. Mechanism of ground-state selection in the frustrated molecular spin cluster V_{15}. *Europhys. Lett.*, 66:423, 2004.

[33] I. Rousochatzakis, Y. Ajiro, H. Mitamura, P. Kögerler, and M. Luban. Hysteresis Loops and Adiabatic Landau-Zener-Stückelberg Transitions in the Magnetic Molecule V_6. *Phys. Rev. Lett.*, 94(14):147204, Apr 2005.

[34] T. Yamase, E. Ishikawa, K. Fukaya, H. Nojiri, T. Taniguchi, and T. Atake. Spin-Frustrated $(VO)_3^{6+}$-Triangle-Sandwiching Octadecatungstates as a New Class of Molecular Magnets. *Inorg. Chem.*, 43:8150, 2004.

[35] Kwang-Yong Choi, Yasuhiro H. Matsuda, Hiroyuki Nojiri, U. Kortz, F. Hussain, Ashley C. Stowe, Chris Ramsey, and Naresh S. Dalal. Observation of a Half Step Magnetization in the Cu_3-Type Triangular Spin Ring. *Phys. Rev. Lett.*, 96(10):107202, Mar 2006.

[36] L.-L. Wang, Y.-M. Sun, Z.-Y. Yu, Qi Z.-N., and C.-B. Liu. Theoretical Investigation on Triagonal Symmetry Copper Trimers: Magneto-Structural Correlation and Spin Frustration. *J. Phys. Chem. A.*, 113:10534, 2009.

[37] G. H. Wannier. Antiferromagnetism. the triangular ising net. *Phys. Rev.*, 79(2):357–364, Jul 1950.

[38] R. M. F. Houtappel. *Physica (Amsterdam)*, 16:425, 1950.

[39] M. F. Collins and O. A. Petrenko. Triangular antiferromagnets. *Can. J. Phys.*, 75:605, 1997.

[40] H. Kawamura. Universality of phase transitions of frustrated antiferromagnets. *J. Phys. Condens. Matter*, 10:4707, 1998.

[41] R. Moessner and S. L. Sondhi. Ising models of quantum frustration. *Phys. Rev. B*, 63(22):224401, May 2001.

[42] R. Moessner and S. L. Sondhi. Slow holes in the triangular ising antiferromagnet. *Phys. Rev. B*, 62(21):14122–14130, Dec 2000.

[43] Cannon R. D. and R. P. White. Chemical and physical properties of triangular bridged metal complexes. *Progress in Inorganic Chemistry*, 36, 1988.

[44] S. Carretta, P. Santini, G. Amoretti, F. Troiani, and M. Affronte. Spin triangles as optimal units for molecule-based quantum gates. *Phys. Rev. B*, 76(2):024408, Jul 2007.

[45] Filippo Troiani, Marco Affronte, Stefano Carretta, Paolo Santini, and Giuseppe Amoretti. Proposal for quantum gates in permanently coupled antiferromagnetic spin rings without need of local fields. *Phys. Rev. Lett.*, 94(19):190501, May 2005.

[46] Mircea Trif, Filippo Troiani, Dimitrije Stepanenko, and Daniel Loss. Spin-electric coupling in molecular magnets. *Phys. Rev. Lett.*, 101(21):217201, Nov 2008.

[47] F. K. Larsen, E. J. L. McInnes, H. E. Mkami, J. Overgaard, S. Piligkos, G. Rajaraman, E. Rentschler, A. A. Smith, G. M. Smith, V. Boote, M. Jennings, G. A. Timco, and R. E. P. Winpenny. Synthesis and characterization of heterometallic Cr_7M wheels. *Angewandte Chemie International Edition*, 42:101, 2003.

[48] M. Affronte, F. Troiani, A. Ghirri, S. Carretta, P. Santini, V. Corradini, R. Schuecker, C. Muryn, G. Timco, and R.E.P. Winpenny. Molecular routes for spin cluster qubits. *Dalton Trans.*, pages 2810–2817, 2006.

[49] F. Troiani, A. Ghirri, M. Affronte, S. Carretta, P. Santini, G. Amoretti, S. Piligkos, G. Timco, and R. E. P. Winpenny. Molecular engineering of antiferromagnetic rings for quantum computation. *Phys. Rev. Lett.*, 94(20):207208, May 2005.

[50] R. Caciuffo, T. Guidi, G. Amoretti, S. Carretta, E. Liviotti, P. Santini, C. Mondelli, G. Timco, C. A. Muryn, and R. E. P. Winpenny. Spin dynamics of heterometallic Cr_7M wheels (M=Mn, Zn, Ni) probed by inelastic neutron scattering. *Phys. Rev. B*, 71(17):174407, May 2005.

[51] W. Wernsdorfer, D. Mailly, G. A. Timco, and R. E. P. Winpenny. Resonant photon absorption and hole burning in Cr_7Ni antiferromagnetic rings. *Phys. Rev. B*, 72(6):060409, Aug 2005.

[52] S. Carretta, P. Santini, G. Amoretti, M. Affronte, A. Ghirri, I. Sheikin, S. Piligkos, G. Timco, and R. E. P. Winpenny. Topology and spin dynamics in magnetic molecules. *Phys. Rev. B*, 72(6):060403, Aug 2005.

[53] M. Affronte, F. Troiani, A. Ghirri, A. Candini, V. Evangelisti, M. Corradini, S. Carretta, P. Santini, G. Amoretti, F. Tuna, G. Timco, and R. E. P. Winpenny. Single molecule magnets for quantum computation. *J. Phys. D: Appl. Phys.*, 40:2999, 2007.

[54] Arzhang Ardavan, Olivier Rival, John J. L. Morton, Stephen J. Blundell, Alexei M. Tyryshkin, Grigore A. Timco, and Richard E. P. Winpenny. Will spin-relaxation times in molecular magnets permit quantum information processing? *Phys. Rev. Lett.*, 98(5):057201, Jan 2007.

[55] F. Troiani, V. Bellini, and M. Affronte. Decoherence induced by hyperfine interactions with nuclear spins in antiferromagnetic molecular rings. *Phys. Rev. B*, 77(5):054428, Feb 2008.

[56] Valdis Corradini, Alberto Ghirri, Umberto del Pennino, Roberto Biagi, Victoria A. Milway, Grigore Timco, Floriana Tuna, Richard E. P. Winpenny, and Marco Affronte. Grafting molecular Cr_7Ni rings on a gold surface. *Dalton Trans.*, 39:4928, 2010.

[57] A. Ghirri, V. Corradini, C. Cervetti, A. Candini, U. del Pennino, G. Timco, R.J. Pritchard, C.A. Muryn, R.E.P. Winpenny, and M. Affronte. Deposition of functionalized Cr_7Ni molecular rings on graphite by liquid phase. *Advanced Functional Materials*, 2010.

[58] V. Corradini, F. Moro, R. Biagi, V. De Renzi, U. del Pennino, V. Bellini, S. Carretta, P. Santini, V. A. Milway, G. Timco, R. E. P. Winpenny, and M. Affronte. Successful grafting of isolated molecular Cr_7Ni rings on Au(111) surface. *Phys. Rev. B*, 79(14):144419, Apr 2009.

[59] Valdis Corradini, Roberto Biagi, Umberto del Pennino, Valentina De Renzi, Alessandro Gambardella, Marco Affronte, Christopher A. Muryn, Grigore A.

Timco, and Richard E. P. Winpenny. Isolated Heterometallic Cr_7Ni Rings Grafted on Au(111) Surface. *Inorg. Chem.*, 46:4937, 2007.

[60] Stephen Blundell. *Magnetism in Condensed Matter*. Oxford University Press, 2001.

[61] J. Schnack and Marshall Luban. Rotational modes in molecular magnets with antiferromagnetic heisenberg exchange. *Phys. Rev. B*, 63(1):014418, Dec 2000.

[62] O. Waldmann. Spin dynamics of finite antiferromagnetic heisenberg spin rings. *Phys. Rev. B*, 65(2):024424, Dec 2001.

[63] O. Waldmann, T. Guidi, S. Carretta, C. Mondelli, and A. L. Dearden. Elementary excitations in the cyclic molecular nanomagnet Cr_8. *Phys. Rev. Lett.*, 91(23):237202, Dec 2003.

[64] E. Liviotti, S. Carretta, and G. Amoretti. S-mixing contributions to the high-order anisotropy terms in the effective spin hamiltonian for magnetic clusters. *J. Chem. Phys*, 117:3361, 2002.

[65] David N. Hendrickson, George Christou, Edward A. Schmitt, Eduardo Libby, John S. Bashkin, Sheyi Wang, Hui Lien Tsai, John B. Vincent, and Peter D. W. Boyd. Photosynthetic water oxidation center: spin frustration in distorted cubane MnIVMnIII3 model complexes. *J. Am. Chem. Soc*, 114:2455, 1992.

[66] Wolfgang Wernsdorfer, Nria Aliaga-Alcalde, David N. Hendrickson, and George Christou. Exchange-biased quantum tunnelling in a supramolecular dimer of single-molecule magnets. *Nature*, 416:406, 2002.

[67] E. C. Sanudo, T. Cauchy, E. Ruiz, R. H. Laye, O. Roubeau, S. J. Teat, and G. Aromì. Molecules composed of two weakly magnetically coupled $[Mn_4^{III}]$ clusters. *Inorg. Chem.*, 46:9045, 2007.

[68] H. Miyasaka, K. Nakata, K.-I. Sugiura, M. Yamashita, and R. Clerac. A three-dimensional ferrimagnet composed of mixed-valence Mn_4 clusters linked by an $Mn[N(CN)_2]_{64}$- unit. *Angew. Chem.*, 116:725, 2004.

[69] M. Affronte, I. Casson, M. Evangelisti, A. Candini, S. Carretta, C. A. Muryn, S. J. Teat, G. A. Timco, W. Wernsdorfer, and R. E. P. Winpenny. Magnetothermal properties of molecule-based materials. *Angew. Chem. Int. Ed.*, 44:6496, 2005.

[70] Grigore A. Timco, Stefano Carretta, Filippo Troiani, Floriana Tuna, Robin J. Pritchard, Christopher A. Muryn, Eric J. L. McInnes, Alberto Ghirri, Andrea Candini, Paolo Santini, Giuseppe Amoretti, Marco Affronte, and Richard E. P. Winpenny. Engineering the coupling between molecular spin qubits by coordination chemistry. *Nature Nanotechnology*, 4(3):173–178, 2009.

[71] Ryszard Horodecki, PawełHorodecki, MichałHorodecki, and Karol Horodecki. Quantum entanglement. *Review of modern Physics*, 81:865, 2009.

[72] Luigi Amico, Rosario Fazio, Andreas Osterloh, and Vlatko Vedral. Entanglement in many-body systems. *Rev. Mod. Phys.*, 80(2):517–576, May 2008.

[73] M. A. Nielsen and I. L. Chuang. *Quantum Computation and Quantum Information*, volume 10. Cambridge: Cambridge University Press, 2000.

[74] Dik Bouwmeester, Jian-Wei Pan, Matthew Daniell, Harald Weinfurter, and Anton Zeilinger. Observation of three-photon greenberger-horne-zeilinger entanglement. *Phys. Rev. Lett.*, 82(7):1345–1349, Feb 1999.

[75] J. R. Petta, A. C. Johnson, J. M. Taylor, E. A. Laird, A. Yacoby, M. D. Lukin, C. M. Marcus, M. P. Hanson, and A. C. Gossard. Coherent Manipulation of Coupled Electron Spins in Semiconductor Quantum Dots. *Science*, 309:2180, 2005.

[76] Tommaso Roscilde, Paola Verrucchi, Andrea Fubini, Stephan Haas, and Valerio Tognetti. Studying quantum spin systems through entanglement estimators. *Phys. Rev. Lett.*, 93(16):167203, Oct 2004.

[77] Tommaso Roscilde, Paola Verrucchi, Andrea Fubini, Stephan Haas, and Valerio Tognetti. Entanglement and factorized ground states in two-dimensional quantum antiferromagnets. *Phys. Rev. Lett.*, 94(14):147208, Apr 2005.

[78] A. Fubini, T. Roscilde, V. Tognetti, M. Tusa, and P. Verrucchi. Reading entanglement in terms of spin configurations in quantum magnets. *Eur. Phys. J. D*, 38:563570, 2006.

[79] M. C. Arnesen, S. Bose, and V. Vedral. Natural thermal and magnetic entanglement in the 1d heisenberg model. *Phys. Rev. Lett.*, 87(1):017901, Jun 2001.

[80] A. Osterloh, Luigi Amico, G. Falci, and Rosario Fazio. Scaling of entanglement close to a quantum phase transition. *Nature*, 416:608, 2002.

[81] Tobias J. Osborne and Michael A. Nielsen. Entanglement in a simple quantum phase transition. *Phys. Rev. A*, 66(3):032110, Sep 2002.

[82] G. Vidal, J. I. Latorre, E. Rico, and A. Kitaev. Entanglement in quantum critical phenomena. *Phys. Rev. Lett.*, 90(22):227902, Jun 2003.

[83] F. Verstraete, M. Popp, and J. I. Cirac. Entanglement versus correlations in spin systems. *Phys. Rev. Lett.*, 92(2):027901, Jan 2004.

[84] S. Ghosh, T. F. Rosenbaum, G. Aeppli, and S. N. Coppersmith. Entangled quantum state of magnetic dipoles. *Nature*, 425:48, 2003.

[85] A. M. Souza, M. S. Reis, D. O. Soares-Pinto, I. S. Oliveira, and R. S. Sarthour. Experimental determination of thermal entanglement in spin clusters using magnetic susceptibility measurements. *Phys. Rev. B*, 77(10):104402, Mar 2008.

[86] A. Candini, G. Lorusso, F. Troiani, A. Ghirri, S. Carretta, P. Santini, G. Amoretti, C. Muryn, F. Tuna, G. Timco, E. J. L. McInnes, R. E. P. Winpenny, W. Wernsdorfer, and M. Affronte. Entanglement in supramolecular spin systems of two weakly coupled antiferromagnetic rings (*purple*-Cr_7Ni). *Phys. Rev. Lett.*, 104(3):037203, Jan 2010.

[87] F. Troiani, V. Bellini, A. Candini, G. Lorusso, and M. Affronte. Spin entanglement in supramolecular structures. *Nanotechnology*, 21:274009, 2010.

[88] Fernando G. S. L. Brandão. Quantifying entanglement with witness operators. *Phys. Rev. A*, 72(2):022310, Aug 2005.

[89] M. Wieśniak, V. Vedral, and Č. Brukner. Magnetic susceptibility as a macroscopic entanglement witness. *New journal of Physics*, page 258, 2005.

[90] Sougato Bose. Quantum Communication through an Unmodulated Spin Chain. *Phys. Rev. Lett.*, 91(20):207901, Nov 2003.

[91] S. Bose. Quantum communication through spin chain dynamics: an introductory overview. *Cont. Phys.*, 48:13, 2007.

[92] S. Bose, B.-Q. Jin, and V. E. Korepin. Quantum communication through a spin ring with twisted boundary conditions. *Phys. Rev. A*, 72(2):022345, Aug 2005.

[93] P. Gambardella, A. Dallmeyer, K. Maiti, M.C. Malagoli, W. Eberhardt, K. Kern, and C. Carbone. Ferromagnetism in one-dimensional monatomic metal chains. *Nature*, 416:301–304, 2002.

[94] P. Gambardella. Magnetic nanostructures: Quantum chains with a spin. *Nature Materials*, 5:431–432, 2006.

[95] Cyrus F. Hirjibehedin, Christopher P. Lutz, and Andreas J. Heinrich. Spin coupling in engineered atomic structures. *Science*, 312(5776):1021–1024, 2006.

[96] A. Ghirri, A. Candini, M. Evangelisti, M. Affronte, S. Carretta, P. Santini, G. Amoretti, R. S. G. Davies, G. Timco, and R. E. P. Winpenny. Elementary excitations in antiferromagnetic heisenberg spin segments. *Phys. Rev. B*, 76(21):214405, Dec 2007.

[97] F. Troiani and M. Affronte. Molecular Spins for Quantum Information Technologies. *submitted*, 2010.

[98] A. Ghirri, G. Lorusso, F. Moro, F. Troiani, V. Corradini, C. Muryn, F. Tuna, G. Timco, R. E. P. Winpenny, and M. Affronte. Probing edge magnetization in antiferromagnetic spin segments. *Phys. Rev. B*, 79(22):224430, Jun 2009.

[99] G. Lorusso, V. Corradini, A. Candini, A. Ghirri, R. Biagi, U. del Pennino, S. Carretta, E. Garlatti, P. Santini, G. Amoretti, G. Timco, R. G. Pritchard, R. E. P. Winpenny, and M. Affronte. Probing local magnetization in molecular heterometallic Cr_2Cu trimer. *Phys. Rev. B*, 82(14):144420, Oct 2010.

[100] Neil W. Ashcroft and N. David Mermin. *Solid State Physics*. Saunders college (Fort Worth, Philadelphia), 1976.

[101] Charles Kittel. *Introduction to Solid State Physics*. Wiley and Sons (New York), 1986.

[102] A. J. Dekker. *Solid State Physics*. Macmillan & Co.(London), 1952.

[103] Richard L. Carlin. *Magnetochemistry*. Springer-Verlag, 1986.

[104] E. S. R. Gopal. *Specific Heats at Low Temperatures*. Plenum (New York), 1966.

[105] D. Gatteschi, R. Sessoli, and J. Villain. *Molecular Nanomagnets*. Oxford University Press, 2006.

[106] M. Affronte, J. C. Lasjaunias, and A. Cornia. Low temperature specific heat of molecular rings: a study on the effects of the internal guest substitution and on the lattice contribution. *Eur. Phys. J.*, 15:633, 2000.

[107] M. Evangelisti, F. Luis, L. J. de Jong, and M. Affronte. Magnetothermal properties of molecule-based materials. *J. Mat. Chem.*, 16:2534, 2006.

[108] B. Bleany and K. D. Bowers. Anomalous Paramagnetism of Copper Acetate. *Proc. R. Soc. Lond. A*, 214:451, 1952.

[109] A. H. Morrish. *The physical principle of magnetism.* Wiley (New York), 1965.

[110] R. Bachmann, F. J. DiSalvo, T. H. Gebale, R. L. Greene, R. E. Howard, C. N. King, H. C. Kirsch, K. N. Lee, R. E. Schwall, H. U. Thomas, and R. B. Zubeck. Heat Capacity measurements on Small Samples at Low Temperatures. *The Review of Scientific Instruments*, 43:205, 1972.

[111] Quantum Design. *PPMS Hardware and Option Manual.* San Diego, CA, U.S.A. See also http://www.qdusa.com/products/ppms.html.

[112] J. S. Hwang, K. J. Lin, and C. Tien. Measurement of heat capacity by fitting the whole temperature response of a heat-pulse calorimeter. *The Review of Scientific Instruments*, 68, 1997.

[113] J. P. Shepherd. Analysis of the lumped τ_2 effect in relaxation calorimetry. *The Review of Scientific Instruments*, 56, 1985.

[114] R. S. Popovic. *Hall Effect Devices.* Adam Hilger (Bristol), 1991.

[115] Xin-Qi Li, F.M. Peeters, and A.K. Geim. The Hall effect of an inhomogeneous magnetic field in mesoscopic structures. *Journal of Physics: Condensed Matter*, 9:8065– 8073, 1997.

[116] K. S. Novoselov, S. V. Morozov, S. V. Dubonos, M. Missous, A. O. Volkov, D. A. Christian, and A. K. Geim. Submicron probes for Hall magnetometry in the extended temperature range from helium to room temperature. *Journal of Applied Physics*, 93:10053–10057, 2003.

[117] S. Liu, H. Guillou, A. D. Kent, G.W. Stupian, and M.S. Leung. Effect of probe gempetry on the Hall response in an inhomogeneous magnetic field: a numerical study. *Journal of Applied Physics*, 83:6161–6165, 1998.

[118] G. Boero, M. Demierre, P.-A. Besse, and R.S. Popovic. Micro Hall devices: perfor- mance, technologies and application. *Sensors and Actuators A*, 106:314–320, 2003.

[119] A. D. Kent, S. von Molnár, S. Gider, and D. D. Awshalom. Properties and measurement of scanning tunneling microscope fabricated ferromagnetic particle arrays. *Journal of Applied Physics*, 76:6656, 1994.

[120] A. K. Geim, S. V. Dubonos, J. G. S. Lok, I. V. Grigorieva, J. C. Maan, L. Theil Hansen, and P. E. Liendolof. Ballistic Hall micromagnetometry. *Applied Physics Letters*, 71:2379, 1997.

[121] Louisa Bokacheva, Andrew D. Kent, and Marc A. Walters. Crossover between Thermally Assisted and Pure Quantum Tunneling in Molecular Magnet Mn_{12}-Acetate. *Phys. Rev. Lett.*, 85(22):4803–4806, Nov 2000.

[122] Kulicke and Soffa Industries, INC. *Model 4123 Universal Wedge Bonder Operation Manual.*

[123] Andrea Candini. *Ph.D Thesis.* Università di Modena e Reggio Emilia, 2006.

[124] A. Candini. Magnetometry by means of Hall micro-probes in the Quantum Design PPMS.

[125] W. Wernsdorfer, A. Müller, D. Mailly, and B. Barbara. Resonant photon absorption in the low-spin molecule V_{15}. *Europhysics Letters*, 66:861, 2004.

[126] K. Petukhov, W. Wernsdorfer, A.-L. Barra, and V. Mosser. Resonant photon absorption in fe_8 single-molecule magnets detected via magnetization measurements. *Phys. Rev. B*, 72(5):052401, Aug 2005.

[127] W. Wernsdorfer, D. Mailly, G. A. Timco, and R. E. P. Winpenny. Resonant photon absorption and hole burning in cr_7ni antiferromagnetic rings. *Phys. Rev. B*, 72(6):060409, Aug 2005.

[128] S. Bahr, K. Petukhov, V. Mosser, and W. Wernsdorfer. Pump-Probe Experiments on the Single-Molecule Magnet Fe_8: Measurement of Excited Level Lifetimes. *Phys. Rev. Lett.*, 99(14):147205, Oct 2007.

[129] K. Petukhov, S. Bahr, W. Wernsdorfer, A.-L. Barra, and V. Mosser. Magnetization dynamics in the single-molecule magnet fe_8 under pulsed microwave irradiation. *Phys. Rev. B*, 75(6):064408, Feb 2007.

[130] E. del Barco, A. D. Kent, E. C. Yang, and D. N. Hendrickson. Quantum Superposition of High Spin States in the Single Molecule Magnet Ni_4. *Phys. Rev. Lett.*, 93(15):157202, Oct 2004.

[131] Louisa Bokacheva, Andrew D. Kent, and Marc A. Walters. Crossover between Thermally Assisted and Pure Quantum Tunneling in Molecular Magnet Mn_{12}-Acetate. *Phys. Rev. Lett.*, 85(22):4803–4806, Nov 2000.

[132] R. Amigó, J. M. Hernandez, A. García-Santiago, and J. Tejada. Microwave absorption and magnetization tunneling in mn_{12}-acetate molecular clusters. *Phys. Rev. B*, 67(22):220402, Jun 2003.

[133] Oxford Instruments. *Operator's handbook*. See also http://www.oxford-instruments.com.

[134] Yuji Furukawa, Kazuki Kiuchi, Ken-ichi Kumagai, Yoshitami Ajiro, Yasuo Narumi, Masahiro Iwaki, Koichi Kindo, Alberto Bianchi, Stefano Carretta, Grigore A. Timco, and Richard E. P. Winpenny. Topological effects on the magnetic properties of closed and open ring-shaped Cr-based antiferromagnetic nanomagnets. *Phys. Rev. B*, 78(9):092402, Sep 2008.

[135] L. P. Engelhardt, C. A. Muryn, R. G. Pritchard, G. A. Timco, Tuna F., and R. E. P. Winpenny. Octa-, Deca-, Trideca- and Tetradeca-nuclear Heterometallic Cyclic Chromium-Copper Cages. *Angew. Chem.*, 120:938, 2008.

[136] S. L. Heath, R. H. Laye, C. A. Muryn, N. Lima, R. Sessoli, R. Shaw, S. J. Teat, G. A. Timco, and R. E. P. Winpenny. Templating Open- and Closed-Chain Structures around Metal Complexes of Macrocycles. *Angewandte Chemie International Edition*, 43:61326135, 2004.

[137] Larry Engelhardt, Catalin Martin, Ruslan Prozorov, Marshall Luban, Grigore A. Timco, and Richard E. P. Winpenny. High-field magnetic properties of the magnetic molecule $Cr_{10}Cu_2$. *Phys. Rev. B*, 79(1):014404, Jan 2009.

[138] R. Boča. *Theoretical Foundations of Molecular Magnetism*. Elsevier, Amsterdam, 1999.

[139] E. Dujardin, S. Ferlay, X. Phan, C. Desplanches, C. Cartier dit Moulin, P. Sainctavit, F. Baudelet, E. Dartyge, P. Veillet, and M. Verdaguer. Synthesis and Magnetization of New Room-Temperature Molecule-Based Magnets: Effect of

Stoichiometry on Local Magnetic Structure by X-ray Magnetic Circular Dichroism. *J. Am. Chem. Soc.*, 120:11347, 1998.

[140] M.-A. Arrio, A. Scuiller, P. Sainctavit, C. Cartier dit Moulin, T. Mallah, and M. Verdaguer. Soft X-ray Magnetic Circular Dichroism in Paramagnetic Systems: Element-Specific Magnetization of Two Heptanuclear Cr^{III} M_6^{II} High-Spin Molecules. *J. Am. Chem. Soc.*, 121:6414, 1999.

[141] R. Moroni, Ch. Cartier dit Moulin, G. Champion, M.-A. Arrio, Ph. Sainctavit, M. Verdaguer, and D. Gatteschi. X-ray magnetic circular dichroism investigation of magnetic contributions from Mn(III) and Mn(IV) ions in Mn_{12}-ac. *Phys. Rev. B*, 68(6):064407, Aug 2003.

[142] V. Corradini, F. Moro, R. Biagi, U. del Pennino, V. De Renzi, S. Carretta, P. Santini, M. Affronte, J. C. Cezar, G. Timco, and R. E. P. Winpenny. X-ray magnetic circular dichroism investigation of spin and orbital moments in Cr_8 and Cr_7Ni antiferromagnetic rings. *Phys. Rev. B*, 77(1):014402, Jan 2008.

[143] R. S. G. Davies, D. Collison, P. A. Mason, C. A. Muryn, E. C. Sanũdo, R. Sessoli, M. Shanmugam, G. A. Timco, F. Tuna, and R. E. P. Winpenny. *unpublished.*

[144] V. Bellini, A. Olivieri, and F. Manghi. Density-functional study of the Cr_8 antiferromagnetic ring. *Phys. Rev. B*, 73(18):184431, May 2006.

[145] B. T. Thole, G. van der Laan, J. C. Fuggle, G. A. Sawatzky, R. C. Karnatak, and J.-M. Esteva. 3d x-ray-absorption lines and the $3d^9 4f^{n+1}$ multiplets of the lanthanides. *Phys. Rev. B*, 32(8):5107–5118, Oct 1985.

[146] B. T. Thole, G. van der Laan, and P. H. Butler. Spin-mixed ground state of Fe phthalocyanine and the temperature-dependent branching ratio in X-ray absorption spectroscopy. *Chem. Phys. Lett.*, 149:295, 1988.

[147] G. Champion, N. Lalioti, V. Tangoulis, M.-A. Arrio, P. Sainctavit, F. Villain, A. Caneschi, D. Gatteschi, C. Giorgetti, F. Baudelet, M. Verdaguer, and C. Cartier dit Moulin. XMCD for Monitoring Exchange Interactions. The Role of the Gd 4f and 5d Orbitals in Metal-Nitronyl Nitroxide Magnetic Chains. *J. Am. Chem. Soc.*, 125:8371, 2003.

[148] Paolo Carra, B. T. Thole, Massimo Altarelli, and Xindong Wang. X-ray circular dichroism and local magnetic fields. *Phys. Rev. Lett.*, 70(5):694–697, Feb 1993.

[149] B. T. Thole, P. Carra, F. Sette, and G. van der Laan. X-ray circular dichroism as a probe of orbital magnetization. *Phys. Rev. Lett.*, 68(12):1943–1946, Mar 1992.

[150] G. A. Timko, A. K. Ursu, M. D. Mazus, V. X. Kravtsov, and V. K. Rotaru. Synthesis, properties and structure of (*3-oxo)-hexabenzoatotriaminetrichromium(III) perchlorate. *Russian Journal of Coordination Chemistry*, 21:463–468, 1995.

[151] E. Gaudry, P. Sainctavit, F. Juillot, F. Bondioli, P. Ohresser, and I. Letard. From the green color of eskolaite to the red color of ruby: an X-ray absorption spectroscopy study . *Phys. Chem. Miner.*, 32:710, 2006.

[152] M. Finazzi, G. Ghiringhelli, O. Tjernberg, Ph. Ohresser, and N. B. Brookes. Radiationless Raman versus Auger behavior at the Cu L_3 resonance of CuO and Cu_2O. *Phys. Rev. B*, 61(7):4629–4635, Feb 2000.

[153] T. Mizokawa, A. Fujimori, H. Namatame, Y. Takeda, and M. Takano. Electronic structure of tetragonal $LaCuO_3$ studied by photoemission and x-ray-absorption spectroscopy. *Phys. Rev. B*, 57(16):9550–9556, Apr 1998.

[154] G. A. Timco, E. J. L. McInnes, R. G. Pritchard, F. Tuna, and R. E. P. Winpenny. Heterometallic rings made from chromium stick together easily. *Angewandte Chemie International Edition*, 47(50):9681–9684, 2008.

[155] Stergios Piligkos, Høgni Weihe, Eckhard Bill, Frank Neese, Hassane El Mkami, Graham M. Smith, David Collison, Gopalan Rajaraman, Grigore A. Timco, Richard E. P. Winpenny, and Eric J. L. McInnes. EPR Spectroscopy of a Family of $Cr_7^{III}M^{II}$(M = Cd, Zn, Mn, Ni) Wheels: Studies of Isostructural Compounds with Different Spin Ground States. *Chemistry A European Journal*, 15:3152, 2009.

[156] Grigore A. Timco, Valerio Bellini, Giulia Lorusso, Andrea Candini, Thomas Faust, Floriana Tuna, Wolfgang Wernsdorferd, Marco Affronte, and Richard E. P. Winpenny. Propagation of spin information at supra-molecular scale through hetero-aromatic linkers. *submitted*, ?:?, 2010.

[157] E. J. Bylaska, W. A. de Jong, N. Govind, K. Kowalski, T. P. Straatsma, M. Valiev, E. D. Wang, Apra, T. L. Windus, J. Hammond, P. Nichols, S. Hirata, M. T. Hackler, Y. Zhao, P.-D. Fan, R. J. Harrison, M. Dupuis, D. M. A. Smith,

J. Nieplocha, V. Tipparaju, M. Krishnan, Q. Wu, T. Van Voorhis, A. A. Auer, M. Nooijen, E. Brown, G. Cisneros, G. I. Fann, H. Fruchtl, J. Garza, K. Hirao, R. Kendall, J. A. Nichols, K. Tsemekhman, K. Wolinski, J. Anchell, D. Bernholdt, P. Borowski, T. Clark, D. Clerc, H. Dachsel, M. Deegan, K. Dyall, D. Elwood, E. Glendening, M. Gutowski, A. Hess, J. Jaffe, B. Johnson, J. Ju, R. Kobayashi, R. Kutteh, Z. Lin, R. Littlefield, X. Long, B. Meng, T. Nakajima, S. Niu, L. Pollack, M. Rosing, G. Sandrone, M. Stave, H. Taylor, G. Thomas, J. van Lenthe, A. Wong, and Z. Zhang. *NWChem, A Computational Chemistry Package for Parallel Computers, Version 5.1*, 2007.

Curriculum vitae

Giulia Lorusso

Birth (date/place): November 15th 1983, Perugia, Italy

Nationality: Italian

Professional address: Dipartimento di Fisica, Università di Modena e Reggio Emilia and S3 CNR-Istituto Nanoscienze, Via Campi 213/a, 41100 Modena, Italy

Phone number: +39 059 2055678

E-mail: giulia.lorusso@unimore.it

Studies and qualification:

January 2008-today: Ph.D. student at Università di Modena e Reggio Emilia and S3 CNR-Istituto Nanoscienze, Modena, Italy. Thesis Title: Quantum Effects in Molecular Nanomagnets. Tutor: Prof. Marco Affronte

October 2007: 'Laurea Specialistica' degree in Physics at "Università degli Studi di Perugia", Perugia, Italy. Thesis Title: 'Studio dei modi collettivi nell'acqua di idratazione della Ribonucleasi tramite spettroscopia Brillouin di neutroni'. Mark: 110/110.
The measurements were carried out at the high flux reactor of Institute Laue-Langevin (ILL), Grenoble, France.

October 2005: 'Laurea Triennale' degree in Physics at "Università degli Studi di Perugia", Perugia, Italia. Thesis title: "Descrizione termodinamica del processo di 'folding' delle proteine". Mark: 110/110 cum laude.

Languages:

Italian, English

Recent activities:

- Optical lithography training at NEST laboratory of Scuola Normale Superiore di Pisa, Pisa, 9-13 March 2009.
- Fabrication of Hall Probes Magnetometer devices by optical lithography at NEST laboratory of Scuola Normale Superiore di Pisa, Pisa, 29-30 July 2009.

Teaching activity:

Assistant of Prof. C. Calandra Buonaura, course of Mechanics for physics students at Università di Modena e Reggio Emilia (2008-2009).

Conferences:

- Joint European Magnetic Symposia 2010, Kraców, August 23-28, 2010. (Invited speaker).
- National School on the Physics of Matter: 'Physics of spin in materials', Hotel Monterosa, Chiavari, 2-9 November 2009. (Poster)
- MAGNET '09, I Conferenza Nazionale di Magnetismo, CNR centre, Roma 27-29 October 2009. (Poster)
- International Conference on Molecule-based Magnets. Florence, September 21-24, 2008.
- Joint European Magnetic Symposia 08, Dublin, September 14-19, 2008. (Poster)
- Summer School 'Nanomagnetism and Spintronics'. Prague, September 5-13, 2008.
- Joint Meeting on Quantum Effects in Molecular Magnets. Modena, April 29, 2008.

Publications:

- G. Lorusso, F. Troiani, V. Bellini, A. Ghirri, A. Candini, S. Carretta, P. Santini, G. Amoretti, W. Wernsdorfer, G. Timco, R.E.P. Winpenny, M. Affronte, *Spin entanglement in supramolecular systems*, Journal of Physics: Conference Series (in press)

- G. A. Timco, V. Bellini, G. Lorusso, A. Candini, T. Faust, F. Tuna, Floriana, W. Wernsdorfer, M. Affronte and R. E. P. Winpenny *Propagation of spin information at supra-molecular scale through hetero-aromatic linkers*, submitted.

- G. Lorusso, V. Corradini, A. Candini, A. Ghirri, R. Biagi, U. del Pennino, S. Carretta, E. Garlatti, P. Santini, G. Amoretti, G. Timco, R. E. P. Winpenny, and M. Affronte. *Probing local magnetization in molecular heterometallic Cr_2Cu trimer*, Phys. Rev. B **82**, 144420 (2010).

- F. Troiani, V. Bellini, A. Candini, G. Lorusso and M. Affronte, *Spin Entanglement in supramolecular Structures*, Nanotechnology **21**, 274009 (2010).

- A. Candini, G. Lorusso, F. Troiani, A. Ghirri, S. Carretta, P. Santini, G. Amoretti, F. Tuna, G. Timco, E. J. L. McInnes, R. E. P. Winpenny, W. Wernsdorfer, M. Affronte, *Entanglement in supramolecular spin systems of two weakly coupled antiferromagnetic rings (purple-Cr_7Ni)*, Phys. Rev. Lett. **104**, 037203 (2010).

- A. Ghirri, G. Lorusso, F. Moro, F. Troiani, V. Corradini, C. Muryn, F. Tuna, G. Timco, R. E. P. Winpenny, and M. Affronte, *Probing edge magnetization in antiferromagnetic spin segments*, Phys. Rev. B **79**, 224430 (2009).

Acknowledgements

I owe my deepest gratitude to my supervisor Marco Affronte. I have great respect for his wide knowledge and his logical and positive way of thinking. His patience, encouraging and personal guidance made the present thesis possible.

I would like to say a big thank to the other members of the laboratory, present and past, for their help, the constructive speeches and suggestions, but also for the pleasant time spent together: Alberto Ghirri, Andrea Candini, Christian Alvino, Christian Cervetti, Tuyen Nguyen Duc and Marco Evangelisti.

Besides, I am grateful to all the people I had the opportunity and the honor to collaborate with during these last three years and whose contribution has been essential for the realization of this thesis: from University of Modena and S3: Valdis Corradini, Filippo Troiani and Valerio Bellini; from University of Parma: Stefano Carretta, Elena Garlatti, Alberto Bianchi, Paolo Santini, Giuseppe Amoretti; from University of Manchester: Grigore Timco, Richard Winpenny and co-workers; from TASC in Trieste Giorgio Biasiol, from NEST in Pisa Daniele Ercolani, PasqualeAntonio Pingue and Lucia Sorba, and finally, from Grenoble Wolfgang Wernsdorfer.

Last but not least, a special thanks to all the Department and S3 staff: Ph.D students, researchers, technicians and administration.

Giulia Lorusso, January 2011